TECHNISCHE
UNIVERSITÄT
DARMSTADT

Structure and function analysis of two channel forming membrane proteins of medical importance – The lysosomal Transmembrane Protein 175 and the Envelope Protein of SARS-CoV-2

Vom Fachbereich Biologie der Technischen Universität Darmstadt

zur Erlangung des akademischen Grades
Doctor rerum naturalium
(Dr. rer. nat.)

Dissertation von
M.Sc. Tobias Schulze
aus Mannheim

1. Referent: Prof. Dr. Gerhard Thiel
2. Referent: Prof. Dr. Bodo Laube

Darmstadt 2021

Schulze Tobias:

Structure and function analysis of two channel forming membrane proteins of medical importance –
The lysosomal Transmembrane Protein 175 and the Envelope Protein of SARS-CoV-2

Darmstadt, Technische Universität Darmstadt

Jahr der Veröffentlichung der Dissertation auf TUPrints: 2022

URN: urn:nbn:de:tuda-tuprints-197927

Tag der mündlichen Prüfung: 16.12.2021

Wenn etwas kleiner ist als das Große,
so ist es darum noch lange nicht unbedeutend.

-Lucius Annaeus Seneca-

Table of contents

Summary

In this work, two channel proteins of medical importance were electrophysiologically characterized with respect to their structure/function correlates.

In the first part of this work, the lysosomal transmembrane protein 175 (TMEM175) was in the focus of the studies. The TMEM175 protein is associated with the development of Parkinson's disease (PD) through a yet unknown mechanism, underscoring the importance of this channel to the regulation of cellular homeostasis. The family of TMEM175 proteins in general constitutes a recently discovered type of potassium (K^+) channels that are important for autophagosome turnover and lysosomal pH regulation. From a structural point of view, TMEM175 channels lack the typical P-loop type selectivity filter, a hallmark of all canonical K^+ channels. This raises the question on how the distinct K^+ selectivity is achieved in TMEM175 channels. In this study, new insights into the mechanism of selectivity were gained by a high-resolution X-ray structure of the bacterial MtTMEM175 channel (from *Marivirga tractuosa*) in combination with electrophysiological recordings of its activity. The crystal structure of MtTMEM175 shows bulky hydrophobic residues (L35) facing the pore while hydrophilic residues like the highly conserved Thr38 are pointing out of the pore. Sequence analysis revealed the same structural features for the human homolog (hTMEM175) leading to mutational studies in both proteins. Subsequent structural and electrophysiological investigations suggested that Thr38 of MtTMEM175 as well as the corresponding layer of threonines in the hTMEM175 play a pivotal role in K^+ selectivity. The data support the view that this mechanism is a general explanation for K^+ selectivity in TMEM175 channels. An additional layer of hydrophobic amino acids in the hTMEM175 comprising two serines further increases K^+ in the human channel and further renders this protein more sensitive to blockers like 4-aminopyridine and Zn^{2+}. The combination of structural data, mutations and electrophysiological measurements further indicate that large hydrophobic side chains occlude the pore, forming a physical gate in TMEM175 channels. Channel opening of MtTMEM175 by an iris-like motion simultaneously relocates this gate and exposes the otherwise concealed selectivity filter to the pore lumen. Close scrutiny of closed- and open-state hTMEM175 cryo-EM structures furthermore provides a coherent hypothesis on a gating mechanism based on charged residues at the extracellular pore entrance.

In the second part of this work, the envelope protein of SARS-CoV-2 and its potential effects on the homeostasis of an infected host cell were studied. SARS-CoV-2 produces in host cells large amounts of envelope proteins (Ep-CoV-2). To mimic its pathophysiological impact, Ep-CoV-2 was expressed in mammalian cells and the effects on signaling parameters were monitored. Fluorescent tagged Ep-CoV-2 was detected in the endoplasmic reticulum and trace amounts in the plasma membrane (PM). Wild-type (wt) Ep-CoV-2 and, to a lesser extent, its known functional mutants (N15A, V25F) and the isolated transmembrane domains corrupted major signaling cascades in cells. This includes an elevated level of intracellular calcium (Ca^{2+}) as well as an alkalization od the cytosol and a membrane depolarization. These Ep-CoV-2-triggered effects, which potentially contribute to the pathogenesis of the viral protein, seem to result from an ion-channel activity. Two independent assays, functional reconstitution of Ep-CoV-2 in artificial membranes and rescue of K^+-deficient yeast mutants, confirm that Ep-CoV-2 generates a cation-conducting channel with a low unitary conductance and a complex ion selectivity. All results together suggest that inhibitors of this channel function can provide cell protection and virostatic effects.

Zusammenfassung

In dieser Arbeit wurden zwei Kanalproteine von medizinischer Relevanz im Hinblick auf ihre Struktur/Funktionskorrelate elektrophysiologisch charakterisiert.

Im ersten Teil dieser Arbeit steht der lysosomale TMEM175-Kanal im Mittelpunkt der Untersuchungen. Das TMEM175-Protein wird grundsätzlich mit der Entstehung der Parkinson-Krankheit, deren Mechanismus noch unbekannt ist, in Verbindung gebracht. Dies unterstreicht die Bedeutung dieses Kanals für die Regulierung der zellulären Homöostase. Die Familie der TMEM175-Proteine stellt im Allgemeinen einen kürzlich entdeckten Typ von Kalium-Kanälen dar, die für den Autophagosomen-Umsatz und die lysosomale pH-Regulierung wichtig sind. Strukturell gesehen fehlt den TMEM175-Kanälen der typische P-*Loop* Selektivitätsfilter, ein Markenzeichen aller kanonischen K^+-Kanäle. Dies wirft die Frage auf, wie eine ausgeprägte K^+-Selektivität in TMEM175-Kanälen erreicht wird. In dieser Arbeit wurden durch die Verwendung einer hochauflösenden Röntgenstruktur des bakteriellen MtTMEM175-Kanals (aus *Marivirga tractuosa*) in Kombination mit elektrophysiologischen Messungen dessen Aktivität neue Einblicke in den Mechanismus der Selektivität gewonnen. Die Kristallstruktur von MtTMEM175 zeigt, dass sperrige hydrophobe Reste (L35) der Pore zugewandt sind, während hydrophile Reste, wie das hochkonservierte Thr38, aus der Pore heraus zeigen. Die Sequenzanalyse ergab die gleichen strukturellen Merkmale für das menschliche Homolog (hTMEM175), woraufhin zu Mutationsstudien in beiden Proteinen durchgeführt wurden. Nachfolgende strukturelle und elektrophysiologische Untersuchungen legen nahe, dass Thr38 von MtTMEM175 sowie die entsprechende Threoninschicht in hTMEM175 eine zentrale Rolle bei der K^+-Selektivität spielen. Die Daten unterstützen die Ansicht, dass dieser Mechanismus eine allgemeine Erklärung für die K^+-Selektivität in TMEM175-Kanälen darstellt. Eine zusätzliche Schicht hydrophober Aminosäuren im hTMEM175, die zwei Serine umfasst, erhöht die K^+-Selektivität des menschlichen Kanals und macht das Protein außerdem empfindlicher gegenüber Blockern wie 4-Aminopyridin und Zn^{2+}. Die Kombination von Strukturdaten, Mutationen und elektrophysiologischen Messungen deutet zudem darauf hin, dass große hydrophobe Seitenketten die Pore verschließen und ein physikalisches *Gate* in TMEM175-Kanälen bilden. Das Öffnen von MtTMEM175 durch eine irisähnliche Bewegung könnte gleichzeitig sowohl das *Gate* öffnen als auch den ansonsten verborgenen Selektivitätsfilter zum Porenlumen drehen. Die genaue Untersuchung der Kryo-EM-Strukturen von hTMEM175 im geschlossenen und offenen Zustand liefert darüber hinaus eine kohärente Hypothese für dessen *Gating*-Mechanismus, der auf geladenen Resten am extrazellulären Poreneingang beruht.

Im zweiten Teil dieser Arbeit wurden das Hüllprotein von SARS-CoV-2 und seine möglichen Auswirkungen auf die Homöostase einer infizierten Wirtszelle untersucht. SARS-CoV-2 produziert in Wirtszellen große Mengen an Hüllproteinen (Ep-CoV-2). Um seine pathophysiologischen Auswirkungen zu imitieren, wurde Ep-CoV-2 in Säugetierzellen exprimiert und die Auswirkungen auf Signalparameter beobachtet.

Hierbei konnte Fluoreszenz-markiertes Ep-CoV-2 im endoplasmatischen Retikulum und Spurenmengen in der Plasmamembran nachgewiesen werden. Der Wildtyp (wt) von Ep-CoV-2 sowie, in geringerem Maße auch seine bekannten Funktionsmutanten (N15A, V25F) und dessen trunkierte Version störten die wichtigsten Signalkaskaden von Zellen. Dazu gehört ein erhöhter intrazellulärer Ca^{2+}-Spiegel, eine Alkalisierung des Zytosols sowie eine Depolarisierung der Membran. Diese durch Ep-CoV-2 ausgelösten Effekte, die möglicherweise zur Pathogenese des viralen Proteins beitragen, scheinen auf eine Ionenkanalaktivität zurückzuführen zu sein. Zwei unabhängige Tests, d.h. die funktionelle Rekonstitution von Ep-CoV-2 in künstlichen Membranen und die Komplementation von K^+-defizienten Hefemutanten, bestätigen, dass Ep-CoV-2 einen kationenleitenden Kanal mit einer niedrigen Einzelkanalleitfähigkeit und einer komplexen Ionenselektivität erzeugt. Alle Ergebnisse deuten darauf hin, dass Inhibitoren dieser Kanalfunktion einen Schutz der Wirtszelle sowie virostatische Effekte bieten können.

1. General introduction

1.1 Ion transport

Cells are separated from their environment by a ~5 nm thick lipid bilayer called the PM (Adam et al., 2009). This bilayer is built by a double layer of amphiphilic phospholipids, with long hydrophobic fatty acids making the inner barrier and the hydrophilic head groups pointing to the aqueous environments. With this architecture the membrane generates a distinction between 'inside' and 'outside', which prevents an unregulated exchange of molecules and ions between the intracellular cytosol and the extracellular medium. This barrier function of the membrane and the consequent compartmentation is one of the fundamental principles of life. But in addition to its function as an isolator the membrane also allows for a controlled and highly regulated exchange of molecules across a membrane the communication of the cell with the environment. This exchange of matter and information is mostly enabled by integral membrane proteins which are incorporated into the PM of cells; their distinct catalytic transport function ensures a selective permeability across membranes.

Unfortunately, structural investigation on membrane proteins is still very challenging because of their strong interaction with the phospholipid bilayer. To isolate integral membrane proteins from their membrane environment, they are generally challenged with aggressive treatments, which often lead to membrane disruption. Also, even after isolation, the membrane proteins are however not completely free of phospholipids and are therefore either insoluble or they form aggregates in aqueous solutions (Singer and Nicolson, 1972). Additionally, it can take years to find ways of forming crystals from membrane proteins that are suitable for analysis. For these reasons, the number of successfully resolved crystal structures of membrane proteins is still strikingly low compared to those of soluble proteins (Ostermeier and Michel, 1997; Shimizu et al., 2018).

In addition to X-ray crystallization, another method to resolve protein structures called cryo-EM was developed through the 1980s and 1990s. The advantage of this technology is that it does not require the difficult crystallization of membrane proteins. Back then when the method was initially developed, this technique could generally resolve structures only with resolutions in the order of ca. 10 Å. This is however not sufficient for providing any information on molecular details in a structure such as the orientation of amino acid side chains. A key advance in improving the resolution was to flash-freeze solutions of proteins using liquid ethane, keeping the molecules relatively still when they were bombarded with electrons (Adrian et al., 1984). This method allowed the molecules to retain their natural shape during imaging. At the same time, data analysis was carried out with sophisticated software programs that can morph thousands of 2D images into sharp 3D models. These two improvements combined enabled electron microscopes to determine the structures of proteins with much higher resolution of about 3 Å. The situation has changed since about 2012, when the detectors of cryo-EMs were improved such that they could capture quick-fire images of an individual molecule at dozens of frames per second. This is why, unlike X-ray crystallography, in which crystals lock proteins in a single, static pose, cryo-EM can be used to calculate the structure of a protein that has been flash-frozen in several conformations. In this way, it is possible to analyze different structural poses of the same protein and to deduce from them the mechanisms by which this protein works. Therefore, cryo-EM can quickly create high-resolution models of molecules that could not be resolved by X-ray crystallography, such as many integral membrane proteins. In this way, even small membrane proteins like the TRPV1 could be resolved at a resolution of 3.4 Å (Liao et al., 2013).

Integral membrane proteins can be generally divided into two classes: i) Membrane proteins that perform a function other than transport and ii) transport proteins that enable active or passive transport of soluble molecules across membranes. The class of transport proteins can be further subdivided according to how they facilitate transport across membranes. The most important group of transport proteins in the context of this work are ion channels. Ion channels play a pivotal role in several homeostatic and excitational processes by constituting passive and therefore fast (Lodish et al., 2000) ion transport across the PM as well as endomembranes. Selectivity in ion channels is defined either by charge (anions, cations) or by the size of the ion, which is transported through an aqueous pathway in the protein (such as K^+, Na^+, Ca^{2+}, Cl^-, F^-; Hille, 2001). Ions are able to pass through the pore only when the channel is in its open state. A stochastic switching from the open (conductive) to the closed (non-conductive) state or *vice versa* is called gating. A number of possible mechanisms for such a switching between a closed and an open state in channel proteins have already been discovered. In this context, some common structural features in gating, that are also related to the present work, are single hydrophobic amino acid residues or entire hydrophobic domains that close the channel by obstructing the channel pore. For example, the primary activation gate of Kv channels is formed by the mostly hydrophobic C-terminal parts of the S6 helices that intersect near the membrane-to-cytosol transition. This intersection of helices forms a hydrophobic barrier and therefore prevents the passage of hydrated K^+ ions into or out of the cavity. Because of its overall structure it is referred to as a bundle-crossing gate (Bavro et al., 2012; Kuang et al. 2015). Crystal structures of many K^+ channels reveal that the region where the TM-helices intersect at the bundle crossing is relatively hydrophobic, but perhaps more surprisingly, the lining of the whole inner pore in many K^+ channels is also hydrophobic. Molecular dynamics (MD) simulations of the TWIK-1 K2P K^+ channel show that hydrophobic residues (Leu146/Leu261) act as a pore gate. This causes the pore or a part of it to run free of water molecules in its closed state (Aryal et al., 2014). This phenomenon is thus called de-wetting and is also known for other channels as KcsA (Aryal et al., 2015), Kv1.2 (Jensen et al., 2010) and MthK (Shi et al., 2011; Ye et al., 2010).

Due to the dynamic structure of ion channels, gating in general is a stochastic process that can be regulated by a variety of stimuli, such as pH, ligands, voltage, light or mechanical stress (Krol & Trebacz, 2000; Hille, 2001). The direction of passive ion transport is determined by the direction of the electrochemical gradient. Once ion channels are in an open state, the ions diffuse through the channel due to their Brownian molecular motion along the gradient through the channel pore, with the goal of equilibrate the concentration. Here, the change in Gibbs free enthalpy is negative, which means that this type of transport occurs spontaneously. By passing the channel protein in this manner, the ion transport can proceed with an extremely high velocity approaching that of free diffusion of ions in water (10^7 ions/s; Hille, 2001).

It is highly desired to investigate and fully understand the structure-function relations of ion channels, since a large number of diseases concerning among others the cardiac and nervous system (so-called channelopathies) are associated with only single mutations within gene sequences that code for ion channels (Ashcroft, 2006).

In the frame of several studies on channelopathies, also channels from endomembranes have been brought into focus of research. The patch clamp technique has been extensively used to measure the activity of ion channels in the PM. But since the membranes of the organelles are not directly accessible to the patch pipettes the channels in their membrane were much less studied. In the last decade, it became more and more evident that also channels in endomembrane compartments like mitochondria, endoplasmic reticulum or even lysosomes, fulfill important functions. For example, they are essential for the regulation of the luminal pH, the membrane potential and organelle fusion. In this way they regulate the transport of other solutes across the membrane and also the dynamics and fate of these organelles (Li et al., 2019).

1.2 Potassium channels

The major intracellular cation, crucial for many fundamental cellular processes of cells, is K^+. Because of its importance the PM as well as many endomembranes exhibit a distinct K^+ permeability, which is mediated by K^+ channels.

K^+ channels are ion channels which selectively facilitate the conductance of K^+ ions (Hille 2001). They are present in all biological entities and fulfill a large variety of functions. For instance, they play major roles in the control of the heartbeat, the activity of the nervous system and in osmoregulation, just to mention a few (Hille 2001; Pongs 1999). K^+ channels are mainly found in the PM, but they are also present in the membranes of intracellular organelles such as mitochondria (Szewczyk et al. 2009), endoplasmic reticulum (Salari et al. 2015) and even lysosomes (Wang et al. 2017).

1.2.1 Structure of canonical potassium channels

Potassium channels are highly diverse in their amino acid sequence, yet they all show a common topology (Doyle et al. 1998; Jiang et al. 2002; Jiang et al. 2003; Kuo et al. 2003; Long et al. 2005). They are composed of two or four monomers, which assemble as a homo- or heterotetramer or -dimer, respectively, to form a functional channel protein. In this way, a water-filled pore is formed in the center of the monomer subunits through which the K^+ ions can pass. Each monomer in turn, is composed of two to eight transmembrane domains (TMD), where a functional channel is composed of either 4 subunits of 2 or 6 TMDs each or 2 subunits of 4 or 8 TMDs each (Figure. 1.1).

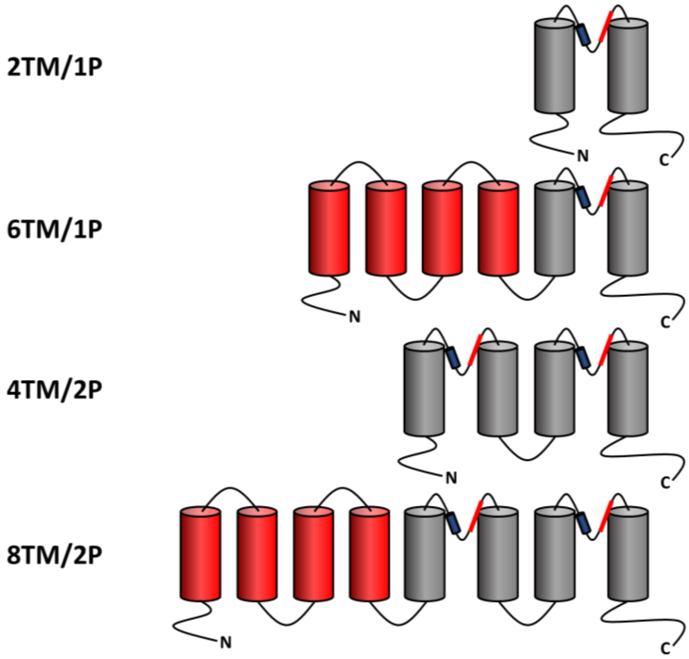

Figure 1.1: Topologies of K^+ channel subunits. The pore-forming domains (colored in grey) are composed of two transmembrane helices (TM) and a P-loop (P). Additional transmembrane helices are shown in red. N and C indicate the amino- and carboxy-terminus of the subunit.

All canonical potassium channels have a pore region composed of the same five components: Two TMDs, a pore helix, a pore loop with the filter region consisting of the same amino acid sequence motif, and a loop on the extracellular side, the turret (Figure 1.2). In the selectivity filter, all K^+ channels have the same motif in their amino acid sequence, which is therefore called the signature sequence: -TXXTXGY/FG- ('X' represents any amino acid at that position) (Heginbotham et al., 1994). The pore-lining filter region provides selective conduction of K^+ ions through the channel protein. In addition to the selectivity filter, another region in the channel protein is responsible for regulating ion permeation - the inner gate (Figure 1.2). The inner gate, also called bundle-crossing gate, enables the stochastic opening and closing of the channel. The detailed mechanisms of ion conduction, selectivity and channel gating are reviewed below.

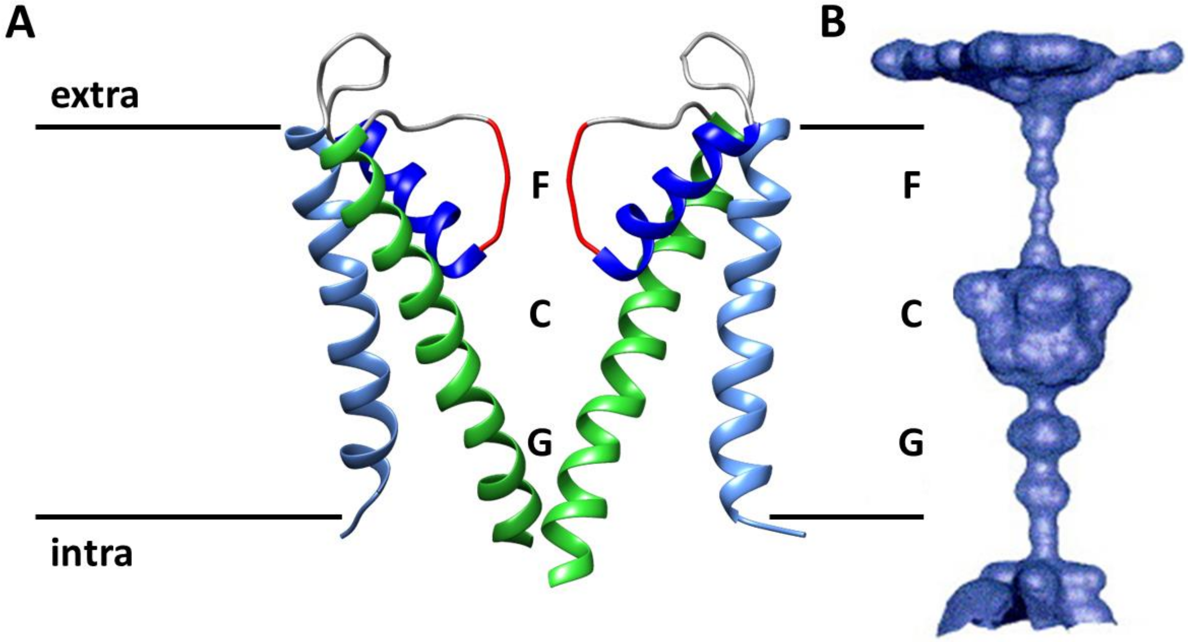

Figure 1.2: Pore domain of the prototypical potassium channel KcsA from Streptomyces lividans. (A) Shown are two opposing subunits of the KcsA tetramer in the closed state (PDB: 3EFF) viewed along the membrane plane. The pore-forming domain comprises of the outer helix (light blue), inner helix (green), loop regions (grey), pore helix (blue), and selectivity filter (red). Extra and intra indicate the extracellular and intracellular space, respectively. **(B)** Pore-lining surface of KcsA aligned with the fold diagram; filter (F), cavity (C) and gate (G) (modified from Sansom et. al., 2002).

1.2.2 Ion conductivity and selectivity

The unitary conductance of K^+ channels can reach a rate of 10^7 K^+ ions/s through the channel pore, which is approximately the rate of free diffusion of ions in water (Sansom et al., 2002). The crystal structure of a K^+ channel from *Streptomyces lividans* (KcsA) provided the first direct answer to the question on how K^+ channels manage this effective and at the same time selective conduction of K^+ ions. The ion binding sites within the selectivity filter are formed by the main chain carbonyl oxygens of the signature sequence TVGYG together with the hydroxyl oxygen atoms of the conserved threonine groups (Doyle et al. 1998). These oxygen atoms create a stack of oxygen rings that form four discrete ion binding sites (S1-S4) within the selectivity filter and an additional ion binding site (S0) at the extracellular pore entrance (Figure 1.3; Doyle et al. 1998, Alam and Jiang 2011). In the case of a K^+ efflux, a K^+ ion enters the channel from the intracellular side into the water-filled cavity and then passes the binding sites (S4-S1) in the selectivity filter to subsequently reach the extracellular exit (S0) (Figure 1.3). In the aqueous solution of the cavity the K^+ ion is surrounded by a hydrate shell. Because of the geometric constraint imposed by the filter, K^+ must be dehydrated to pass through the selectivity filter (Doyle et al., 1998). The carbonyl oxygens of the amino acids in the filter thereby form a substitute for the hydrate shell of K^+ (Figure 1.3, Figure 1.4). The energetic costs of the dehydration process are compensated by the stabilization of the potassium ion by the eight oxygen ligands arranged in a square antiprism geometry at each ion binding site (Figure 1.3; Alam and Jiang 2011). The energy required for the passage of K^+ ions through the channel pore is thereby significantly reduced (MacKinnon, 2003).

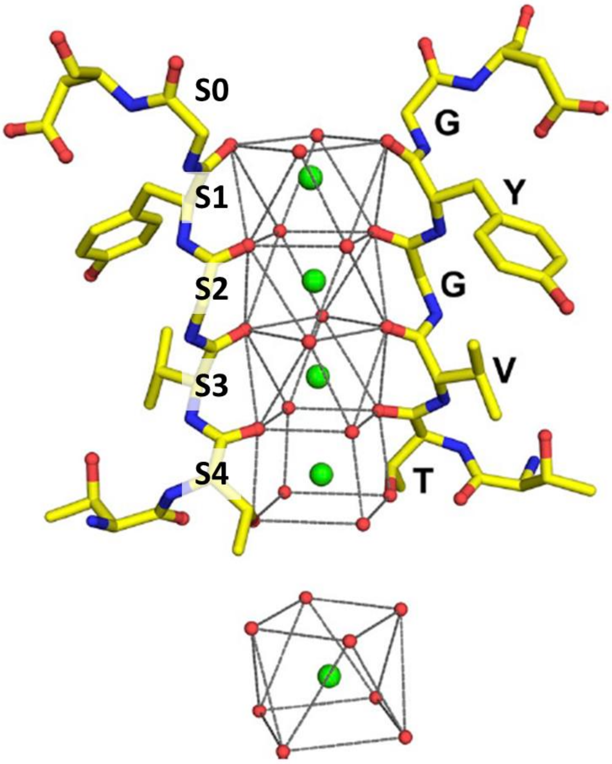

Figure 1.3: Structure of the selectivity filter of the bacterial K^+ channel KcsA. The five ion binding sites within the filter are labeled S0-S4 from top to bottom. The amino acids of the signature sequence are labeled with their single-letter abbreviations. Potassium ions are shown as green spheres, oxygen atoms as red balls. The potassium ion in the cavity (bottom) is surrounded by eight water molecules (modified from Alam and Jiang 2011).

In this way, the distance between the carbonyl oxygens of the amino acids in the filter (of neighboring as well as adjacent subunits), determines the high selectivity of K^+ channels. Sodium ions (Na^+) e.g., which are also physiologically important, are conducted at least 1,000 times less efficient than K^+, although Na^+ ions have even a smaller atomic radius (0.95 Å for Na^+ compared to 1.33 Å for K^+) (Figure 1.4; MacKinnon 2003;). This high K^+ over Na^+ selectivity of potassium channels can be explained by the rigid geometry of the ion binding sites in the filter. The latter provide a good fit for dehydrated K^+ ions but not for smaller and more solvated Na^+ ions (Doyle et al. 1998). Therefore, the entry and transfer of Na^+ ions is, due to a higher dehydration energy and a higher coulombic energy, thermodynamically unfavorable (Bezanilla and Armstrong 1972, Doyle et al. 1998).

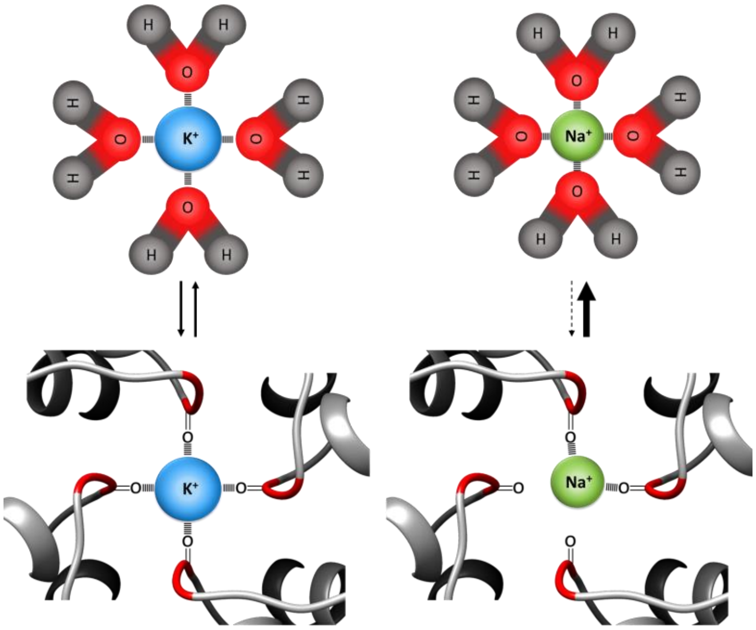

Figure 1.4: Schematic representation of the selectivity filter of a potassium channel; comparative for potassium ions (left) and sodium ions (right). Free ion with hydrate shell (top); ion in the selectivity filter of a potassium channel (KcsA; PDB: 3EFF; bottom)). The potassium ion is optimally stabilized by the carbonyl groups of one amino acid from each subunit of the channel protein. This stabilization is less optimal for the sodium ion, since the distance between two opposing oxygen atoms of the hydrate shell is significantly smaller than that for potassium ions.

In addition to prokaryotes and eucaryotes a group of small, highly hydrophobic viral proteins with channel function, termed viroporins, has been identified in diverse viral systems. These include the HCV p7 protein (Pavlovic et al., 2003), human immunodeficiency virus type 1(HIV-1) Vpu (Gonzalez and Carrasco, 1998, Schubert et al., 1996), influenza A virus M2 (Pinto et al., 1992), hepatitis A virus 2B (Jecht et al., 1998), semliki forest virus 6K (Sanz et al., 1994), picornavirus 2B (Agirre et al., 2002, Aldabe et al., 1996), and avian reovirus p10 protein (Bodelon et al., 2002). Viroporins show a different structure and oligomerization than most of the well-known ion channels. They contain at least one transmembrane domain that interacts with and expands the lipid bilayer. The transmembrane domain can form hydrophilic pores in the membrane by oligomerization (Carrasco et al., 1995, Gonzalez and Carrasco, 2003). The hydrophilic channels allow low molecular weight hydrophilic molecules to cross the membrane barrier, leading to the disruption of membrane potential, collapse of ionic gradients, and release of essential compounds from the cell.

In most cases, conduction by viroporins does not occur in a highly selective manner. However, there are also viral ion channels that are highly selective for just one type of ion – e.g. viral K$^+$ channels. Prokaryotic and eukaryotic K$^+$ channels are usually composed of several hundred amino acids per monomer. For example, a subunit of the relatively small bacterial potassium channel KirBac1.1 is composed of 333 amino acids (Kuo et al. 2003). Highly regulated channels with large N- and C- termini, such as the human ERG (hERG) channel, are with more than 1000 amino acids per monomer truly gigantic (Vandenberg et al. 2012). In contrast, dsDNA viruses of the *Phycodnaviridae* family encode for miniature potassium channels with usually less than 100 amino acids per monomer (Thiel et al. 2011). In spite of their small size these so-called, Kcv channels exhibit many of the functional but also structural properties of more complex potassium channels: they show a high K^+ over Na^+ selectivity, fluctuate stochastically between open and closed states and can be inhibited by classical potassium channel blockers such as Ba^{2+} (Gazzarini et al. 2009, 2003, Braun et al. 2014). From a structural point of view, these viral K^+ channels are very similar to the pore module of all canonical K^+ channels.

In this work, two newly discovered ion channels with an unusual structure are examined in more detail. **In the first part**, the lysosomal TMEM175 channel was in the focus of the studies. TMEM175 channels show a very different architecture as canonical K^+ channels. The most prominent difference is probably that the subunits assemble in an inverted kind of way, so that helix one (the N-terminal helix) is the pore-lining helix rather than the C-terminal helix as it is the case for canonical K^+ channels. (Cang et al., 2015). Additionally, TMEM175 channels lack the typical P-loop type selectivity filter, a hallmark of all canonical K^+ channels, which raises the question on how the distinct K^+ selectivity is achieved in this family of channel proteins. To gain insight into their structure and mechanisms of gating and ion selectivity, I used the high-resolution crystal structure of MtTMEM175 as a structural basis to perform functional analysis *via* patch clamp.

In the second part, the envelope protein of SARS-CoV-2 was functionally investigated. This homopentameric viroporin is composed of 5 subunits each comprising a short hydrophilic N-terminus, a long transmembrane domain, and a long hydrophilic C-terminal domain with an alpha helical fold (Surya et al., 2018). Computer-based models and structural studies suggest, that this protein of SARS-CoV-2 forms a central pore that could serve as an ion channel (Mandala et al., 2020; Park et al., 2021; Surya et al., 2018). For an understanding of the functional role of the E-protein in viral infection and replication, a detailed characterization of ion channel activity is essential.

1.3 References

Adam G, Läuger P, Stark G. 2009. Physikalische Chemie und Biophysik. DOI: https://doi.org/10.1007/978-3-642-00424-7

Adrian M, Dubochet J, Lepault J, McDowall AW. 1984. Cryo-electron microscopy of viruses. Nature. 308(5954):32-6. DOI: 10.1038/308032a0, PMID: 6322001

Agirre A, Barco A, Carrasco L, Nieva JL. 2002. Viroporin-mediated membrane permeabilization. Pore formation by nonstructural poliovirus 2B protein. J Biol Chem. 277(43):40434-41. DOI: 10.1074/jbc.M205393200, PMID: 12183456

Alam A, **Jiang Y**. 2011. Structural studies of ion selectivity in tetrameric cation channels. J Gen Physiol. 137(5):397-403. DOI: 10.1085/jgp.201010546, PMID: 21518828

Aldabe R, Barco A, Carrasco L. 1996. Membrane permeabilization by poliovirus proteins 2B and 2BC. J Biol Chem. 271(38):23134-7. DOI: 10.1074/jbc.271.38.23134, PMID: 8798506

Aryal P, Abd-Wahab F, Bucci G, Sansom MS, Tucker SJ. 2014. A hydrophobic barrier deep within the inner pore of the TWIK-1 K2P potassium channel. Nat Commun. 5:4377. DOI: 10.1038/ncomms5377, PMID: 25001086

Aryal P, Sansom MS, Tucker SJ. 2015. Hydrophobic gating in ion channels. J Mol Biol. 427(1):121-30. DOI: 10.1016/j.jmb.2014.07.030, PMID: 25106689

Ashcroft FM. 2006. From molecule to malady. Nature, 440,440–447. DOI: https://doi.org/10.1038/nature04707

Bavro VN, De Zorzi R, Schmidt MR, Muniz JR, Zubcevic L, Sansom MS, Vénien-Bryan C, Tucker SJ. 2012. Structure of a KirBac potassium channel with an open bundle crossing indicates a mechanism of channel gating. Nat Struct Mol Biol. 19(2):158-63. DOI: 10.1038/nsmb.2208, PMID: 22231399

Bezanilla F, **Armstrong CM**. 1972. Negative conductance caused by entry of sodium and cesium ions into the potassium channels of squid axons. J Gen Physiol. 60(5):588-608. DOI: 10.1085/jgp.60.5.588, PMID: 4644327

Bodelón G, Labrada L, Martínez-Costas J, Benavente J. 2002. Modification of late membrane permeability in avian reovirus-infected cells: viroporin activity of the S1-encoded nonstructural p10 protein. J Biol Chem. 277(20):17789-96. DOI: 10.1074/jbc.M202018200, PMID: 11893756

Braun CJ, Lachnit C, Becker P, Henkes LM, Arrigoni C, Kast SM, Moroni A, Thiel G, Schroeder I. 2014. Viral potassium channels as a robust model system for studies of membrane-protein interaction. Biochim Biophys Acta. 1838(4):1096-103. DOI: 10.1016/j.bbamem.2013.06.010, PMID: 23791706

Cang C, Aranda K, Seo YJ, Gasnier B, Ren D. 2015. TMEM175 is an organelle K(+) Channel regulating lysosomal function. Cell 162:1101–1112. DOI: https://doi.org/10.1016/j.cell.2015.08.002, PMID: 26317472

Carrasco L. 1995. Modification of membrane permeability by animal viruses. Adv Virus Res. 45:61-112. DOI: 10.1016/s0065-3527(08)60058-5, PMID: 7793329

Doyle DA, Morais Cabral J, Pfuetzner RA, Kuo A, Gulbis JM, Cohen SL, Chait BT, MacKinnon R. 1998. The structure of the potassium channel: molecular basis of K+ conduction and selectivity. Science 280:69–77. DOI: https://doi.org/10.1126/science.280.5360.69, PMID: 9525859

Gazzarrini S, Severino M, Lombardi M, Morandi M, DiFrancesco D, Van Etten JL, Thiel G, Moroni A. 2003. The viral potassium channel Kcv: structural and functional features. FEBS Lett. 552(1):12-6. DOI: 10.1016/s0014-5793(03)00777-4, PMID: 12972145

Gazzarrini S, Kang M, Abenavoli A, Romani G, Olivari C, Gaslini D, Ferrara G, van Etten JL, Kreim M, Kast SM, Thiel G, Moroni A. 2009. Chlorella virus ATCV-1 encodes a functional potassium channel of 82 amino acids. Biochem J. 420(2):295-303. DOI: 10.1042/BJ20090095, PMID: 19267691

González ME, **Carrasco L**. 1998. The human immunodeficiency virus type 1 Vpu protein enhances membrane permeability. Biochemistry. 37(39):13710-9. DOI: 10.1021/bi981527f, PMID: 9753459.

Gonzalez ME, **Carrasco L**. 2003. Viroporins. FEBS Lett. 552(1):28-34. DOI: 10.1016/s0014-5793(03)00780-4, PMID: 12972148

Heginbotham L, Lu Z, Abramson T, MacKinnon R. 1994. Mutations in the K+ channel signature sequence. Biophys J. 66(4):1061-7. DOI: 10.1016/S0006-3495(94)80887-2, PMID: 8038378

Hille B, 2001. Ion channels of excitable membranes. Sinauer Associates, Inc. 3rd edition

Jecht M, Probst C, Gauss-Müller V. 1998. Membrane permeability induced by hepatitis A virus proteins 2B and 2BC and proteolytic processing of HAV 2BC. Virology. 252(1):218-27. DOI: 10.1006/viro.1998.9451, PMID: 9875331

Jensen MØ, Borhani DW, Lindorff-Larsen K, Maragakis P, Jogini V, Eastwood MP, Dror RO, Shaw DE. 2010. Principles of conduction and hydrophobic gating in K+ channels. Proc Natl Acad Sci U S A. 107(13):5833-8. DOI: 10.1073/pnas.0911691107, PMID: 20231479

Jiang Y, Lee A, Chen J, Cadene M, Chait BT, MacKinnon R. 2002. The open pore conformation of potassium channels. Nature. 417(6888):523-6. DOI: 10.1038/417523a, PMID: 12037560

Jiang Y, Lee A, Chen J, Ruta V, Cadene M, Chait BT, MacKinnon R. 2003. X-ray structure of a voltage-dependent K+ channel. Nature. 423(6935):33-41. DOI: 10.1038/nature01580, PMID: 12721618

Krol E, Trebacz K. 2000. Ways of ion channel gating in plant cells. Annals of Botany. 86(3),449–469. DOI: https://doi.org/10.1006/anbo.2000.1226

Kuang Q, Purhonen P, Hebert H. 2015. Structure of potassium channels. Cell Mol Life Sci. 72(19):3677-93. DOI: 10.1007/s00018-015-1948-5, PMID: 26070303

Kuo A, Gulbis JM, Antcliff JF, Rahman T, Lowe ED, Zimmer J, Cuthbertson J, Ashcroft FM, Ezaki T, Doyle DA. 2003. Crystal structure of the potassium channel KirBac1.1 in the closed state. Science. 300(5627):1922-6. DOI: 10.1126/science.1085028, PMID: 12738871

Li P, Gu M, Xu H. 2019. Lysosomal ion channels as decoders of cellular signals. Trends in Biochemical Sciences 44:110–124. DOI: https://doi.org/10.1016/j.tibs.2018.10.006, PMID: 30424907

Lodish H, Berk A, Zipursky SL, Matsudaira P, Baltimore D, Darnell J. 2000. Overview of membrane transport proteins. Molecular Cell Biology. 4th edition. New York: W. H. Freeman

Long SB, Campbell EB, Mackinnon R. 2005. Crystal structure of a mammalian voltage-dependent Shaker family K+ channel. Science. 309(5736):897-903. DOI: 10.1126/science.1116269, PMID: 16002581

MacKinnon R. 2003. Potassium channels. FEBS Lett. 555(1):62-5. DOI: 10.1016/s0014-5793(03)01104-9, PMID: 14630320

Mandala VS, McKay MJ, Shcherbakov AA, Dregni AJ, Kolocouris A, Hong M. 2020. Structure and drug binding of the SARS-CoV-2 envelope protein transmembrane domain in lipid bilayers. Nat Struct Mol Biol. 27(12):1202-1208. DOI: 10.1038/s41594-020-00536-8, PMID: 33177698

Ostermeier C, **Michel H**. 1997. Crystallization of membrane proteins. Curr Opin Struct Biol. 7(5):697-701. DOI: 10.1016/s0959-440x(97)80080-2, PMID: 9345629

Park SH, Siddiqi H, Castro DV, De Angelis AA, Oom AL, Stoneham CA, Lewinski MK, Clark AE, Croker BA, Carlin AF, Guatelli J, Opella SJ. 2021. Interactions of SARS-CoV-2 envelope protein with amilorides correlate with antiviral activity. PLoS Pathog. 17(5):e1009519. DOI: 10.1371/journal.ppat.1009519, PMID: 34003853

Pavlović D, Neville DC, Argaud O, Blumberg B, Dwek RA, Fischer WB, Zitzmann N. 2003. The hepatitis C virus p7 protein forms an ion channel that is inhibited by long-alkyl-chain iminosugar derivatives. Proc Natl Acad Sci U S A. 100(10):6104-8. DOI: 10.1073/pnas.1031527100, PMID: 12719519

Pinto LH, Holsinger LJ, Lamb RA. 1992. Influenza virus M2 protein has ion channel activity. Cell. 69(3):517-28. DOI: 10.1016/0092-8674(92)90452-I, PMID: 1374685

Pongs O. 1999. Voltage-gated potassium channels: from hyperexcitability to excitement. FEBS Lett. 452(1-2):31-5. DOI: 10.1016/s0014-5793(99)00535-9, PMID: 10376673

Sansom MS, Shrivastava IH, Bright JN, Tate J, Capener CE, Biggin PC. 2002. Potassium channels: structures, models, simulations. Biochim Biophys Acta. 1565(2):294-307. DOI: 10.1016/s0005-2736(02)00576-x, PMID: 12409202

Sanz MA, Pérez L, Carrasco L. 1994. Semliki Forest virus 6K protein modifies membrane permeability after inducible expression in Escherichia coli cells. J Biol Chem. 269(16):12106-10, PMID: 8163515

Salari S, Ghasemi M, Fahanik-Babaei J, Saghiri R, Sauve R, Eliassi A. 2015. Evidence for a KATP Channel in Rough Endoplasmic Reticulum (rerKATP Channel) of Rat Hepatocytes. PLoS One. 10(5):e0125798. DOI: 10.1371/journal.pone.0125798, PMID: 25950903

Schubert U, Ferrer-Montiel AV, Oblatt-Montal M, Henklein P, Strebel K, Montal M. 1996. Identification of an ion channel activity of the Vpu transmembrane domain and its involvement in the regulation of virus release from HIV-1-infected cells. FEBS Lett. 398(1):12-8. DOI: 10.1016/s0014-5793(96)01146-5, PMID: 8946945.

Shi N, Zeng W, Ye S, Li Y, Jiang Y. 2011. Crucial points within the pore as determinants of K^+ channel conductance and gating. J Mol Biol. 411(1):27-35. DOI: 10.1016/j.jmb.2011.04.058, PMID: 21554888

Shimizu K, Cao W, Saad G, Shoji M, Terada T. 2018. Comparative analysis of membrane protein structure databases. Biochim Biophys Acta Biomembr. 1860(5):1077-1091. DOI: 10.1016/j.bbamem.2018.01.005, PMID: 29331638

Singer SJ, **Nicolson GL**. 1972. The fluid mosaic model of the structure of cell membranes. Science. 175(4023):720-31. DOI: 10.1126/science.175.4023.720, PMID: 4333397

Surya W, Li Y, Torres J. 2018. Structural model of the SARS coronavirus E channel in LMPG micelles. Biochim Biophys Acta Biomembr. 1860(6):1309-1317. DOI: 10.1016/j.bbamem.2018.02.017, PMID: 29474890

Szewczyk A, Jarmuszkiewicz W, Kunz WS. 2009. Mitochondrial potassium channels. IUBMB Life. 61(2):134-43. DOI: 10.1002/iub.155, PMID: 19165895

Thiel G, Baumeister D, Schroeder I, Kast SM, Van Etten JL, Moroni A. 2011. Minimal art: or why small viral K(+) channels are good tools for understanding basic structure and function relations. Biochim Biophys Acta. 1808(2):580-8. DOI: 10.1016/j.bbamem.2010.04.008, PMID: 20417613.

Vandenberg JI, Perry MD, Perrin MJ, Mann SA, Ke Y, Hill AP. 2012. hERG K(+) channels: structure, function, and clinical significance. Physiol Rev. 92(3):1393-478. DOI: 10.1152/physrev.00036.2011, PMID: 22988594

Wang W, Zhang X, Gao Q, Lawas M, Yu L, Cheng X, Gu M, Sahoo N, Li X, Li P, Ireland S, Meredith A, Xu H. 2017. A voltage-dependent K+ channel in the lysosome is required for refilling lysosomal Ca2+ stores. J Cell Biol. 216(6):1715-1730. DOI: 10.1083/jcb.201612123, PMID: 28468834

Ye S, Li Y, Jiang Y. 2010. Novel insights into K+ selectivity from high-resolution structures of an open K+ channel pore. Nat Struct Mol Biol. 17(8):1019-23. DOI: 10.1038/nsmb.1865, PMID: 20676101

2. Electrophysiological characterization using structural data to gain insights into ion selectivity and gating mechanisms of lysosomal TMEM175 K$^+$ channels

2.1 Abstract

The TMEM175 family constitutes a recently discovered type of K^+ channels that are important for autophagosome turnover and lysosomal pH regulation; they are associated with the early onset of Parkinson's disease (PD). The vertebrate TMEM175 proteins are composed of two homologous non-identical repeats, each comprising six transmembrane domains forming dimers; the bacterial homologs consist of only one such repeat and assemble as tetramers. TMEM175 channels lack the typical P-loop type selectivity filter, a hallmark of all canonical K^+ channels. This raises the question on how K^+ selectivity is achieved in TMEM175 channels.

In this study, new insights gained by the X-ray structure of a closed bacterial TMEM175 channel are used in combination with electrophysiological methods to address this very question. The newly obtained crystal structure of this bacterial TMEM175, derived from *Marivirga tractuosa* (MtTMEM175), revealed two densities inside the protein, which could be assigned to K^+ ions. One K^+ ion was located at an ion binding site at the extracellular pore entrance and was surrounded by a hydrate shell. The second K^+ ion was not coordinated by water molecules, indicating permeation of dehydrated K^+ ions through the pore. These findings stand in line with electrophysiological measurements, where MtTMEM175 generated "leak-like" multi-channel currents in HEK293 cells. The crystal structure further suggests that a highly conserved layer of threonine residues in the pore mediates basal K^+ selectivity. To test this hypothesis *via* patch clamp measurements, these threonines at position 38 were mutated to alanines. In recordings on HEK293 cells expressing the T38A mutant of MtTEMEM175 an exchange of K^+ in the bath solution for Na^+ caused only a minor shift in the reversal potential by -15 ± 2 mV. For comparison, the same procedure causes a shift of -37 ± 6 mV in cells expressing the wild-type (wt) channel. The results of these experiments underpin that the respective mutation indeed reduces the selectivity for K^+ over Na^+ by a factor of 2.5 compared to the wt. The corresponding layer of threonines also accounts for K^+ selectivity in human TMEM175 channels suggesting that this mechanism is a general explanation of selectivity in TMEM175 channels. An additional layer in the human homolog (hTMEM175) comprising two serines further increases selectivity and renders this channel sensitive to blockers like 4-aminopyridine and Zn^{2+}.

The combination of structural data, mutations and electrophysiological measurements suggests that large hydrophobic side chains occlude the pore, forming a physical gate. Channel opening by an iris-like motion simultaneously relocates the gate and exposes the otherwise concealed selectivity filter to the pore lumen. Close scrutiny of the hTMEM175 cryo-EM structures furthermore provides a coherent hypothesis on the mechanism of channel gating in hTMEM175 based on charged amino acid residues in the extracellular pore entrance.

2.2 Introduction

Potassium is the major intracellular cation and is crucial for many fundamental cellular processes such as maintenance of the resting membrane potential, repolarization of action potentials, counter-ion flux and osmoregulation. The function and distribution of K^+ ions in endomembrane compartments such as endosomes and lysosomes are less clear and their significance has only recently been beginning to emerge (Feng et al., 2018). Lysosomes are small, acidic organelles that play essential roles in nutrient sensing, signaling, autophagy and degradation of macromolecules (Bollabio and Bonifacino, 2020; Lawrence and Zoncu, 2019). Furthermore, they have been recognized lately as a central hub in metabolic regulation of the cell (Perera and Zoncu, 2016; Lamming and Bar-Peled, 2019). Many of these lysosomal controlled processes are closely related to ion transport across the membrane *via* numerous channels and transporters (Li et al., 2019). Defects in such lysosomal transport proteins can lead to a variety of diseases from neurodegenerative (dementia and PD), infectious, or metabolic diseases to retinal and pigmentation disorders as well as cancer (Grimm et al., 2017; van Veen et al., 2020).

It has been known for decades that lysosomal membranes are permeable for K^+ and even more for Cs^+, a hallmark of this type of endomembranes (Henning, 1975). The channel responsible for this transport has recently been identified as a member of the TMEM175 family. TMEM175 is a constitutively-active K^+-selective channel expressed in lysosomal membranes where it is responsible for establishing a membrane potential. This ubiquitous channel was found to mediate a major K^+ permeability of lysosomes and late endosomes (Cang et al., 2015). Structurally the TMEM175 protein is not related to canonical K^+ channels, displaying a unique membrane topology as well as lacking a P-Loop with the conserved TVGYG selectivity filter of canonical K^+ channels such *Shaker*, BK and KcsA (Doyle, 1998; Long et al., 2005; Tao et al., 2017). The most prominent difference is probably that the subunits assemble in an inverted kind of way, so that helix one (the N-terminal helix) is the pore-lining helix rather than the C-terminal helix as it is the case for canonical K^+ channels. (Cang et al., 2015; Figure 2.2B).

Reflecting its divergent sequence, TMEM175 also shows great differences in terms of ion permeation properties and its pharmacology compared to canonical K^+ channels. The latter are strongly selective for K^+ over Na^+ and are blocked by Ba^{2+} as well as by Cs^+ frequently. In contrast, TMEM175 conducts cations according to a lyotropic series (so-called Hofmeister series), with Ca^{2+} being least permeable, followed by Na^+, K^+, Rb^+ and Cs^+ being most permeable (Cang et al., 2015). Only one of the common K^+ channel inhibitors, 4-aminopyridine, can inhibit TMEM175 activity (with the exception of bacterial TMEM175 proteins), while others, such as tetraethylammonium or quinine, do not alter channel activity or conductance. In contrast to canonical K^+ channels, TMEM175 can be blocked by Zn^{2+} ions instead (Cang et al., 2015). Together, these features predict unique ion permeation and selectivity mechanisms for TMEM175 proteins.

TMEM175 channels are present in animals, eubacteria and archaea but are not found in plants and fungi. They exhibit a selectivity for K^+ (P_K) over Na^+ (P_{Na}) with selectivity ratios (P_K/P_{Na}) ranging from ~35-20 in vertebrates to ~2-5 in bacteria (Cang et al., 2015; Lee et al., 2017). Because of the relatively low selectivity, their ohmic conductance and the absence of activation or inactivation kinetics, they have been described as 'leak-like' channels (Cang et al., 2015). The vertebrate TMEM175 proteins are composed of two homologous non-identical repeats, each comprising six transmembrane domains; for a functional channel these monomers form homodimers. The bacterial homologues assemble in a homotetrameric architecture where one subunit consists of only one such repeat (Figure 2.1; Brunner et al., 2020; Cang et al., 2015; Lee et al., 2017).

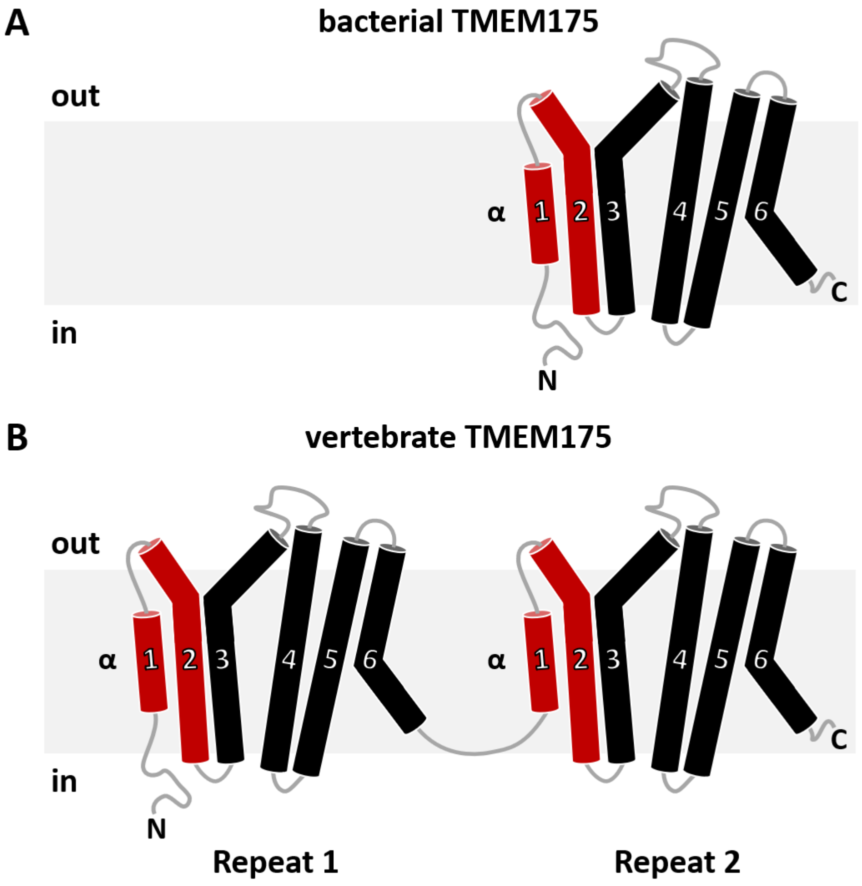

Figure 2.1: Schematic compositions of bacterial and vertebrate TMEM175 variants. (A) Scheme of the one-repeat six-transmembrane-domain (1 x 6TM) topology of bacterial TMEM175 subunits forming homotetramers. **(B)** Scheme of the two-repeat six-transmembrane-domain (2 x 6TM) topology of vertebrate TMEM175 subunits forming dimers; Pore lining domains are indicated in red. Approximate membrane boundaries are indicated in grey.

In prokaryotes, the function of TMEM175 proteins is currently unclear but may be linked to the regulation of the membrane potential (Cang et al., 2015). In vertebrates, deletion of the TMEM175 gene leads to increased lysosomal pH values under conditions of starvation, reduced proteolytic activity in lysosomes and aberrant autophagosome fusion and clearance (Cang et al., 2015; Jinn et al., 2017). The most interesting finding is that hTMEM175 has been linked to PD by several genome wide association studies. This is consistent with the fact that the coding gene is a highly significant risk gene for the early onset of this neurodegenerative disease (Jinn et al., 2017; Nalls et al., 2014; Chang et al., 2017). The deficiency in autophagosome clearance and the impaired proteolytic activity by loss of TMEM175 are presumably responsible for the accumulation of insoluble α-synuclein fibrils in PD models. This might explain why this channel is relevant for the progression of PD (Jinn et al., 2017).

Taken together, the available data show that TMEM175 is a functional K^+ selective channel, which operates in the membrane of lysosomes. Its channel function seems to be crucial for the general performance of the lysosomes. With these features the channel function of TMEM175 presents a viable drug-target for interfering with channelopathies related to malfunctions of this channel. Selectivity for K^+ ions, with the exception of the very weakly selective trimeric intracellular cation (TRIC) channels (Su et al., 2017), is intimately associated with a P-loop architecture (Doyle et al., 1998). The lack of such a P-loop motif in TMEM175 channels hence raises the question on how K^+ conduction and selectivity is achieved in this unrelated architecture.

To gain more detailed insights into the structural basis for K^+ selectivity of TMEM175 proteins, a crystal structure of a representative protein variant had to be selected. Currently, crystal structures of three different TMEM175 proteins have already been resolved namely: channel variants from *Chamaesiphon minutus* (CmTMEM175; Lee et al., 2017), *Marivirga tractuosa* (MtTEMEM175; Brunner et al., 2020) and the human homolog (hTEMEM175; Oh et al., 2020). The general architecture is very similar among these three variants. This similarity in folding as well as the high conservation of key residues in the TMEM175 variants suggests that the respective amino acids have key functions in the channel protein. For most of the highly conserved residues in MtTMEM175 at least one functional role could be assigned using structural data from a high-resolution crystal structure (2.4 Å) only. Based on these aspects it is likely that MtTMEM175 provides a clear case to characterize the TMEM175 family in general.

Consequently, this work is based on the structural data gained from the crystal structure of MtTMEM175. It aims to test functional predictions from the structural data by electrophysiological measurements of channel activity. Parts of this work has already been published in a collaborative work in Brunner J, Jakob RP, **Schulze T**, … eLife 9:e53683; 2020.

2.2.1 General architecture of MtTMEM175

Expression screening of over 30 bacterial TMEM175 variants revealed several homologues as candidates for structural characterization. One of them, MtTMEM175, was crystallized in complex with a nanobody which in turn was prepared by fusing an N-terminally truncated Maltose Binding Protein (MBP) to its C-terminus; this procedure greatly improved X-ray diffraction. The structure was solved at a resolution of 2.4 Å, from which a map of high quality could be built (Figure 2.2A, Brunner et al., 2020).

At first glance the general architecture of MtTMEM175 seems to be quite similar to the one of canonical potassium channels. Each MtTMEM175 subunit for example is composed of six transmembrane helices (Figure 2.2B) which assemble as a homotetrameric channel (Figure 2.2A). However, by taking a closer look, the MtTMEM175 structure shows a lot of structural differences compared to the well-studied potassium channels. The most striking difference is that the subunits assemble in an inverted kind of way. This means that helix one of MtTMEM175 is the pore-lining helix, as predicted earlier (Cang et al., 2015); it also constitutes the highest degree of conservation (Figure 2.2B, 2.3; Brunner et al., 2020). Furthermore, MtTMEM175 as other members of its family, lacks a P-loop selectivity filter. The latter is the hallmark of all canonical K^+ channels. This raises the question on how K^+ selectivity is achieved in TMEM175 channels.

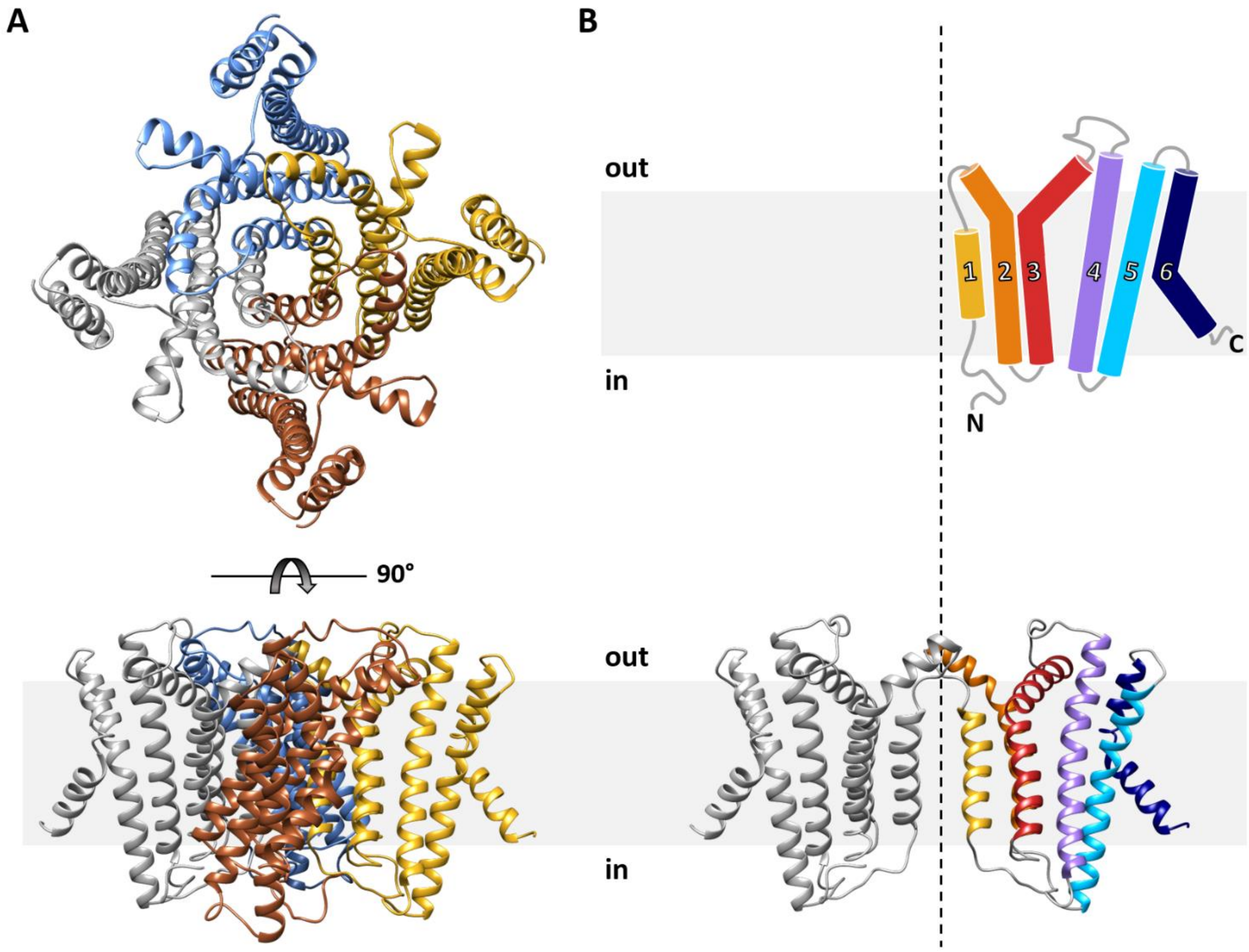

Figure 2.2: Structure of MtTMEM175. (A) Top view (top) and side view (bottom) of homotetrameric MtTMEM175 channel. **(B)** Arrangement of transmembrane helices 1–6 in MtTMEM175; schematic (top) and ribbon model derived from crystal structure (bottom; PDB: 6HD8). N- and C-termini are indicated. Two subunits are omitted for clarity; Approximate membrane boundaries are indicated in grey.

In general, the level of conservation for TMEM175 channels in transmembrane helices 4–6 is strikingly low, suggesting that this region is not involved in K^+ selectivity (Figure 2.3A). Considering the degree of conservation of the helices 1-3 among MtTMEM175 homologs three amino acids in proximity to the intracellular pore entrance (Phe28, Ser29, Asp30 in MtTMEM175) stand out in particular. This triplet is called FSD motif (Figure 2.3; Brunner et al., 2020; Cang et al., 2015). These three consecutive amino acids at the N-terminus of helix one, were originally proposed to play a central role in ion conduction (Cang et al., 2015). It has been shown for both CmTMEM175 (Lee et al., 2017) and MtTMEM175 (Brunner et al., 2020) that all three amino acids are involved in a network of hydrogen bonds that positions helices 1-3 relative to each other and interconnects adjacent subunits. With this in mind, it can be concluded that the FSD motif does not appear to play a distinct role in selectivity that would be immediately apparent from the structure (Brunner et al., 2020).

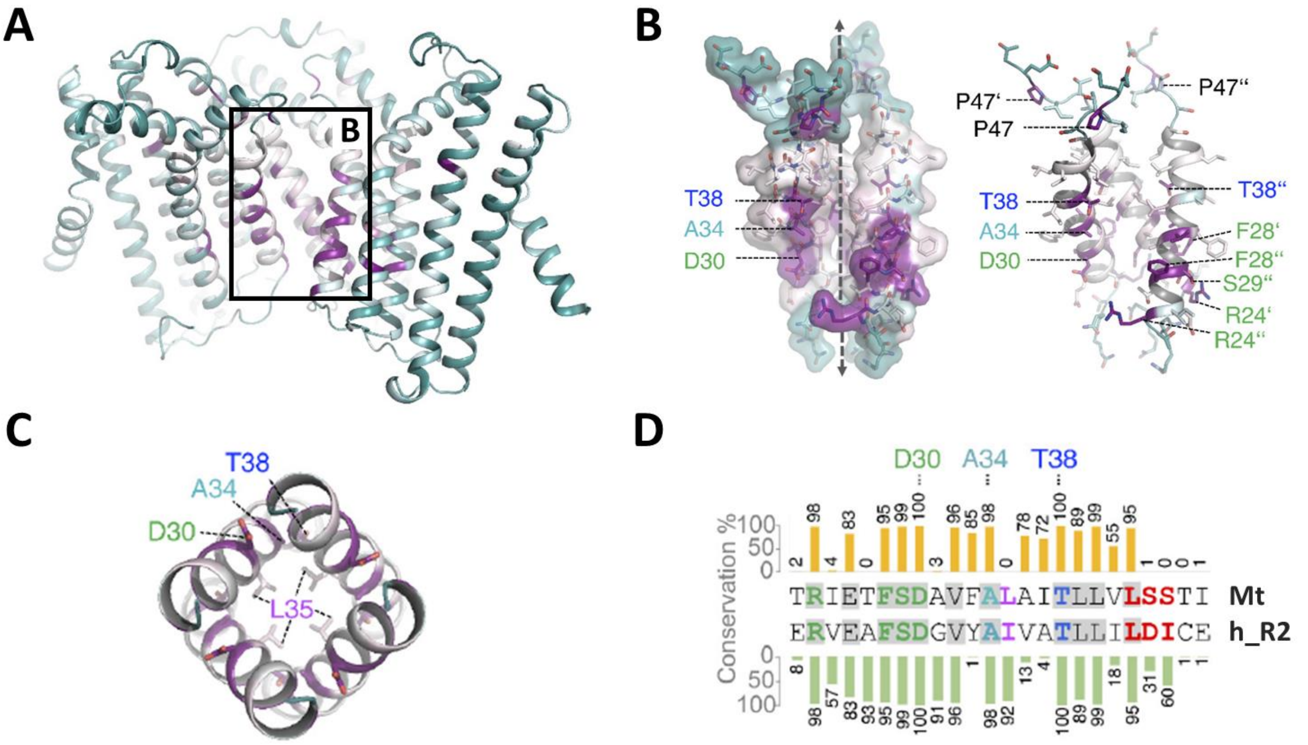

Figure 2.3: Conservation in TMEM175 proteins. (A-C) Conservation in TMEM175 projected onto the structure of MtTMEM175 (using AL2CO). Highly conserved residues are indicated and labelled. In (A) and (B), a side view is shown and one subunit has been omitted for clarity. **(C)** View from the intracellular side into the pore. Key residues are shown and pore-lining Leu35 is displayed for orientation. **(D)** Sequence alignment of helix 1. A BLAST search within the prokaryotic phyla was done using the sequence of hTMEM175 as query and the first 100 hits were aligned against each other. The conservation between helix 1 of the bacterial homologs with helix 1 of MtTMEM175 (Mt; top sequence) and of the second repeat of hTMEM175 (h_R2, bottom sequence) is given in percent in a bar chart. Conserved residues between MtTMEM175 and hTMEM175 are marked in grey (modified from Brunner et al., 2020; in turn published under CC-BY 4.0).

2.2.2 The MtTMEM175 structure reveals hydrated and dehydrated K$^+$ ions

The crystal structure of MtTMEM175, which was obtained in KCl solution, revealed two densities, which can be assigned to K$^+$ ions, termed 1K$^+$ and 2K$^+$ (Figure 2.4A). The presence of these K$^+$ ions in the protein was confirmed by data acquisition at even higher resolution of 2.025 Å (Brunner et al., 2020). In contrast, the structure of CmTMEM175, which was solved at 3.3 Å, showed no bound ions (Lee et al., 2017). One K$^+$ ion (1K$^+$, occupancy ~1) in the MtTMEM175 structure is located at an ion binding site at the extracellular pore entrance (Figure 2.4B). This binding site resembles from a structural point of view a short selectivity filter typical for canonical ion channels (Brunner et al., 2020; Chen et al., 2017; Guo et al., 2017; Shen et al., 2016). The 1K$^+$ ion is hydrated by eight water molecules in an antiprismatic geometry (Figure 2.4E, G), which in turn are coordinated by the backbone oxygens of Leu42, Ser43 and Ser44 (Figure 2.4B, D). The respective backbone oxygens of these residues of opposing subunits are 12, 13.1 and 14.9 Å apart (Figure 2.4D). By soaking crystals with Cs^+ and Rb^+, clear anomalous densities for both ions at the position of $1K^+$ were detected (Brunner et al., 2020).

The hydrated $1K^+$ ion in the MtTMEM175 crystal is reminiscent of a K^+ ion in the vestibule of a high-resolution structure of the canonical K^+ channel KcsA in close proximity to the entrance of the selectivity filter (Figure 2.4F, Zhou et al., 2001). In comparison, the two planes in the $1K^+$-hydrate in MtTMEM175 are, due to interactions with the surrounding backbone oxygens (Figure 2.4E, G), slightly twisted. Also, within the canonical selectivity filter, K^+ ions are eightfold coordinated in the square antiprism, which is mediated by backbone oxygens (Figure 2.4H; Doyle et al., 1998; Zhou et al., 2001). However, in spite of these similarities it is questionable that this region (L42-S44) determines selectivity. One argument against a filter function of this region is its low conservation between TMEM175 proteins (Figure 2.3D). Furthermore, the structure appears too simple and finally the K^+ ion is only indirectly coupled to the backbone oxygens of the protein. It could be that this binding site serves instead to attract monovalent ions with similar properties as K^+ and plays a role in the detachment or assembly of the hydrate shells of K^+ ions that pass through the pore. In addition to the ion binding site, the negative electrostatic potential in the pore lumen would be another property promoting cation permeation (Figure 2.5C).

The second K^+ ion ($2K^+$, occupancy ~0.5) is not coordinated by water molecules, indicating a permeation of dehydrated K^+ ions in these channels. In the crystal structure it is located deep in the protein between the layers of Leu35 and Thr27 (Figure 2.4A, C; Brunner et al., 2020). It is likely that this dehydrated K^+ ion is trapped in the pore. It seems as if it cannot leave this confinement due to steric restrictions at this critical position. The Leu35 of each subunit reduces the pore diameter at this position to less than 1 Å. This is a diameter that neither a dehydrated K^+ ion nor a dehydrated Na^+ ion can pass anymore. It is further worth noting that the density of $2K^+$ is likely also partly constituted by Na^+ ions, but no significant anomalous signal for Cs^+ or Rb^+ ions was found. This indicates that the channel would have to open to allow diffusion of these bigger, but generally permeable ions to this position (Brunner et al., 2020). Important to note is also that in this position the K^+ ion lacks clear interactions with the protein suggesting that it is not tightly bound to the protein but that it can in principle move. Collectively, these results showing that K^+ or Na^+ is trapped in a narrow cavity in the protein strongly suggest that in addition to this nonconductive form the protein also has a conductive conformation with a wider pore that differs from the crystal structure.

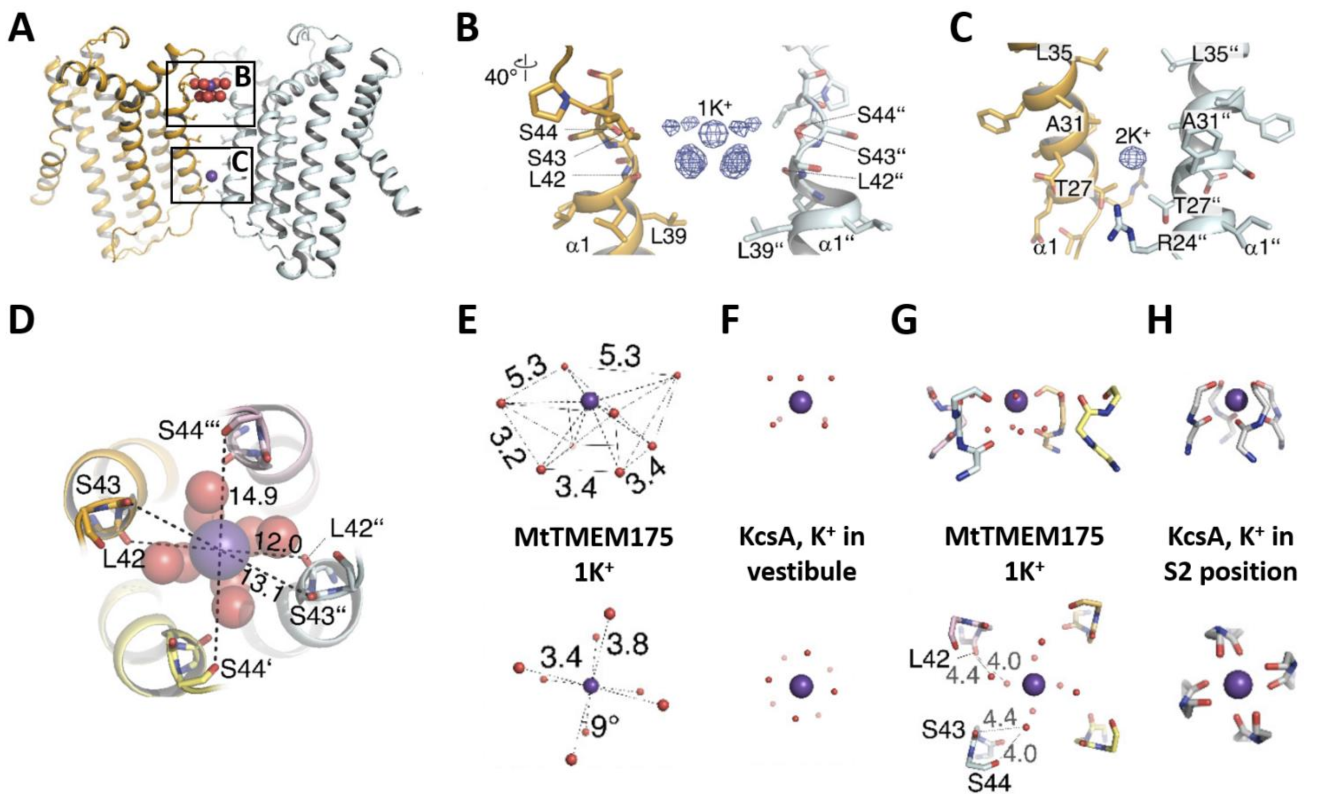

Figure 2.4: K⁺ ions in the MtTMEM175 structure. (A-C) Side view on MtTMEM175 **(A)** and close-up views of the ion binding site with a hydrated K⁺ ion at position 1K⁺ **(B)** and another K⁺ ion within the pore at position 2K⁺ **(C).** In **(A),** K⁺ ions and water molecules are displayed as purple and red spheres, respectively. In **(B)** and **(C)** the 2Fo-Fc electron density is depicted as blue mesh at the position 1K⁺ and 2K⁺ (at 2.4 Å, contoured at 1.8 s, sharpened with b = -25). Two subunits are omitted for clarity. **(D)** Top view of the ion binding site. Distances between opposing backbone oxygens of Leu42, Ser43 and Ser44 are indicated in Å. Side chains are omitted and the size of the spheres is reduced for clarity. **(E + G)** Geometry and dimensions of the hydrated K⁺ in MtTMEM175. Angles and atom-to-atom distances are indicated in degrees (°) and Å, respectively. **(F+H)** Coordination of K⁺ in KcsA by backbone oxygens (**F**, PDB: 1K4C, S2 position) and geometry of a hydrated K⁺ ion in the KcsA vestibule in proximity to the selectivity filter (**H**, PDB: 1K4C) (modified from Brunner et al., 2020; in turn published under CC-BY 4.0).

2.2.3 Bulky hydrophobic residues constrict the pore and form a physical gate in the closed state

It has already been mentioned that the finding of 2K⁺ as dehydrated ion trapped in the pore of MtTMEM175 indicates that the channel must also have an open conductive conformation. This questions both the amino acids that form the gate and the type of conformational changes which open the channel from the closed state in the crystal structure to an open conductive one.

A closer look at the pore structure reveals that the hydrophobic residues of helix 1 facing the pore lumen form a narrow bottleneck along the ion conduction pathway (Figure 2.5A, B). This does not exclude an ion passage *per se* because ion permeation through a narrow hydrophobic pathway is not unknown. One example is the pentameric bestrophin channel, in which three layers of hydrophobic residues create a 10-Å-long and 3-Å-wide ion pathway similar to the one seen in the structures of TMEM175 channels (Kane et al., 2014; Lee et al., 2017; Miller et al., 2019; Yang et al., 2014).

In the structure of MtTMEM175, especially Leu35 narrows the pore to such an extent (> 1 Å) that K^+ ions cannot pass (Figure 2.3C, 2.5A, B; Brunner et al., 2020). This bulky residue is thus likely constituting a hydrophobic physical gate on this channel. It has already been mentioned that both this highly constricted barrier and the fact that the $2K^+$ binding site is not exchanging with Cs^+ or Rb^+ in the MtTMEM175 structure indicates that the crystal structure is representing a closed state. This implies that structural rearrangements have to take place in order for the channel to become conductive. An opening of the channel would inevitably require displacement of the hydrophobic side chain of Leu35 from the pore center, probably by a helix-rotation as seen in the NaK channel (Alam and Jiang, 2009a) or in TRPV6 (McGoldrick et al., 2018). Previously, the homologous residues in CmTMEM175 (Ile23) or hTMEM175 (Ile46 and Ile271) were described as the determinants for selectivity (Lee et al., 2017) rather than a gate. However, from the crystal structure of MtTMEM175, it is more likely that this position is generally occupied by a residue that acts as a physical gate for ions.

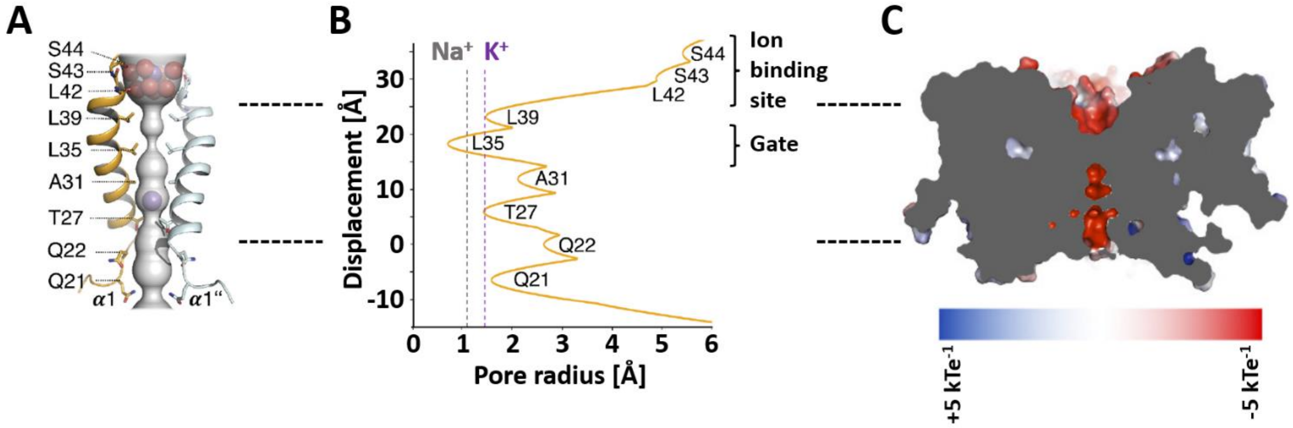

Figure 2.5: Large hydrophobic residues cause a constriction in the pore and form a physical gate in the closed state. **(A)** The ion conduction pathway is illustrated as grey surface and the pore-lining residues are displayed. K^+ ions and water molecules are shown as purple and red spheres, respectively. **(B)** The pore radius along the central axis is shown in Å. Dashed lines indicate the radii of K^+ and Na^+ ions without inner hydration shell. **(C)** Illustration of the surface electrostatic potential across the pore (modified from Brunner et al., 2020; in turn published under CC-BY 4.0).

Another argument, which favors the idea of a gate in this position versus a function in selectivity, is that the pore-lining residues physically interacting with passing ions and determining conduction or selectivity should show a high degree of conservation. After plotting the conservation of residues of randomly chosen TMEM175 proteins onto the structure of MtTMEM175 (*via* AL2CO analysis; Pei and Grishin, 2001), the most highly conserved residues are not the bulky hydrophobic residues that face the pore in the observed conformation.

The more conserved residues are located to the side of the pore-lining helix, facing helix 1 of the next subunit (Figure 2.3A, B, D). In MtTMEM175, these are the residues Thr38, Ala34 and Asp30 (the latter being part of the FSD motif) (Brunner et al., 2020). Threonine38 and Ala34 do not show any particular interaction with their respective environments, for example with the adjacent helix that they are facing. This raises the question on why these residues have such a high degree of conservation. In particular, Thr38 is of interest since it is the most conserved residue among all TMEM175 proteins (Figure 2.3D, 2.12A). Threonine38 forms a layer that is interspersed between Leu35 and Leu39 and participates in a bifurcated hydrogen bond with the main-chain oxygen of Ala34 (Brunner et al., 2020). A rotation of helix 1 (in clockwise direction when viewed from intracellular) as part of an iris-like opening of the gate (Leu35) would expose the side chain of Thr38 to the pore lumen. Following this line of thoughts, K^+ ions could interact with the side chain of Thr38 in a conductive conformation of MtTMEM175.

To gain insight into the structure and mechanisms of this new family of ion channels I used the high-resolution crystal structure of MtTMEM175 as a structural basis to perform functional analysis *via* patch clamp. The overall aim was to investigate how K^+ selectivity is achieved in TMEM175 channels. Here I show, by performing mutational studies and subsequent electrophysiological investigations, that Thr38 appears to be involved in K^+ selectivity. I also show structural and functional evidence that Leu35 functions as a hydrophobic pore gate in MtTMEM175. I further provide data that explains the increased potassium selectivity as well as the pronounced sensitivity towards 4-aminopyridine and zinc (Zn^{2+}) of human TMEM175 compared to the bacterial counterparts and suggest events that lead to channel opening.

2.3 Results and discussion

TMEM175 are a family of non-canonical potassium channels, which were identified of generating a K^+ selective conductance over the membranes of lysosomes and late endosomes. They were determined of being responsible for regulating lysosomal membrane potential and pH stability in neurons (Cang et al., 2015). Importantly, it could be shown that this channel is connected to the early onset of PD (Jinn et al., 2017; Nalls et al., 2014; Chang et al., 2017; Jinn et al., 2019; Wie et al., 2021). Although its exact function in lysosomal physiology remains to be elucidated, available experimental evidence shows that aberrant processing of autophagosomes as well as increased lysosomal pH under conditions of starvation is the prominent phenotype of TMEM175-loss (Cang et al., 2015; Jinn et al., 2017). This likely associates the lysosomal pathology with PD. Using a high-resolution MtTMEM175 structure (2.4 Å) as a basis, electrophysiological analysis was able to identify the residues that confer this channel family its K^+ selectivity.

2.3.1 MtTMEM175 is located at the plasma membrane

Since TMEM175 family proteins are usually found in lysosomes, it was first necessary to verify whether overexpression of MtTMEM175 in HEK293 cells leads to nonspecific sorting of the protein into the PM. When vYFP-tagged MtTMEM175 (MtTMEM175$_{\text{vYFP}}$) was expressed in HEK293 cells, the fluorescence associated with the protein colocalized well with the fluorescent marker ER-Tracker$^{\text{TM}}$, which specifically stains the endoplasmic reticulum (Figure 2.6A-D). This suggests that the protein enters the secretory pathway and may eventually reach the PM as well.

Although currents have been recorded in HEK293 cells transfected with TMEM175 variants from *Chryseobacterium sp*. and *Streptomyces collinus* (CbTMEM175 and ScTMEM175; Cang et al., 2015), the expression and localization of these bacterial channels at the PM has not been confirmed by other methods.

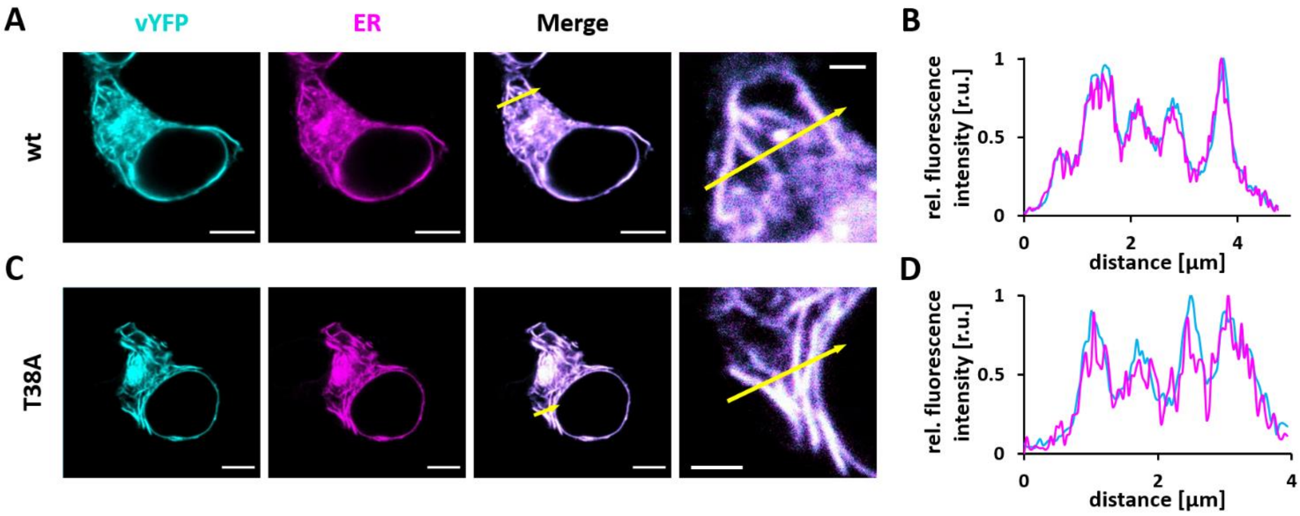

Figure 2.6: MtTMEM175 is sorted into the ER of HEK293 cells. (A+C) Representative fluorescence images of HEK293 cells transfected with vYFP tagged MtTMEM175_wt (MtTMEM175vYFP, A) or MtTMEM175vYFP_T38A (C). vYFP signal (cyan, first lane) and ER-trackerTM Blue-white DPX (magenta, second lane) colocalize (third lane, merger); Scale bar = 5 µm. Area around transect is magnified in fourth lane; Scale bar represents a distance of 1 µm (upper image) and 2 µm (lower image). **(B+D)** Plot profile along inserted arrow from corresponding merger in A or C. Colocalization of MtTMEM175vYFP_wt or MtTMEM175vYFP_T38A with ER signal.

To address the question of a PM localization for MtTMEM175, I used high-resolution microscopy of membrane proteins in the PM (Axelrod, 1981). Small PM patches of HEK293 cells expressing MtTMEM175$_{\mathrm{vYFP}}$ were isolated by de-roofing of the cell body (Biel et al., 2016) and then imaged with TIRF microscopy. The experiment was performed additionally with the mutant MtTMEM175$_{\mathrm{vYFP}}$_T38A, because Thr38 is of particular interest since it is the most conserved residue among all TMEM175 proteins. As mentioned above, Thr38 may play a special role in stabilizing the passing K^+ ions in a conductive conformation of MtTMEM175. In the case that MtTMEM175$_{\mathrm{vYFP}}$_T38A shows any different electrophysiological characteristics compared to the wt channel, it is important to know whether either the mutation affects the intrinsic properties of the channel protein or the electrical changes are only related to an impact on protein sorting. For comparison also hTMEM175$_{\mathrm{vYFP}}$ was included in the test of protein sorting since vertebrate homologs show a different channel assembly than the bacterial versions.

Figure 2.7 shows representative images of such isolated PM patches transfected with either vYFP alone (ctrl, first row) or together with hTMEM175$_{\mathrm{vYFP}}$ (second and third row), MtTMEM175$_{\mathrm{vYFP}}$ (fourth row) or MtTMEM175$_{\mathrm{vYFP}}$_T38A (T38A; fifth row). The isolated PM patch in the evanescent field can be identified from the fluorescence of the PM-specific dye CellMask™ Deep Red (CMDR, magenta). In some cases, small areas with a fluorescent signal from the ER-tracker™ (yellow) are visible, suggesting some remaining cortical ER attached to the patches.

In cells expressing only soluble vYFP (first row), no vYFP fluorescence could be detected in the evanescent field of the isolated membrane patch or the associated ER. Cells expressing $hTMEM175_{vYFP,}$ $MtTMEM175_{vYFP}$ or $MtTMEM175_{vYFP}$_T38A, however, frequently showed a vYFP signal (first lane) in the plane of the PM. This signal is composed of intense spots and a diffuse low-intensity background. In the overlay (fourth lane), the diffuse low-background vYFP signal as well as the spots with high intensity of all three tested constructs colocalize equally well with the CMDR signal.

The results of these experiments suggest that MtTMEM175 is sorted to the PM. Furthermore, the mutation at position 38 has no impact on the sorting of MtTMEM175 protein to the PM. Also, even the difference in architecture between bacterial and vertebrate variants (Figure 2.1) plays no role in protein sorting. In summary, it can be mentioned that MtTMEM175 as well as its T38A mutant and its human homolog enter the secretory pathway and terminate in the PM, where they can be functionally investigated using patch clamp analysis.

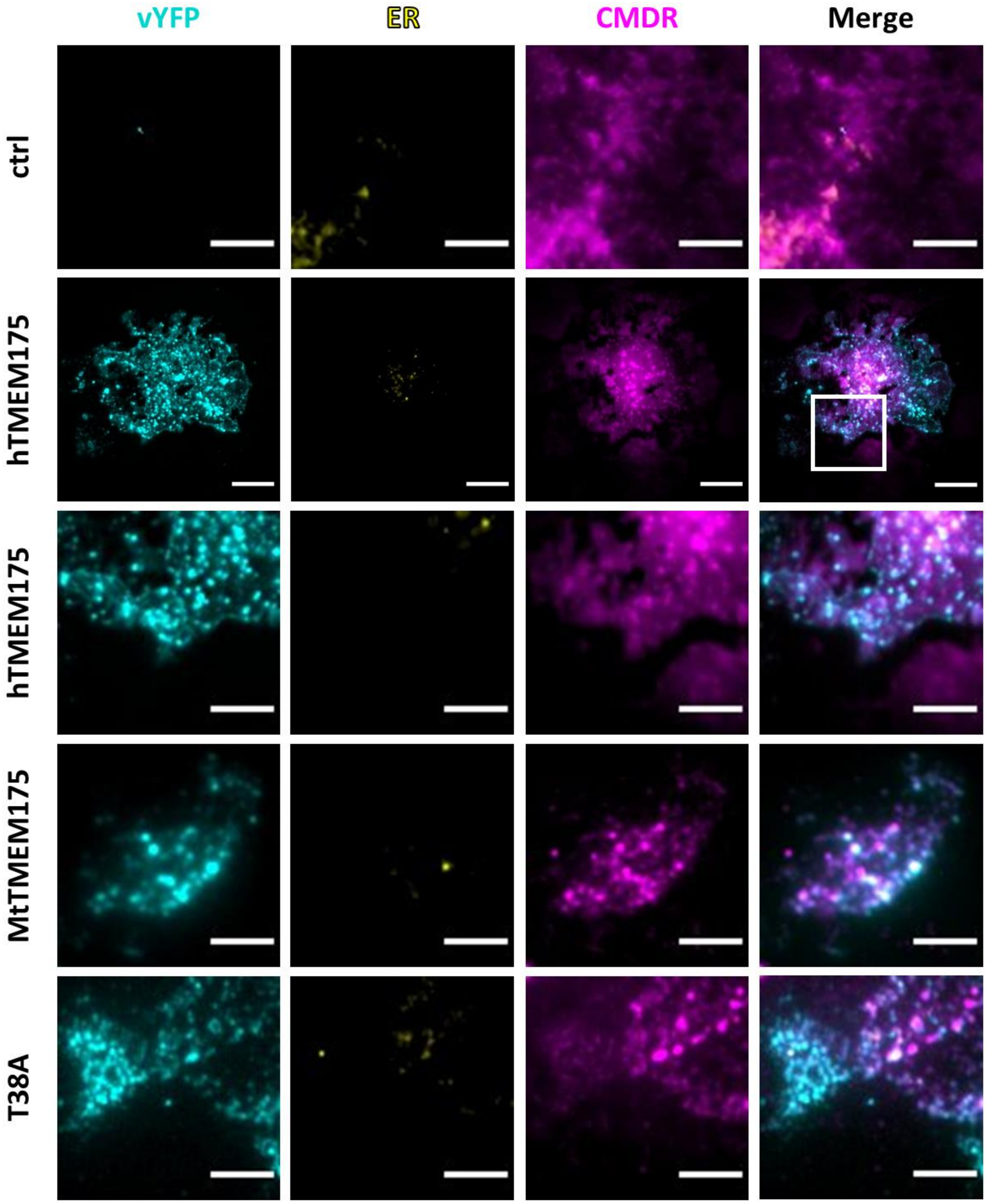

Figure 2.7: MtTMEM175 is sorted into the plasma membrane of HEK293 cells. Exemplary fluorescence TIRF microscopy images of isolated membrane patches of HEK293 cells expressing either vYFP (first row), hTMEM175$_{\mathrm{vYFP}}$ (second row, area framed in merger is magnified in third row), MtTMEM175$_{\mathrm{vYFP}}$_wt or MtTMEM175$_{\mathrm{vYFP}}$_T38A (fourth and last row). The vYFP signal shows localization of the protein of interest in isolated membrane patches (first lane, cyan). Remaining ER on the isolated patches (second lane) and isolated PM patches (third lane) are identified by ER-tracker$^{\mathrm{TM}}$ Blue-white DPX (ER, yellow) and CellMask$^{\mathrm{TM}}$ Deep Red (CMDR, magenta) fluorescence respectively. Mergers of lane 2-5 show coincidence of the proteins of interest, ER and CMDR (fourth lane). Scale bars: 10 µm in second lane or 5 µm in all others.

2.3.2 MtTMEM175 is a weakly selective K^+ channel

The crystal structure of MtTMEM175 shows two densities of K^+ ions: a hydrated one at the extracellular pore entrance ($1K^+$) and a dehydrated one trapped between the layers of T27 and L35 of each subunit ($2K^+$) (Figure 2.4A-C). The second K^+ ion ($2K^+$) is indicating the existence of a conductive conformation with a wider pore differing from the crystal structure.

In order to evaluate functionality of MtTMEM175, electrophysiological measurements *via* whole-cell patch clamp were performed. Therefore, $\text{MtTMEM175}_{\text{vYFP}}$ was expressed in HEK293 cells as previously done with CbTMEM175 and ScTMEM175 (Cang et al., 2015). As a negative control, HEK293 cells were transfected with empty pcDXC3GMS vector so that they expressed vYFP as a transfection control only. In whole-cell patch clamp experiments HEK293 cells expressing $\text{MtTMEM175}_{\text{vYFP}}$ showed non-rectifying, non-inactivating K^+ currents with no signs of voltage-dependency. The respective negative controls showed significantly lower currents originating from endogenous channels (Figure 2.8A, B). Thus, MtTMEM175 generates a functional channel which itself generates \`leak-like\` multi-channel currents under symmetrical potassium concentrations ($[K^+]_{in} = [K^+]_{ex} = 150$ mM).

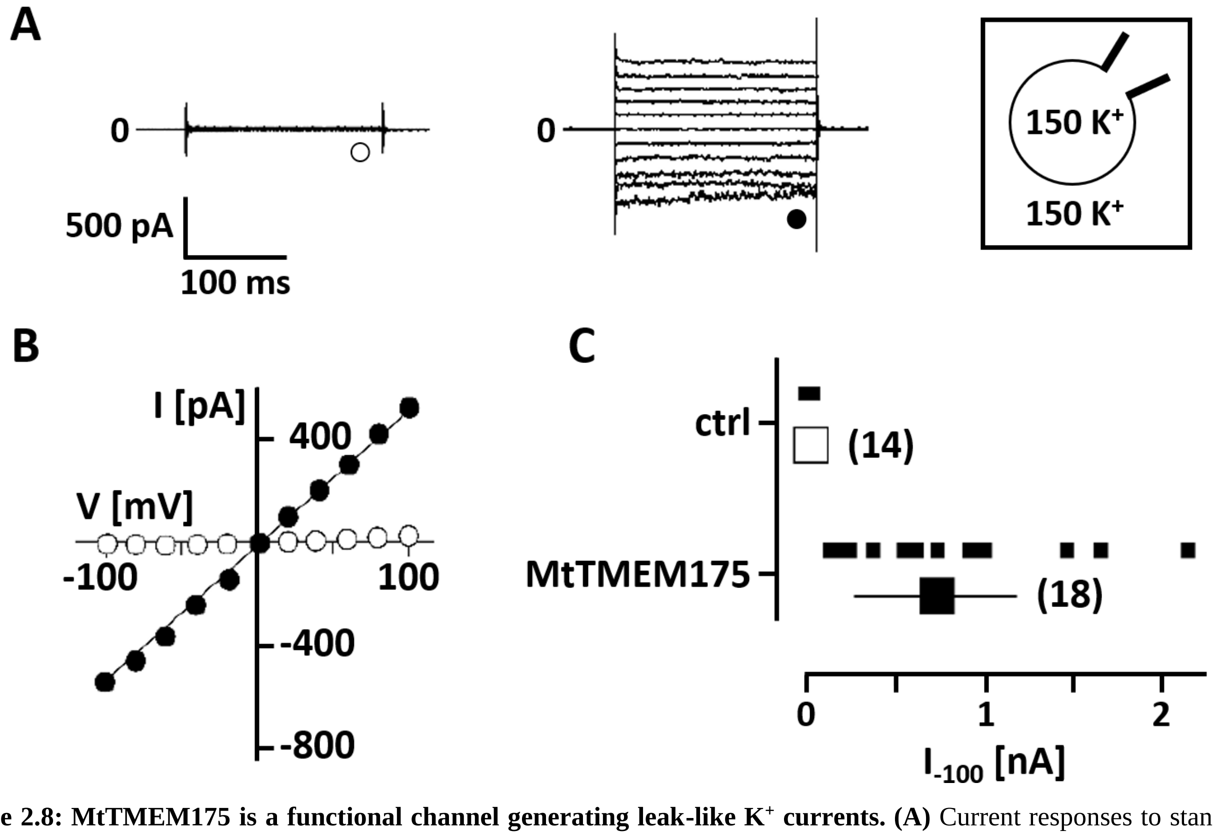

Figure 2.8: MtTMEM175 is a functional channel generating leak-like K^+ currents. (A) Current responses to standard voltage pulse protocol in mock (ctrl, ○, left) and MtTMEM175 (●, right) transfected HEK293 cells under symmetrical K^+ concentrations. **(B)** Corresponding steady state I/V relations. Plot of currents recorded in same manner at -100 mV for individual cells (small symbols) and mean ± standard deviation (s.d.) (large symbols). Number of cells in brackets.

To investigate the K^+ selectivity of MtTMEM175, the major cation in the external solution was exchanged from K^+ to Na^+ and the resulting shift of the reversal potential was measured. This shift is a diagnostic parameter for the K^+ selectivity of ion channels. Similar to CbTMEM175 and ScTMEM175, MtTMEM175 exhibits quite a low selectivity for K^+ ions over Na^+ (P_K/P_{Na} ~ 4.4) (Figure 2.9A, B). On the one hand, it conducts, unlike most of the canonical potassium channels, Cs^+ and Rb^+ with a similar efficiency as K^+ (Figure 2.9D). By soaking crystals with Cs^+ and Rb^+, clear anomalous densities for both ions at the position of $1K^+$ were detected (Figure 2.9C). This provides additional evidence for an affinity of the channel towards monovalent cations with similar properties as K^+ at this extracellular ion-binding site. On the other hand, MtTMEM175 conducts both Na^+ and Li^+ to a lesser extent than K^+ (Figure 2.9D). Even though there are some structural similarities of TMEM175 pores with the pores of bestrophin anion channels, MtTMEM175 shows no apparent permeability for anions; the reversal voltage was not significantly different when the same recordings were performed either with standard bath solution containing the large anion methanesulfonate (+0.64 ± 3 mV, n = 18) or in a bath with 150 mM KCl (2.4 ± 4 mV, n = 7).

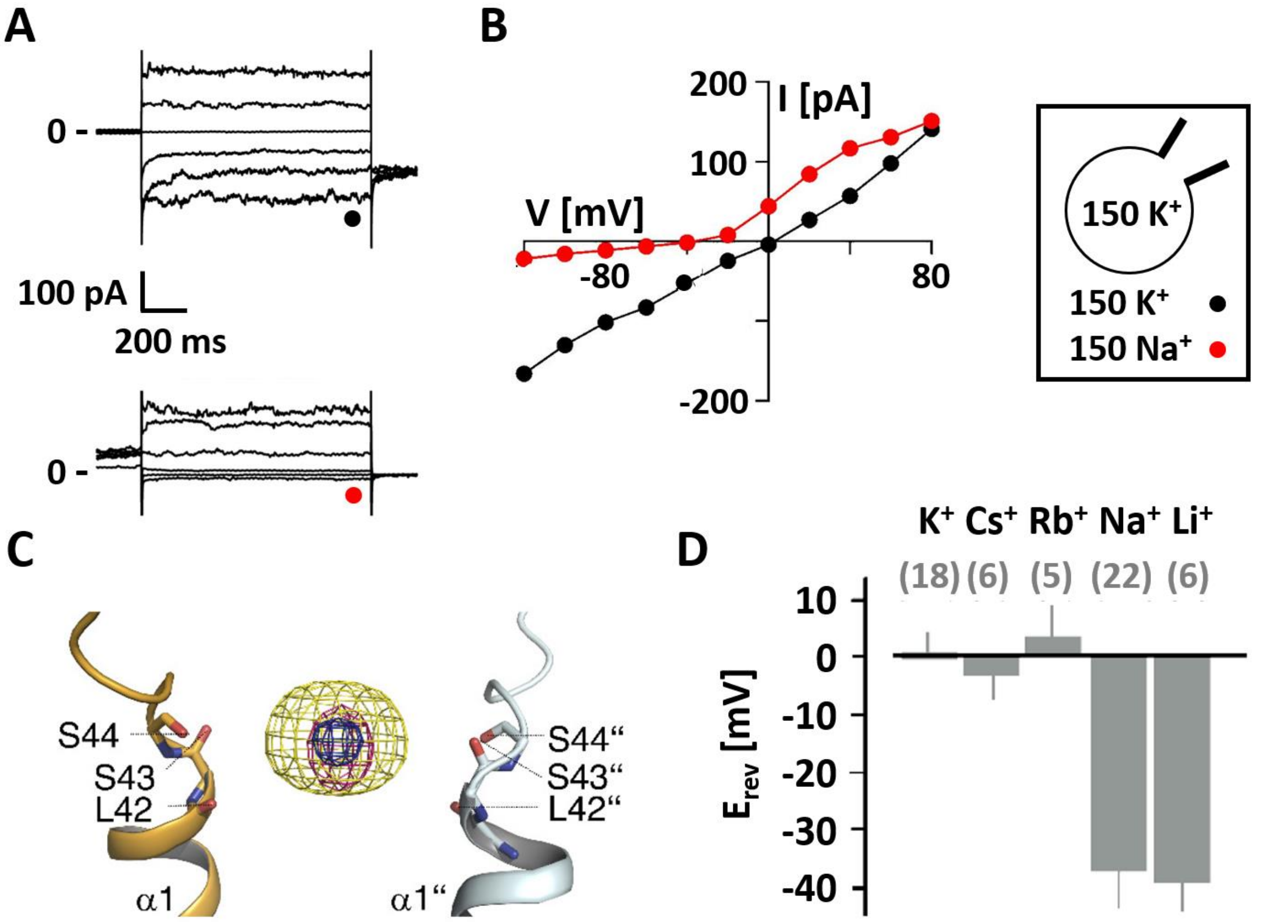

Figure 2.9: MtTMEM175 is a weakly selective K^+ channel. (A) HEK293 cells expressing MtTMEM175 before (top) and after (bottom) replacing K^+ (●) with Na^+ (●) in the external buffer **(B)** Corresponding steady state I/V relations. **(C)** Substitution of K^+ in the ion binding site with Cs^+ and Rb^+. The 2Fo-Fc electron density (blue mesh) marks the position of the K^+ ion. Anomalous difference electron densities of Cs^+ (at 3.8 Å, contoured at 7 s; PDB: 6HDA) and Rb^+ (at 3.6 Å,

contoured at 7 s, blurred with b = 125; PDB: 6HD9) are shown in yellow and magenta, respectively (modified from Brunner et al., 2020; in turn published under CC-BY 4.0) **(D)** Same experiments were performed by exchanging K^+ in external buffer by other cations. The mean reversal voltage ($E_{rev;}$ ± s.d) was used as a parameter for selectivity. Number of cells in brackets.

These \`leak-like\` whole-cell currents can be blocked by Zn^{2+} ions in the external medium in a voltage-independent manner with an applied concentration of 5 mM. The efficiency of Zn^{2+} block at this concentration is about 70% (Figure 2.10A-C).

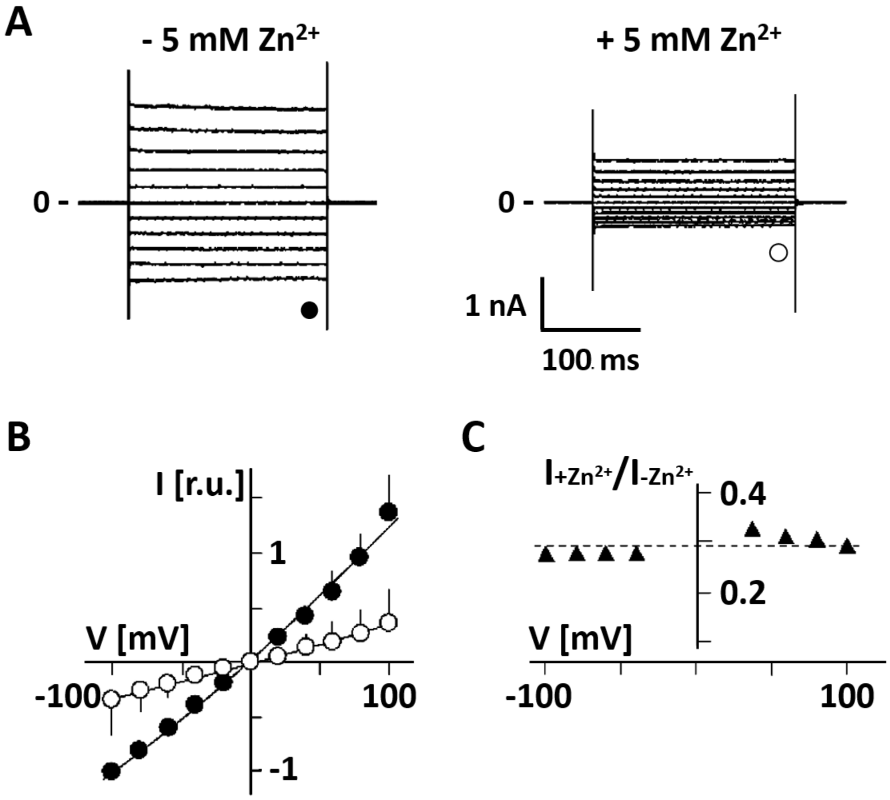

Figure 2.10: MtTMEM175 shows a voltage-independent block by Zn^{2+} ions. (A) HEK293 cells expressing MtTMEM175 before (●, left) and after (○, right) adding 5 mM ZnSO4 to the bath solution containing 150 mM K^+. **(B)** Mean I/V relations (± s.d.) of n = 4 cells. To compare the effect on different cells, the I/V relation was normalized to currents at -100 mV in the absence of blocker. **(C)** The voltage dependency of the Zn^{2+} block was estimated by dividing currents in the presence and absence of Zn^{2+} ($I_{+Zn^{2+}}/I_{-Zn^{2+}}$).

In conclusion, the expression of MtTMEM175 generates a current across the PM of HEK293 cells. These currents can be blocked by Zn^{2+} ions. This proves that MtTMEM175 is a functional channel in the PM of HEK293 cells that conducts K^+ ions, meaning that the measured currents are not the product of an indirect activation of endogenous channels. The electrical data are in good agreement with the fluorescence-microscopic measurements, which also confirm that MtTMEM175 is sorted into the PM after expression in HEK293 cells (Figure 2.7).

To further validate a channel function of MtTMEM175, and to follow up on the aforementioned expectation that the channel has a closed and an open conformation I attempted to record single-channel activity with fluctuations between an open and closed state. Expressing MtTMEM175 *in vitro* into membrane-mimicking nanodiscs and incorporating them into planar lipid bilayers (DPhPC, 10% cholesterol) revealed two different conformations of the channel. Figure 2.11A shows single channel recordings (in symmetrical 100 mM KCl, buffered with 10 mM HEPES to pH 7) after functional reconstitution of MtTMEM175 into the artificial membrane. These measurements revealed distinct channel fluctuations with up to seconds-long open and closed states and a low unitary amplitude. The presence of gating events is inconsistent with the definition of a simple \`leak-like\` channel, which is only open. The data in contrast supports the view that the channel can fluctuate between defined open and closed states. This was already expected from the position of $2K^+$ in the crystal structure. In symmetrical solutions with 100 mM KCl, MtTMEM175 generates after functional reconstitution a dominant unitary conductance of ~30 pS. The i/V relation of the channel is linear over the range of test voltages between ±180 mV (Figure 2.11B). All in all, multiple measurements resulted in several different conductivities ranging from 12 to 50 pS for the channel, but the one presented in Figure 2.11 was by far the most common one. Yet, it needs to be mentioned that measurements in which the channel remained in the membrane for an extended period of time were difficult to obtain as most of the measurements lasted less than 1 min. This could not be improved by using other lipid compositions of the bilayer (e.g., by adding PIP_2 or DPhPS with their negatively charged head groups or by using lecithin) or by replacing K^+ with Rb^+. The channel did not remain incorporated long enough to perform distinct experiments like blocking the channel with Zn^{2+}. Therefore, there is no definitive proof that the measured currents originate from MtTMEM175. However, since the planar lipid bilayer technique is a method with a very low propensity of channel contaminations from the expression system, it is highly likely that this is the case (Winterstein et al., 2018).

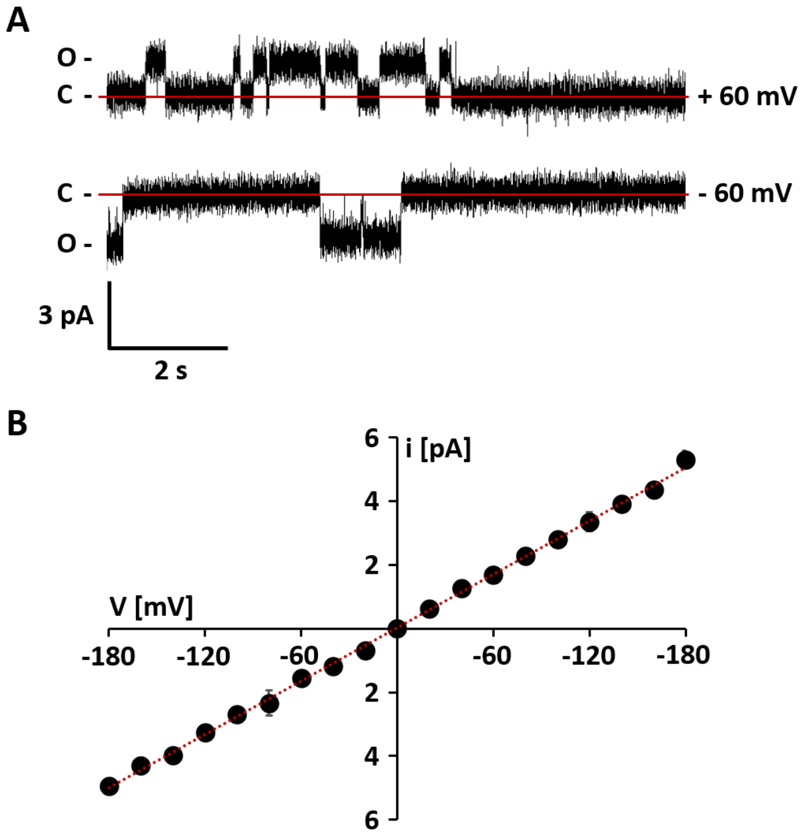

Figure 2.11: MtTMEM175 shows channel fluctuations in artificial planar lipid bilayers. (A) Exemplary current fluctuations generated by *in vitro* translated MtTMEM175 channels in lipid bilayers (DPhPC + 10% cholesterol) at ± 60 mV in symmetrical 100 mM KCl solutions buffered with 10 mM HEPES to pH 7. Red lines indicate the zero-current level. Current traces filtered at 300 Hz for visualization. **(B)** Unitary open-channel currents of MtTMEM175 from measurements performed as in A. Dashed line is the best fit of $i = \gamma \cdot V$ to the data set. Data points are arithmetic means ± s.d. of >3 independent measurements.

Besides these measurements in planar lipid bilayers also cell attached patch clamp recordings from MtTMEM175-transfected HEK293 cells revealed single channel fluctuations. In this system, MtTMEM175 generated a unitary conductance of ~70 pS (Brunner et al., 2020), which is about twice the conductance derived from the bilayer measurements reported in this study. This discrepancy could be due to the fact that the measurements were performed in different membrane environments as well as different solutions. The potassium concentration for example was 1.5 times higher in cell-attached patch clamp than in bilayer experiments. With this in mind the unitary conductance values from measurements in these two different systems are in the same order of magnitude. Collectively these results again strongly suggest that the protein has, in addition to the nonconductive form in the crystal structure, also a conductive conformation.

2.3.3 The highly conserved Thr38 confers K^+ selectivity to the MtTMEM175 channel

Thr38 that is located to the side of the pore-lining helix 1, facing helix 1 of the next subunit, is the most conserved residue among all TMEM175 proteins (Figure 2.3A, B, D; Figure 2.12A). The fact, that it is not facing the pore in the crystal structure raises the question on the function of this residue. To answer this question, Thr38 was substituted by an alanine. *Via* electrophysiological characterization of MtTMEM175_T38A the role of Thr38 in the wt protein was investigated.

When analyzed in whole-cell patch clamp recordings in HEK293 cells the T38A mutant of MtTMEM175 showed a strongly impaired selectivity for K^+ ions, as exchanging K^+ in the bath solution for Na^+ caused only a minor shift of the reversal potential by -15 ± 2 mV (n = 4). This value corresponds to a $P_K/P_{Na} < 2$ (Figure 2.12C, D). For comparison, the wt protein responds to a replacement of K^+ for Na^+ with a shift of -37 ± 6 mV (n = 22) (Figure 2.9B, D and Figure 2.12D) translating into a P_K/P_{Na} value of ~ 4.4.

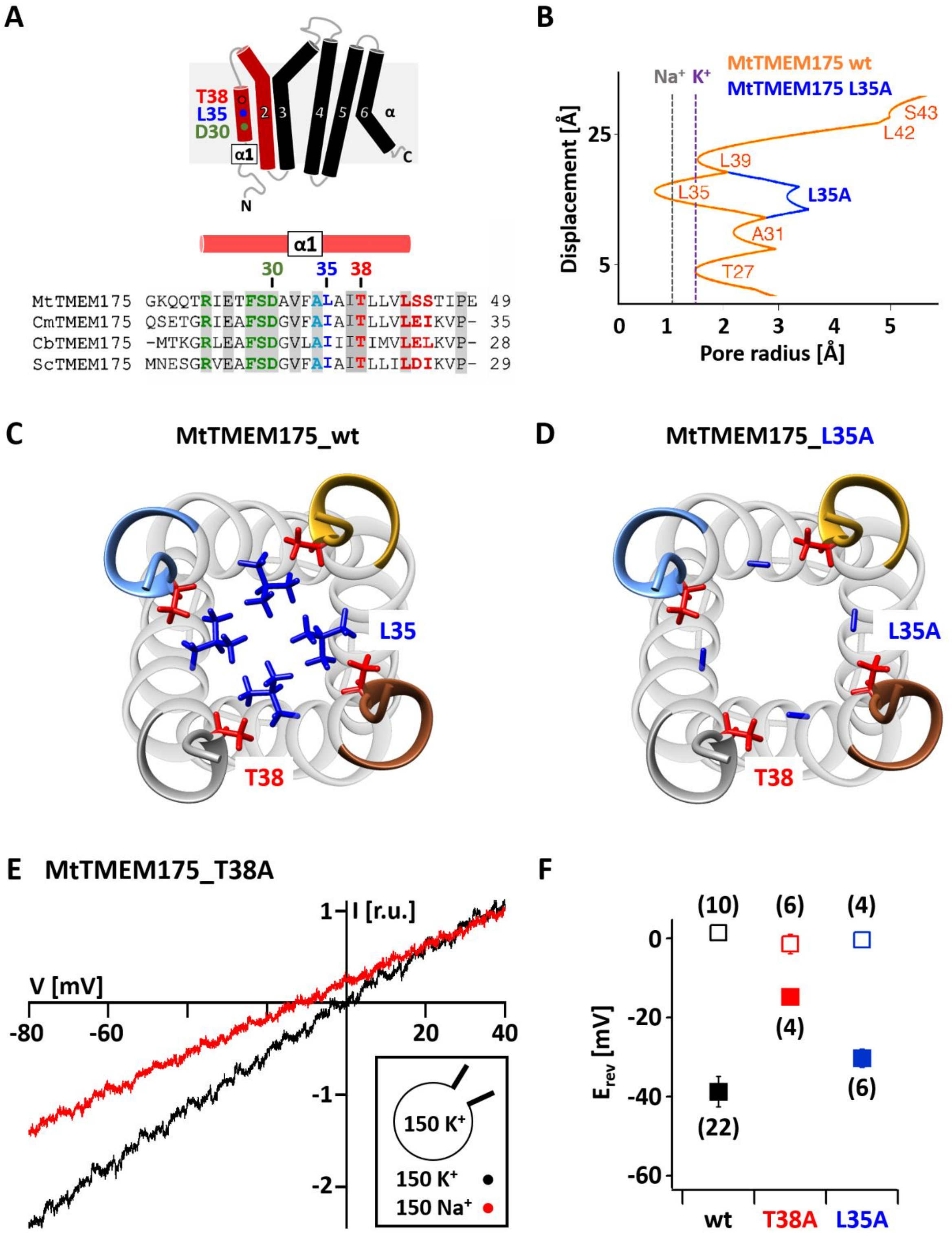

Figure 2.12: T38 confers K$^+$ selectivity to MtTMEM175. (A) Subunit organization of MtTMEM175 and alignment of bacterial sequences highlighting the most conserved residues in helix 1. **(B)** HOLE calculation of MtTMEM175 wt and the mutant L35A. The pore radius along the central axis is shown in Å. Dashed lines indicate the radii for K$^+$ and Na$^+$ without inner hydration shell. **(C+D)** Top view on pore of wt (C) and L35A mutant (D) of homotetrameric MtTMEM175 channel. Helix 2-6 are omitted for clarity. T38 and L35 (L35A) are highlighted in red and blue, respectively (PDB: 6HD8). **(E)** Representative currents elicited by a ramp protocol (-80 to +40 mV in 200 ms) from HEK293 cells transfected with the MtTMEM175 T38A in external solution with 150 mM K$^+$ (black) or Na$^+$ (red); currents were normalized to values at +33 mV. **(F)** Plot of the average reversal potentials (E_{rev} ± s.d.) for T38A or L35A mutants in comparison to wt in symmetrical buffer with 150 mM K$^+$ (□) or in external buffer with 150 mM Na$^+$ (■). Number of patched cells in brackets (A+B are modified from Brunner et al., 2020; in turn published under CC-BY 4.0).

The results of these experiments suggest that Thr38 plays a pivotal role for generating K^+ selectivity in MtTMEM175, which explains its high degree of conservation. Notably, the side chain of a conserved threonine is also essential for the coordination of K^+ ions at the end of the S4 position in the selectivity filter of canonical K^+ channels. Hence, not only carbonyl groups, but also the threonine side chain is suited to coordinate K^+ ions with impact on selectivity and conductance (Zhou and MacKinnon, 2003; Zhou and MacKinnon, 2004; Krishnan et al., 2008; Chatelain et al., 2009). However, in a crystal structure of this MtTMEM175 mutant in the closed conformation no obvious differences can be detected (Brunner et al., 2020). This suggests that Thr38 must undergo a conformational change in the open channel.

Overall, a significant contribution to K^+ selectivity by the extracellular ion binding site is contradicted by the results of the T38A mutant protein - whether the residual selectivity is arising from this motif remains open. Ascribing a function to the extracellular ion binding site therefore is currently difficult. Structural insight into the conductive conformation, which might reveal rearrangements at both ends of helix 1, will help to gain insights into potential functions of this region. The binding site could also serve an unrelated function, such as the sensing of ions to modulate the open-probability.

Since Leu35 reduces the radius of the pore to less than 1 Å and thus appears to act as a kind of bottleneck in the crystal structure of MtTMEM175 (Figure 2.5C; Figure 2.12B), it is also suspected to be involved in K^+ selectivity. When Leu35 was mutated to alanine, the channel only showed a slightly reduced selectivity compared to wt channels (E_{rev} = -31 ± 2 mV, n = 6; P_K/P_{Na} = 3.5) (Figure 2.12C, D). This data is in contrast to the findings in other TMEM175 proteins where mutations of Ile23 in CmTMEM175 and Ile46/Ile271 in hTMEM175 to alanines resulted in a loss of K^+ selectivity and channel function, respectively (Lee et al., 2017). The data collected with measurements of the L35A mutant of MtTMEM175 in this study argue against a primary function in selectivity for these bulky hydrophobic residues as discussed below.

2.3.4 A layer of threonines also accounts for K^+ selectivity in human TMEM175 channels, which is increased by Serine45

Compared to MtTMEM175, the human variant, hTMEM175, is of greater interest from an applicational point of view. Therefore, it is important to know whether the structural basis of K^+ selectivity of MtTMEM175 can also be extrapolated to its human homolog. Scrutiny of the primary sequences shows that the critical layer of threonines is indeed also conserved in vertebrate TMEM175 proteins (Figure 2.13A, B). This level of conservation raises the question of whether a mutation of the corresponding residues in the human TMEM175 channel to alanine would also affect selectivity in the human homolog.

Patch clamp recordings of hTMEM175 in HEK293 cells show that this channel is more selective than the bacterial counterparts. Previous studies reported values of P_K/P_{Na} of 35-20 (Cang et al., 2015; Lee et al., 2017). To determine the selectivity of hTMEM175 and its mutants in the PM of HEK293 cells the experimental strategy of others (Lee et al., 2017) was repeated here. From the shift in the reversal voltage after replacing K^+ for Na^+ in the external medium (-58 ± 3 mV, n = 7) a P_K/P_{Na} value of ~10 (Figure 2.13C, D) could be estimated. This is somewhat lower than the P_K/P_{Na} values previously reported for hTMEM175. Mutating Thr49 in the first repeat and Thr274 in the second repeat of hTMEM175 to alanine resulted in strongly reduced selectivity with a reversal potential of -17 ± 3 mV (n = 8) ($P_K/P_{Na} = 2$) after exchanging K^+ for Na^+ in the external solution (Figure 2.13C, D). The results of these experiments provide evidence for a conserved role of the threonine-layer in selectivity. But since the human channel is 2–3 times more selective than the known bacterial homologs, an additional factor that accounts for the higher selectivity in the human protein, probably in conjunction with the threonine layer, is highly likely.

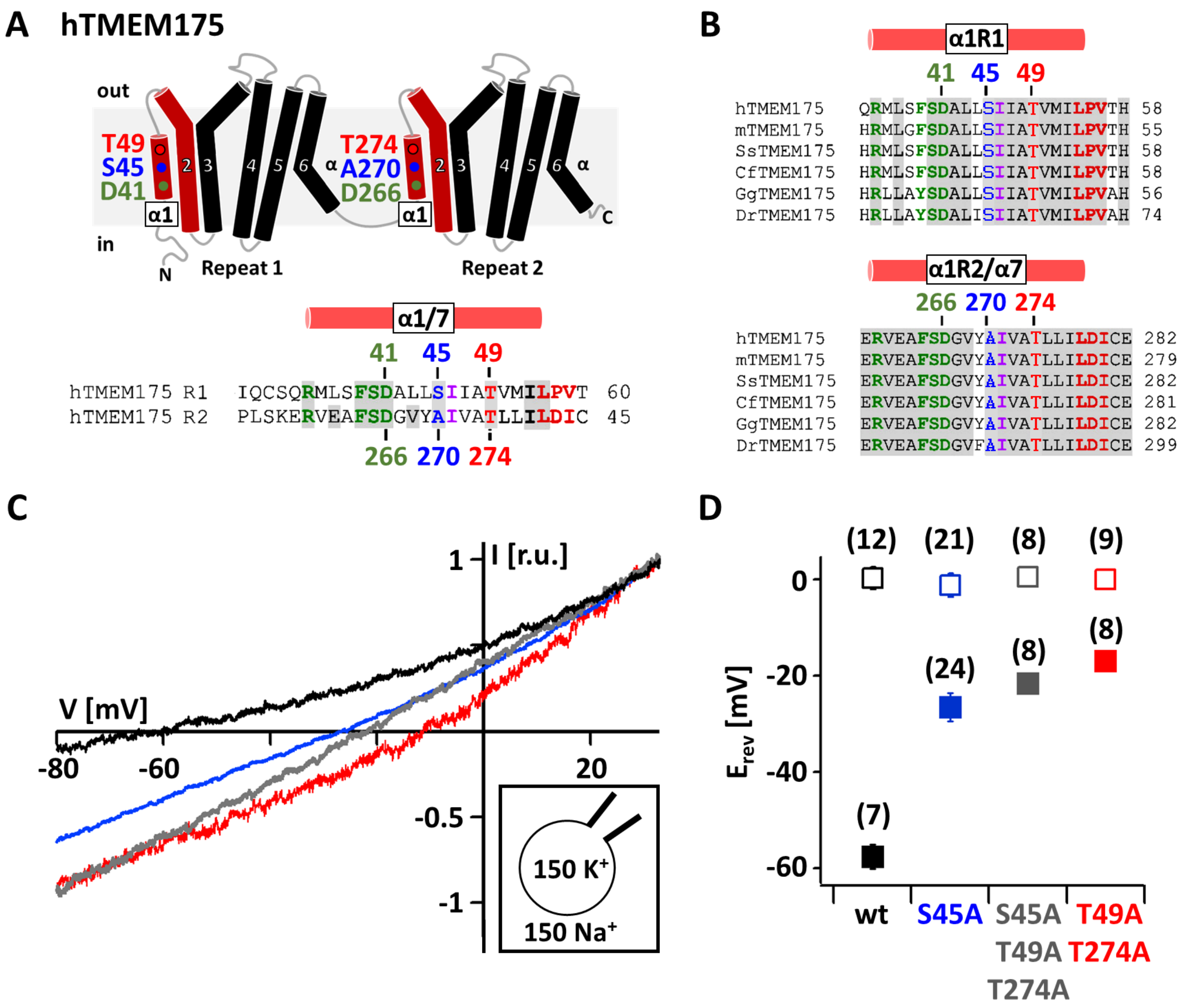

Figure 2.13: Corresponding threonines to T38 from MtTMEM175 also confer K$^+$ selectivity to hTMEM175. **(A)** Subunit organization of the channel and alignment of the crucial parts for selectivity of the two repeats of hTMEM175. **(B)** Alignment highlighting conserved residues. m: mouse, Ss: Sus scrofa, Cf: Canis familiaris, Gg: Gallus gallus, Dr: Danio rerio. **(C)** Representative currents elicited by a ramp protocol (-80 to +40 mV in 200 ms) from HEK293 cells transfected with hTMEM175 wt (black) or mutants S45A (blue), S45A/T49A/T274A (grey) or T49A/T274A (red) in external solution with 150 mM Na$^+$; currents were normalized to values at +33 mV. **(D)** Plot of the respective average reversal potentials (E_{rev} ± s.d.) for each construct in symmetrical buffer with 150 mM K$^+$ (□) or in external buffer with 150 mM Na$^+$ (■). Color coding as in (C). Number of patched cells in brackets (A+B are modified from Brunner et al., 2020; in turn published under CC-BY 4.0).

When comparing the primary amino acid sequences of the vertebrate proteins, it became apparent that the position that is corresponding to the highly conserved Ala34 in MtTMEM175 is occupied by serine in repeat 1 in all of the analyzed vertebrate species (Ser45 in hTMEM175). In contrast, in repeat 2, like in bacterial channels, the corresponding residue is an alanine (Ala270 in hTMEM175) (Figure 2.13B). Therefore, Ser45 might also play a role in the selectivity of hTMEM175 in an analogous manner as the threonines. In this scenario the side chain of these serines could contribute to coordination of K$^+$ ions in close proximity to the threonine layer to increase selectivity. In this manner six ligands would be involved in ion coordination instead of only four as in MtTMEM175. A test of this hypothesis showed that selectivity was indeed reduced in the S45A mutant dimer. The reversal potential only shifted to -27 ± 2 mV (n = 24) (P_K/P_{Na} = 3) upon changing the major cation in the bath solution from K^+ to Na^+. In the wt the respective reversal potential was -58 ± 3 mV (n = 7). This mutant is very similar to bacterial TMEM175 channels in its primary sequence of helix one and intriguingly also with respect to its preference for K^+. Consequently, a triple mutant with all of the threonine and serine residues in these two layers of the pore being exchanged for alanine (S45A/T49A/T274A) shows a similar reduction of selectivity (E_{rev} = -22 ± 3 mV, n = 8; P_K/P_{Na} = 2.4) (Figure 2.13C, D) as the double mutant T49A/T249A and the T38A mutant protein of MtTMEM175 (Figure 2.12C, D). From these experiments, it can be concluded that Ser45 in the first repeat adds to the increased selectivity of the human TMEM175 channel in conjunction with the threonine layer. In conclusion, in hTMEM175 the selectivity could be attenuated to levels of bacterial homologues by reducing the number of coordinating ligands from six to four *via* mutation of Ser45 to alanine. How exactly the presence of these two additional hydrophilic residues leads to a preference for K^+ over Na^+ ions remains to be seen. As the total number and geometry of the coordinating ligands accounts for selectivity, it is not surprising that mutation of the threonine layer suffices to lose selectivity since the remaining two serine residues alone could not effectively coordinate K^+ ions.

Generally, the data is in agreement with a scenario in which reduction of sequential ion binding sites is known to attenuate the K^+ selectivity in the canonical K^+ selectivity filter. Furthermore, introducing additional binding sites can increase selectivity (Derebe et al., 2011; Sauer et al., 2013; Kast et al., 2011; Lee and MacKinnon, 2017; Alam and Jiang, 2009b; Gouaux and Mackinnon, 2005), a principle that apparently also accounts for the different K^+ selectivity of bacterial and vertebrate TMEM175 channels.

2.3.5 Zinc ions and 4-aminopyridine act as pore blockers at the selectivity filter of hTMEM175

The next aim was to gain insight into the mechanism of channel blocking in TMEM175 proteins. In comparison to bacterial TMEM175 channels, the human TMEM175 channel is substantially more sensitive to Zn^{2+} ions. The IC50 value in the bacterial channel is ~38 mM compared to an IC50 of ~0.5 mM in human homologs (Cang et al., 2015). In addition, the human channel is also inhibited by the potassium channel blocker 4-AP (IC50 ~35 mM) (Cang et al., 2015), indicating significant differences between human and bacterial homologues and suggesting a more specific interaction of the blockers with the human channel. The finding that the block of human TMEM175 by Zn^{2+} and 4-AP is equally effective regardless on whether the blocker is added from the extracellular or intracellular side (Cang et al., 2015; Lee et al., 2017) suggests that the block is occurring in the pore. I showed that the increased selectivity for K^+ in hTMEM175 is related to Ser45, and thus speculated whether the pronounced sensitivity for Zn^{2+} and the potency of 4-AP in this channel could also be based on this difference. To address this question, I analyzed the response of the S45A mutant of hTMEM175 for these blockers in comparison with the wt protein. As shown in Figure 2.14C, D and 2.14F, G the S45A mutant is not blocked by Zn^{2+} ions and also lost its sensitivity for 4-AP at a concentration of 100 µM. These data confirm that both Zn^{2+} and 4-AP act as pore blockers at the selectivity filter, at very similar locations. The size of the 4-AP molecule further indicates that this block can only take place in a widened pore which again supports the view of a conductive conformation in addition to the non-conductive one caught in the crystal structure. In such a conductive conformation bulky side chains should not occlude the ion path and Ser45 should be facing the pore.

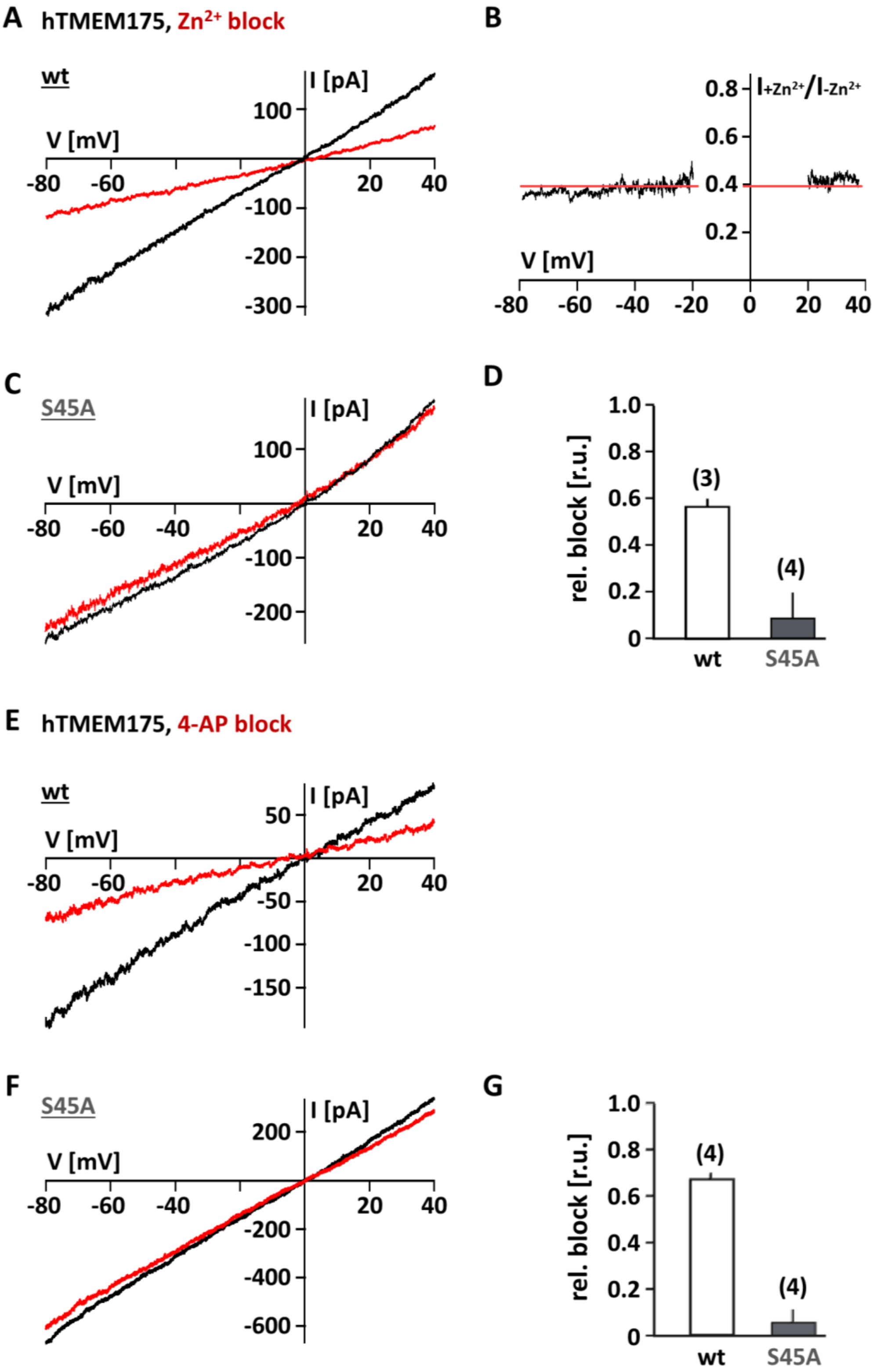

Figure 2.14: Sensitivity of the hTMEM175 S45A mutant for Zn^{2+} and 4-AP. (A+C) Currents elicited by a ramp protocol (-80 to +40 mV in 200 ms) in HEK293 cells expressing hTMEM175 wt **(A)** or hTMEM175 S45A mutant **(C)** in absence (black) and presence (red) of 5 mM ZnSO4 in external bath solution (150 mM K^+). **(B)** The ratio of currents in the presence and absence of Zn^{2+} ($I_{+Zn^{2+}}/I_{-Zn^{2+}}$) shows the voltage independency of channel block. **(D)** Columns summarize average inhibition (± s.d.) of current amplitudes at -60 mV in the hTMEM175 wt and S45A mutant. Number of measured cells in brackets. **(E+F)** same as in (A+C) with representative measurements in absence (black) or presence (red) of 100 mM 4-AP in external bath solution (150 mM K^+) for hTMEM175 wt **(E)** and S45A mutant **(F)**, respectively. **(G)** Columns show average inhibition (± s.d.) of current amplitudes at -60 mV in the hTMEM175 S45A mutant and wt. Number of patched cells in brackets.

Bacterial channels are only weakly inhibited by Zn^{2+} (Cang et al., 2015) and the S45A mutant of hTMEM175 suggests that the threonine layer constituted by Thr38 in MtTMEM175 and Thr49/Thr274 in hTMEM175 does not suffice to render TMEM175 channels sensitive to Zn^{2+}. Indeed, the T38A mutant of MtTMEM175 retained its sensitivity for Zn^{2+}; in the wt and the mutant channel Zn^{2+} caused the same relative inhibition (wt: 66.9 ± 12%, T38A mutant: 69.7 ± 10%, n = 4) at a reference voltage of -60 mV (Figure 2.15C, D). This implies that the bacterial channel is inhibited by Zn^{2+} through a different mechanism that is not a pore block. This interpretation is in contrast to the finding of an anomalous signal of Zn^{2+} ions in the crystal structure of the MtTMEM175 pore. The Zn^{2+} ion in the pore was obtained by soaking crystals of MtTMEM175 wt with 0.5 mM Zn^{2+}. The major peak of this anomalous signal lies in proximity to Thr38 and Leu35 (Figure 2.15A), a functionally critical area of the channel. In crystal soaking experiments with the T38A mutant of MtTMEM175, no anomalous signal for Zn^{2+} could be detected at all, even when using concentrations of 2.5 mM (Figure 2.15B). This supports an attraction for Zn^{2+} ions in the pore in close distance to or directly at the selectivity filter and indicates that the T38A mutation changes the electrostatic environment in the pore. However, the functional analysis does not support the idea of a Zn^{2+} block of MtTMEM175 by the same mechanism as in hTMEM175.

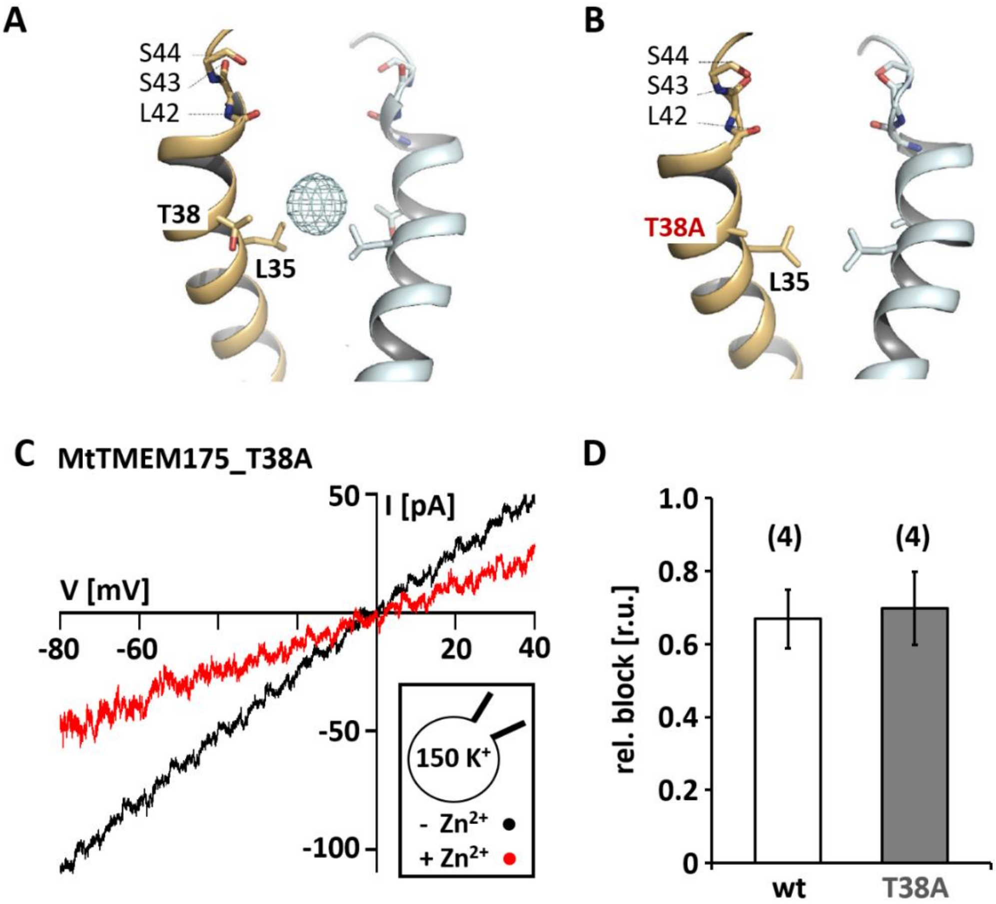

Figure 2.15: Sensitivity to Zn^{2+} and anomalous density of Zn^{2+} in the pore of the MtTMEM175 wt and the T38A mutant. **(A)** Location of Zn^{2+} ions within the pore of MtTMEM175 wt. Anomalous difference electron density of Zn^{2+} is illustrated as cyan mesh (at 2.88 Å, contoured at 4 s, blurred with b = 200). Front and rear subunits are omitted for clarity. **(B)** No Zn^{2+} ions can be detected in the T38A mutant of MtTMEM175 (Fo-Fc density at 3.2 Å, contoured at 4s, blurred with b = 200). **(C)** Representative currents elicited by a ramp protocol (-80 to +40 mV in 200 ms) in HEK293 cells transfected with the MtTMEM175 T38A mutant in absence (black) and presence (red) of 5 mM ZnSO4 in external bath solution containing 150 mM K$^+$. **(D)** Column summarizes average inhibition (± s.d.) of current amplitudes at -60 mV in the MtTMEM175 T38A mutant and wt. Number of patched cells in brackets. (A + B are modified from Brunner et al., 2020; in turn published under CC-BY 4.0)

An unusual finding is the voltage independency of the pore block in hTMEM175 (Figure 2.14B) as this is not expected for a binding site of a charged blocker in the electric field of the channel (Hilf et al., 2010). This absence of a voltage dependency of the block cannot be explained on the basis of the present data. From the combination of structural and functional data it can currently only be speculated that the voltage independent block could originate from the fact that TMEM175 channels spontaneously open and close also at 0 mV. Once they are open, the binding site for the pore blocker is freely accessible and the blocker can bind in the absence of an electrical filed. In this case, the block would be voltage independent. This hypothesis is indirectly supported by structural data. It was found that crystals soaked in Zn^{2+} containing solution exhibited the small Zn^{2+} ion even in the closed channel close to the proposed selectivity filter in the middle of the membrane plane (Figure 2.15A). This indicates that the Zn^{2+} ion (or the 4-AP molecule) is already bound to the selectivity filter before a voltage is applied for eliciting a current. In such a scenario Zn^{2+} would indeed reach the binding site inside the conductive pathway in the absence of voltage and voltage would not affect the strength of the block.

2.4 Conclusion and outlook

Based on the combined structural and electrophysiological analysis, the pore of TMEM175 channels can be divided into distinct functional layers (Figure 2.16). The resulting structure-function correlates are conceptually different from previous interpretations of structural information from another TMEM175 protein (Lee et al., 2017): According to the present data the ion pathway through TMEM175 is built from an ion binding site for monovalent cations. The dimensions of this binding site at the extracellular pore entrance are such that they favor accommodation of K^+ ions. An additional structural layer is formed by a major gate at the position of Leu35 (in MtTMEM175). Finally, a third rather unusual structural layer is made by polar residues that tune K^+ selectivity. While prokaryotic TMEM175 proteins contain one of these layers the eukaryotic homologs have two of these layers in series. These conclusions on structure-function correlates are based on two important considerations. First, scrutiny of the pore in the structure of MtTMEM175 shows that it is too narrow for the passage of ions. This demands that conformational changes have to take place in order to render the channel conductive and to allow entrance of a K^+ ion to the position of $2K^+$ deep in the permeation pathway. Second, there are highly conserved hydrophilic side chains provided by threonine and additionally serine in vertebrate homologs that would be suited for coordinating ions on their passage.

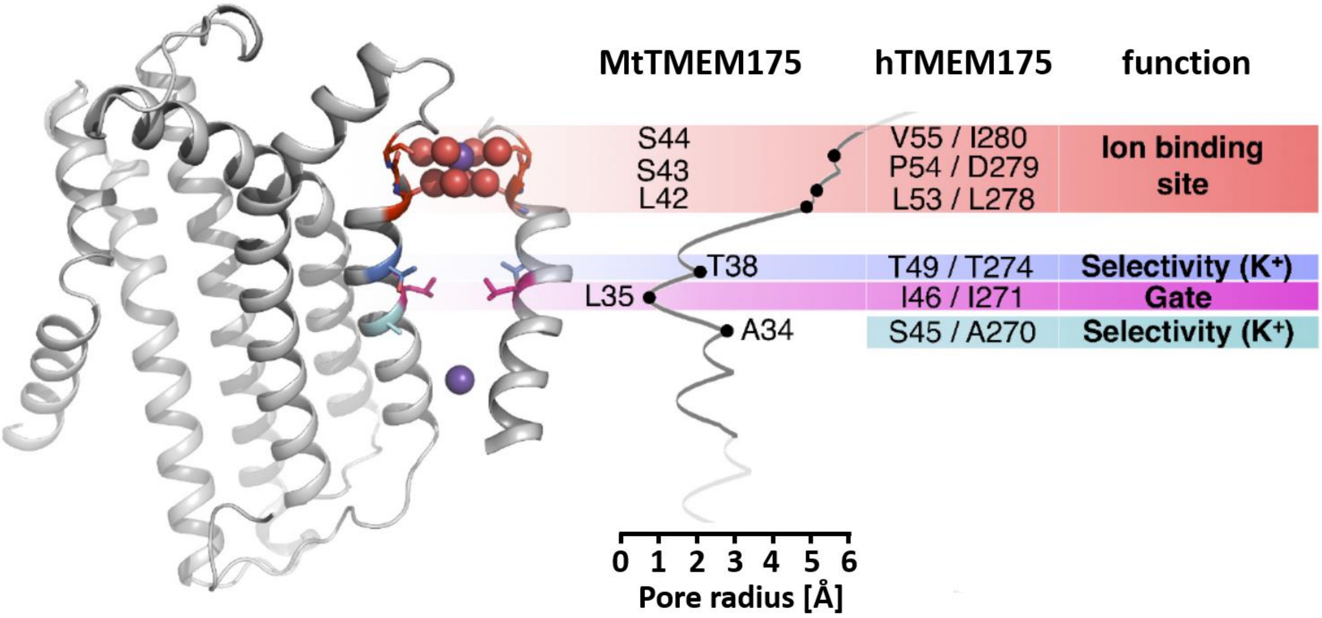

Figure 2.16. Functional layers TMEM175 channels. Functional layers in the MtTMEM175 pore. Two subunits are shown (right side only partly). Important residues in MtTMEM175 and hTMEM175 and for comparison the pore radius (in Å) are indicated. The ion binding site is shown in red, gate-residues in magenta and residues required for selectivity in blue and cyan (modified from Brunner et al., 2020; in turn published under CC-BY 4.0).

But since these residues do not face the pore lumen, i.e. the ion pathway, it can be anticipated that a rotation of helix 1 is required. Such a rotation will presumably result in an iris-like opening of the conductive pathway in TMEM175 channels. The same rotational channel opening simultaneously exposes the hydroxyl-groups of the threonines (Thr38 in MtTMEM175 and Thr49/Thr274 in hTMEM175) and serines (Ser45 in hTMEM175) to the pore lumen and swings the bulky hydrophobic residues (Leu35 in MtTMEM175) out of the conducting pathway (Figure 2.17). This hypothetical scenario is supported by mutational studies in which the respective threonine and serine residues strongly reduced the K$^+$ selectivity both in bacterial and vertebrate TMEM175 channels (Figure 2.12E, F; Figure 2.13C, D).

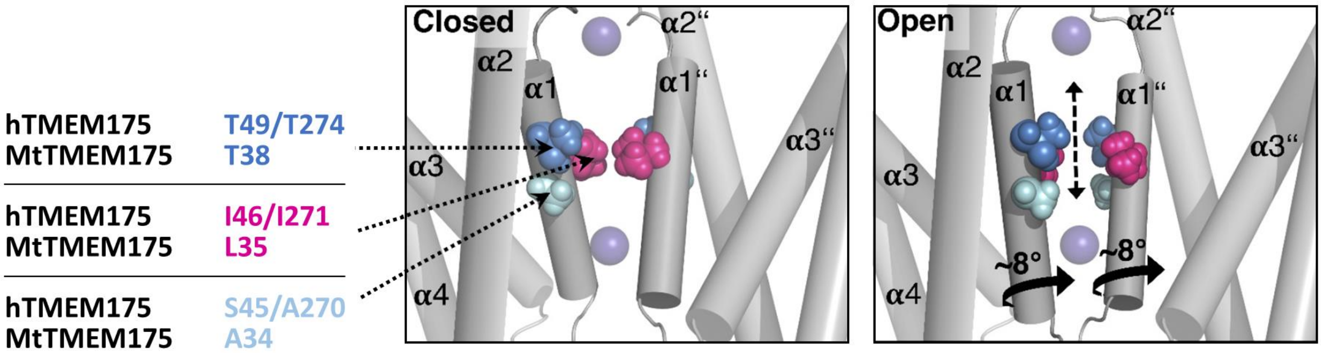

Figure 2.17: Proposed mechanism for channel opening in TMEM175 channels. Schematic side view of MtTMEM175 in closed (left) and proposed conductive state (right). Key residues on helix 1 are shown as spheres. Two subunits are omitted for clarity. K$^+$ ions are shown as purple spheres. A clockwise rotation of helix 1 (viewed from intracellular) of 8–15° would widen the pore sufficiently for K$^+$ ions to permeate (indicated by curved arrows) (modified from Brunner et al., 2020; in turn published under CC-BY 4.0).

TMEM175 channels are not as enigmatic as anticipated earlier but instead recapitulate classical structure-function correlates of other ion channel families: Large hydrophobic residues are acting as gates and polar contacts from side chains and the backbone are coordinating ions in the conducting pathway. The same molecular interactions and structural principles are also known for example from the NaK channel (Alam and Jiang, 2009a) or the TRPV6 channel (McGoldrick et al., 2018).

On the other hand, it is remarkable that the selectivity in TMEM175 channels is mediated by cryptic hydroxyl-bearing side chains inside the pore that are only available for selective ion solvation in an open conformation by concerted repositioning. In conclusion, the conductive state must thus deviate substantially from the closed state in order to be permeable to ions. This is strongly supported by the localization of the residues that mediate K$^+$ selectivity and sensitivity to the blockers Zn^{2+} and 4-AP. Mutational studies suggest that Ser45 is apparently involved in a pore block by Zn^{2+} and 4-AP in hTMEM175 at the site of the selectivity filter. This is underscoring that the respective serine residues are part of the conductive pathway. The data further provide a possible explanation on why bacterial channels are less sensitive to Zn^{2+} and resistant to 4-AP. Notably bacterial TMEM175 channels only have four binding sites for the blockers in their simpler selectivity filter while the eukaryotic homologs have six.

To further support and test this hypothesis, further mutation studies need to be performed. For example, substituting A34 in MtTMEM175 by a serine should raise the number of ligands in its selectivity filter from only four to eight. A subsequent increase in K^+ selectivity of this rather nonselective bacterial channel should be expected from these mutations. Ideally the selectivity should approach the value of the human homolog. The same outcome would be expected from mutating A270 to a serine in hTMEM175, which would also raise the number of binding sites in the filter from six to eight.

This hypothesis about the mechanism of channel opening and gating in the MtTMEM175 channel raise new questions, such as about the stimulus that leads to TMEM175 channel opening. Voltage-gated Kv channels for example are composed of the canonical pore-domain and a N-terminal voltage-sensing domain (VSD), which is formed by four transmembrane segments (S1-S4). The S4 helix of the VSD possesses a series of positively charged residues that act as actual gating charges (Gandhi and Isacoff 2002). In this case a change in the membrane potential, that causes a conformational change in the Kv protein through movement of the S4 helix, affects channel gating. Since TMEM175 channels generate only `leak-like` currents that are not voltage-dependent, it is very unlikely that voltage is the stimulus that gates the channel. Alternatively binding of a ligand could lead to conformational changes in the channel protein that alter pore gating. It was recently reported that hTMEM175 is presumably regulated by direct interaction with protein kinase B (AKT) (Wie et al., 2021). In complex with AKT, hTMEM175 is not opened by the catalytic activity of AKT, but by a conformational change of the latter. Only when AKT was activated by growth factors, hTMEM175 was `switched on` and generated a voltage-independent conductance (Wie et al., 2021). Further studies need to be performed to uncover the mechanistic details of this potential activation mechanism.

2.4.1 An open-state cryo-EM structure provides new insights into ion coordination

Also, a recently published cryo-EM structure of hTEMEM175 in the open state provides some insights into ion coordination and thus into the mechanism of selectivity and gating in TMEM175 channels (Oh et al., 2020). This structural study underlined that the amino acid residues that are crucial for K^+ selectivity and gating in hTMEM175, are identical to those identified in the study on the bacterial MtTMEM175 (Brunner et al. 2020).

Examination of the pore-lining helices 1 and 7 in hTMEM175 reveals that a clockwise rotation of their outer ends from the closed to the open state is accompanied by a straightening of their α-helical conformation, especially in helix 7 (Figure 2.18A, B). From the crystal structures of CmTMEM175 (Ile23) and MtTMEM175 (Leu35) it had been anticipated that in the human homolog Ile46 (R1) and Ile271 (R2) generate a narrow constriction (Brunner et al., 2020; Lee et al., 2017). Comparative analysis of the closed state with the newly obtained open state in hTMEM175 (Oh et al., 2020) confirms the hypothesis that the residues in this position form the gate in TMEM175 channels. Straightening of the pore-lining helices alters the shape of the pore, particularly at the site of the isoleucine constriction (Figure 2.18A, B). In the open state, the minimum radius of the isoleucine constriction is 1.7 Å with an ion binding site in the center surrounded by the isoleucine side chains. In this configuration, the four isoleucine residues are symmetrically facing the pore but pointing to the pore-lining helix of the adjacent subunit, namely helix 1 or 7, respectively. In the closed state, this symmetry is broken due to an inward movement of all four isoleucine residues and a rotation of the Ile271 side chains. These changes reduce the minimum pore radius to 0.5 Å, which is too narrow to accommodate dehydrated K^+ ions (Figure 2.18B; Oh et al., 2020).

By using cryo-EM technology it was also possible to resolve densities inside the open-state protein that were attributed to four K^+ ions in the pore of hTEMEM175 (Figure 2.18C; Oh et al., 2020). The sites are referred to as $1K^+$-$4K^+$ hereafter. Notably in the crystal structure of MtTMEM175 (Brunner et al., 2020), which shows the closed state of the channel, only 2 K^+ ions were identified. Since the densities attributed to the K^+ ions are shown in hTMEM175 only for the open state and in MtTMEM175 only for the closed state, the potential binding sides do not completely match. However, it seems as if the two densities from the crystal structure of MtTMEM175 overlap with the densities at the positions $2K^+$ and $4K^+$ from hTMEM175 with a slight shift in extracellular direction. This could be the case because the open state of hTMEM175 provides enough space for K^+ ions to move to the level of pore-facing hydrophobic residues (e.g. A42). Since MtTMEM175 could only be crystallized in the closed state, there is not enough space at the same level of the hydrophobic residues (e.g. the corresponding A31), so the K^+ ions are forced into the spaces between the layers of hydrophobic residues.

In between the four K^+ ions in the hTMEM175 channel are layers of coordinated water molecules, which are visible as additional densities in the cryo-EM structure (Oh et al., 2020). The most interesting density in the hTMEM175 structure with respect to the data from MtTMEM175 (Brunner et al., 2020) is the $3K^+$ positioned directly at the narrow point of the pore formed by Ile46/Ile271. This constriction is flanked by two layers of four ordered water molecules each (Figure 2.18D, Oh et al., 2020). The cytosolic layer of waters is partially coordinated by Ser45, while the outer layer is partially coordinated by Thr49 and Thr274 (Figure 2.18D, E+F). Unlike the spherical densities resolved at the other ion-binding sites, the density from the $3K^+$ ion is blurred and extends between the two layers of waters on either side of the isoleucine constriction. Because the center of the constriction is hydrophobic, it is unlikely that ions stably bind in this position (Figure 2.18D). It is hence tempting to speculate that the $3K^+$ density corresponds to the sum of two partially-occupied ion-binding sites. These are presumably positioned on either the cytoplasmic or the outer side of the constriction where the ions can be directly coordinated by the nearby waters (Oh et al., 2020).

The results obtained from the cryo-EM structure of hTMEM175 (Oh et al., 2020) are perfectly in line with the electrophysiological data collected in this study. Mutating Ser35 in hTMEM175, the amino acid residue that coordinates the cytosolic layer of water molecules stabilizing the 3 K^+ ion in the cryo-EM structure, resulted in a reduction of K^+ selectivity. An exchange of K^+ for Na^+ in the external solution resulted in a shift in the reversal potential of -58 ± 3 mV (n = 7) for the wt and only -27 ± 2 mV (n = 24) for hTMEM175_S35A (Figure 2.13 C, D). Additionally, a substitution of Thr49 (R1) and Thr274 (R2), stabilizing the outer layer of water molecules, with alanines resulted in an even stronger reduction of K^+ selectivity with a reversal potential of -17 ± 3 mV (n = 8) after exchanging the major cation in the bath solution from K^+ to Na^+ (Figure 2.13C, D). Both amino acid residues which we, based on this data, assumed to play a central role in K^+ selectivity of hTMEM175 are connected with ion stabilization at the critical 3K^+ position.

In summary, the structural data presented in this work as well as in Oh et al., (2020) show that Thr38 (in MtTMEM175) and Thr49/274 together with Ser45 (in hTMEM175) are causally related to K^+ selectivity in TMEM175 channels. Furthermore, both structures show that these hydrophilic residues are not facing the pore but the pore-lining helix of the adjacent subunit. While the structural analysis of the two related TMEM175 channels reveals many common architectural features, the interpretation of the function of the aforementioned Thr and Ser residues as well as the mechanism of channel opening and ion stabilization inside the pore differs a lot between the bacterial channel (Brunner et al., 2020; and this study) and hTMEM175 (Oh et al., 2020). The position of Thr38 suggests that a rotation of the pore-lining helices causes an iris-like opening of the pore (Figure 2.17). As a result, the hydroxyl-groups of Thr38 (in MtTMEM175) and Thr49/274 together with Ser45 (in hTMEM175) become exposed to the pore lumen, where they can stabilize the passing K^+ ions. On the other hand, the data presented in Oh et al., 2020 highlight the existence of layers of water molecules in hTMEM175, which are partially coordinated by Ser45 and Thr49/Thr274, respectively (Figure 2.18 D), which is advocating another mechanism for ion stabilization. In the combination with the water layer, it is more likely, with regard to the open-state hTMEM175 structure, that the ions are only indirectly coordinated by these hydrophilic residues *via* ordered water molecules (Figure 2.18E, F; Oh et al., 2020). In this context the likely mechanism for ion conduction in hTMEM175 is that the K^+ ions are hopping from one binding site to the next where they are stabilized by layers of coordinated water. The bulky hydrophobic residues (e.g. Leu35 in MtTMEM175 and Ile46/I271 in hTMEM175) are in this scenario pointing away from the conducting pathway allowing ion permeation.

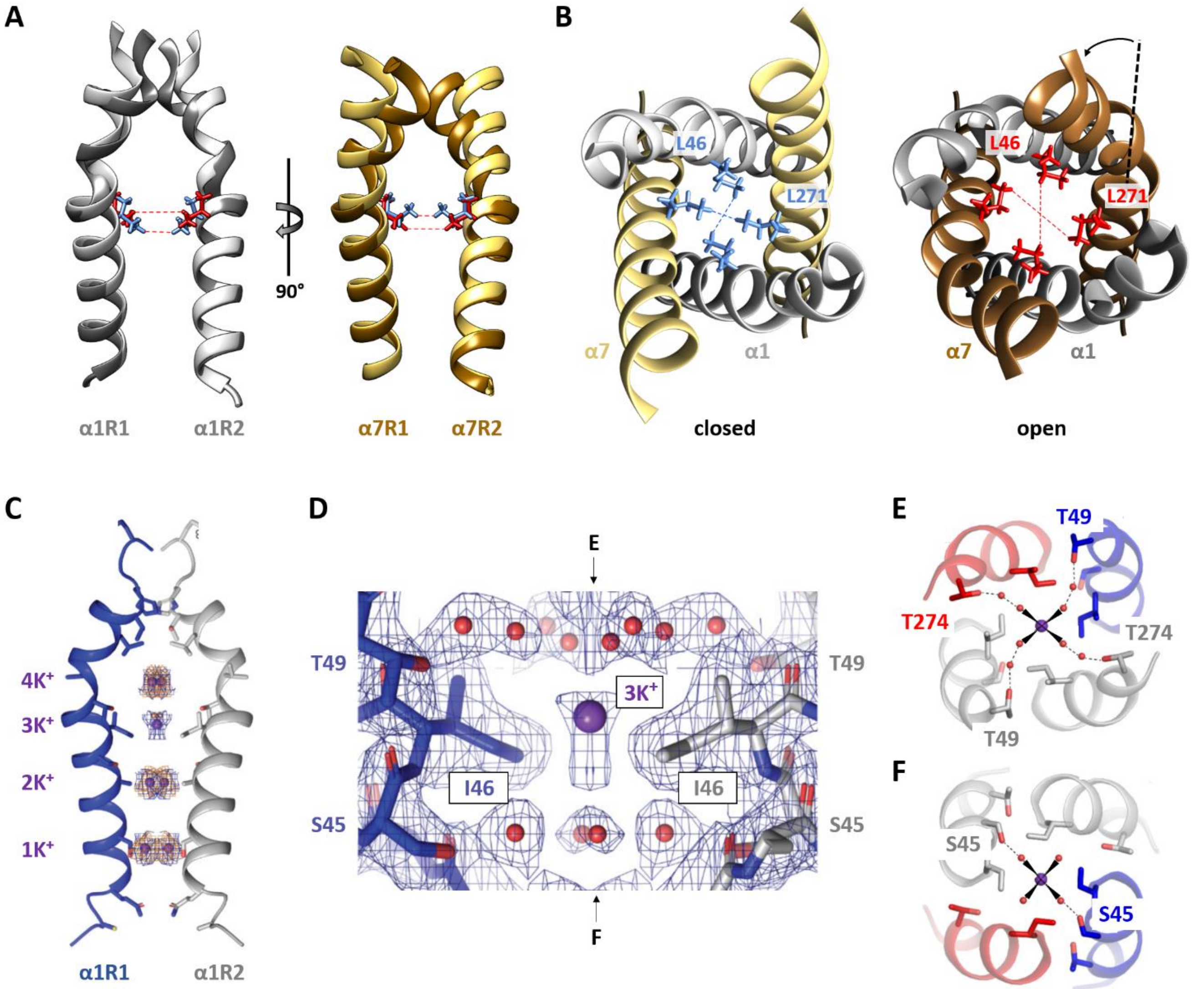

Figure 2.18: Gating mechanism and ion conduction pathway of hTMEM175. (A) Ion conduction pathways of open-state (dark) and closed-state (bright) hTMEM175. Helix 1 is shown at left side in two different shades of grey and helix 7 on the right in two different shades of gold with all other helices removed for clarity. L46 and L271 are highlighted in blue (closed-state) or red (open-state). Dotted lines correspond to minimum distance between opposing residues at the isoleucine constriction. **(B)** Top view on pore-lining helices 1 and 7 of closed-state (left) and open-state (right) hTMEM175 channel. All other helices are omitted for clarity. L46 and L271 are both highlighted in blue (closed-state, left) or red (open-state, right). Dotted blue and red lines correspond to minimum distance between opposing residues at the isoleucine constriction. Tilt of pore-lining helices causing channel opening is indicated in open-state (right) by dotted black line and arrow. **(C)** Overlapping non-protein density peaks in the ion permeation pathway of open-state hTMEM175 in the presence of K^+ (blue mesh) and Cs^+ (gold mesh). K^+ ions are shown as violet spheres. **(D)** Density map near the isoleucine constriction displayed as blue mesh. The K^+ ion bound in $3K^+$ binding site is shown as violet sphere and water molecules are shown as red spheres. **(E+F)** The isoleucine constriction is flanked by two layers of ordered water molecules. The outer layer of waters is partially coordinated by Thr49 and Thr274 (E; top view), while the cytosolic layer is partially coordinated by Ser45 (cytosolic view). Perspectives on the pore are indicated in D. (C-F are modified from Oh et al., 2020; in turn published under CC-BY 4.0) (closed state PDB: 6WCA; open-state PDB: 6WC9)

This hypothesis for the mechanism of channel opening does not necessarily apply to all TMEM175 variants. In general, the level of conservation between different TMEM175 channel homologs is pretty low. For example, Ala48, Met51 and Thr84 of hTMEM175, the amino acid residues that are suspected to order the water molecule stabilizing the kinked formation of helix 1 and which are in this way essential for channel opening in hTMEM175 (Oh et al., 2020), are highly conserved only between the vertebrate homologs. Bacterial variants exhibit different amino acids in the corresponding positions. MtTMEM175, for example, contains Ile37, Leu40 and Cys66, respectively, residues that differ a lot in steric, electrical and hydrophobic properties from those in hTMEM175. Based on their physicochemical properties it seems unlikely that they promote the same kink-like movement as in hTMEM175.

2.4.2 A putative model for hTMEM175 channel gating

In addition to the findings of Oh et al., (2020) on the stabilization of the kinked conformation of the pore-lining helices, also the movement of multiple charged amino acids at the extracellular pore entrance is particularly striking. In the closed state of hTMEM175, the negatively charged residues of amino acids Asp279, Glu282 and Asp283 are pointing out of the pore. Only the positively charged His57 side chain is facing the pore lumen (Figure 2.19A, C). Due to the rotation and kink formation of helix 7 the negatively charged amino acids are turned toward the direction of the pore lumen where they interact with His57 of helix 1 (Figure 2.19B, C, D). This movement leads to a circular arrangement of charged amino acids at the extracellular pore entrance presumably stabilizing the open state of hTMEM175. The interaction of these charged residues seems to be the reason for a helix rotation as well as the kinking of the pore lining helices and the resulting opening of the channel gate (Ile46/271; Figure 2.20). Such a scenario would also explain why helix 7 experiences a stronger rotation, as well as a stronger kinking, than helix 1. His57 of helix 1 is already facing the pore lumen in the closed state and has only to be slightly moved to be in the range where it can interact with both Asp279 and Glu282. The negatively charged residues of helix 7 have to be turned and moved a lot more for interacting with their partner, resulting in a stronger movement of helix 7 itself (Figure 2.19C, Figure 2.20).

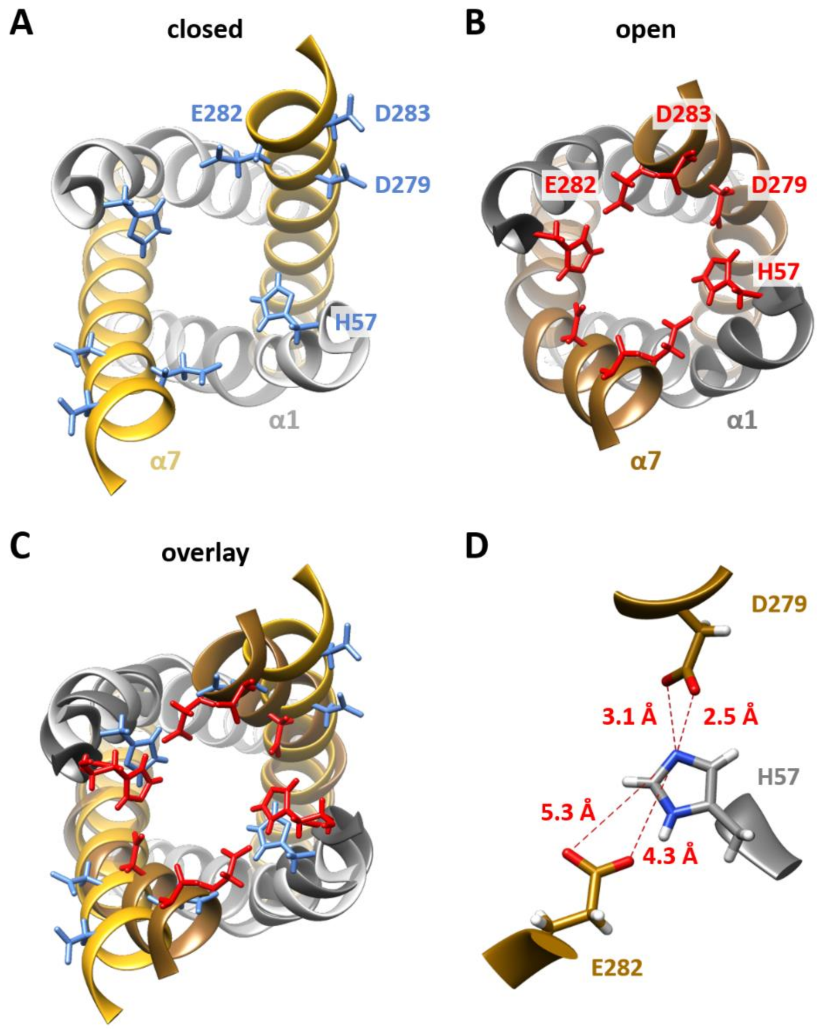

Figure 2.19: Potential mechanism of stabilization of hTMEM175 open state. (A-C) Top view on pore-lining helices 1 and 7 of closed-state (A) and open-state (B) hTMEM175 channel and an overlay of both (C). All other helices are omitted for clarity. H57, D279, E282 and D283 are highlighted in blue (closed-state, A + C) or red (open-state, B + C). **(D)** Distances between the potentially charged atoms of H57 and D279 or H57 and E282 in the open state of hTMEM175. Distances are shown as dashed red lines labeled with distance values in Å. (closed state PDB: 6WCA; open state PDB: 6WC9)

These critical amino acids, which may play a pivotal role in channel gating are highly conserved only between the vertebrate homologs. In the bacterial versions, e.g. MtTMEM175, these charged residues in the corresponding positions are missing. This implies that the gating mechanism in bacterial TMEM175 channels has to be different from the one in hTMEM175. For this hypothetical gating mechanism of hTMEM175, the asymmetrical architecture of this protein is crucial. If all pore-lining helices would exhibit the same amino acids and therefore the same charges, this mechanism would not work due to electrostatical charge repulsion.

The hypothetical gating mechanism is in good agreement with the site of hTMEM175 expression, its journey through the secretory pathway and the target organelle in which hTMEM175 shows its activity. Since membrane proteins of the lysosomes are co-translationally synthesized, the imidazolium group of Histidine with a pK_S value of 6 is initially deprotonated when the nascent protein enters the lumen of the ER with its pH of 7,2 (Paroutis et al., 2004). In the secretory pathway, which sorts the channel to its final destination, hTMEM175 proceeds through the Golgi to the lysosomes. On this journey His57 is exposed to compartments which are becoming progressively more acidic. By being inserted into the lysosomal membranes, the orientation of hTMEM175 is such that the charged amino acids are facing the lysosomal lumen, e.g. a very acidic environment with a pH 4.5-5.5 (Cang et al., 2015; Paroutis et al., 2004). In such an acidic milieu His57 will be protonated. In this scenario the protonation of His57 could promote a rotation and kink formation of the pore-lining helices, thus stabilizing the open state of hTMEM175. This hypothesis is in good agreement with the fact that hTMEM175 is active primarily in lysosomes, but also in late endosomes (Cang et al., 2015), where the pH is lower than the pK_S of Histidine. This means that the stimulus that presumably leads to channel opening in hTMEM175 is the low pH of the lysosomal lumen. Once hTMEM175 incorporates into the lysosomal membrane, the channel activates and generates a `leak-like` current as already published in Cang et al., (2015).

At this point, the proposed gating mechanisms is still speculative and only based on an interpretation of structural data. To test the hypothesis further, patch-clamp experiments on hTMEM175-expressing HEK293 cells in bath solutions with different pH values are essential. In this way, it can be tested whether the activity of hTMEM175 depends on the degree of protonation of His57. Additional mutational studies on the aforementioned charged amino acids could also underpin this hypothesis. In this context, one critical experiment would be to substitute His57 with arginine that is also positively charged and has similar steric properties. The pK_S value of the arginine side chain is with 12.5 way out of the physiologically relevant range. Arginine would be positively charged in every physiological context. Transferred to the hypothesis of hTMEM175 gating this positively charged side chain should stabilize the open state of the channel by interacting with Asp279 and Glu282. In this way, hTMEM175 could be forced into a constitutively open state almost independently of the pH.

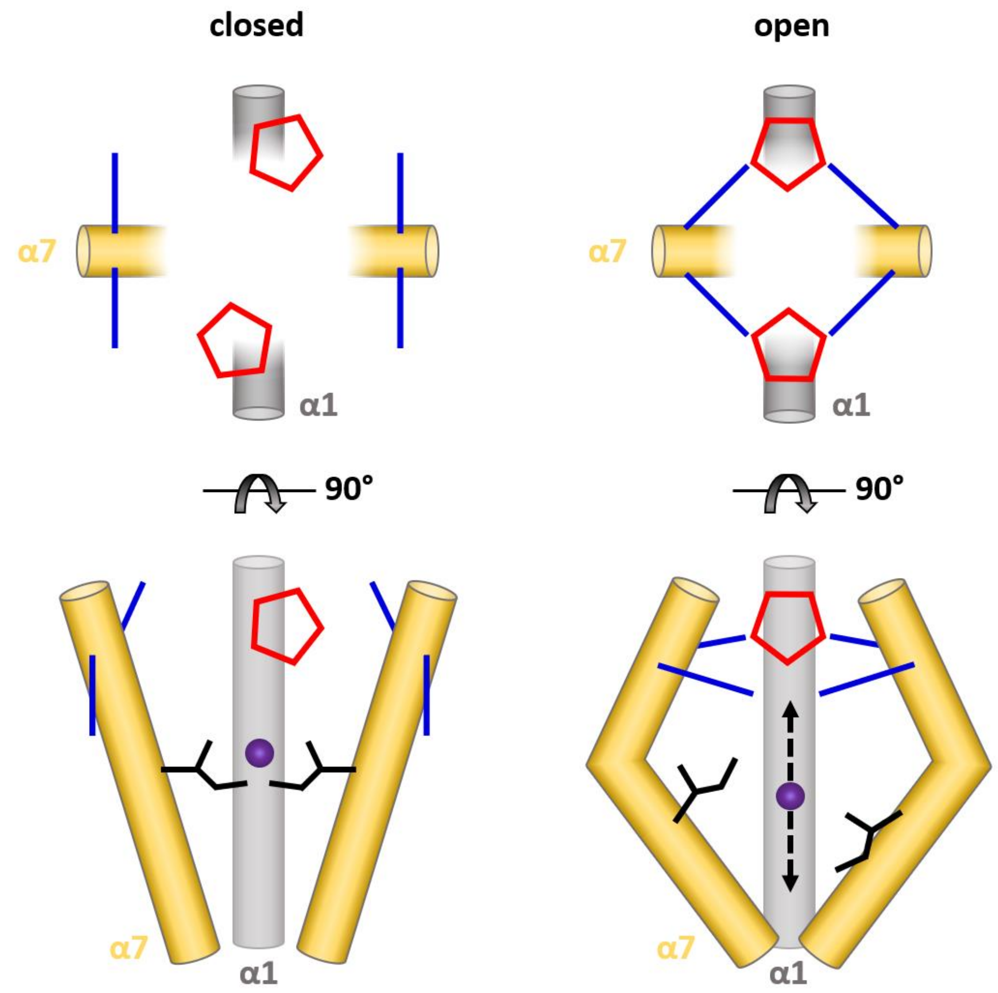

Figure 2.20: Potential mechanism of hTMEM175 channel gating. Scheme of top (top) and side view (bottom) on pore-lining helices 1 (grey) and 7 (yellow) of closed-state (left) and open-state (right) hTMEM175. All other helices are omitted for clarity. The positively charged H57 is illustrated as red pentagon and the negatively charged D279 + E282 as blue lines. Black lines show Ile271 which is suspected to be the channel gate. Violet sphere is indicating a K^+ ion that is only able to pass through the pore due to the opening of the gate.

Collectively, this study, which combines structural and functional data on TMEM175 proteins, provides insight into a potential and alternative solution for conduction of K^+ ions in these newly detected channel proteins. The data provide a coherent description of selectivity, blocking, and channel opening based on an unusual selectivity filter in TMEM175 channels. Interesting to note is that these channels recapitulate, in spite of their unique architecture, many established structural and physico-chemical concepts that are also found in canonical K^+ channels as basis of selectivity. This includes the geometry and chemistry of the filter as well as the number of cation binding sites. Close scrutiny of the channel structures furthermore provides a coherent hypothesis on the mechanism of channel gating in hTMEM175, which can be experimentally tested.

2.5 Material and methods

2.5.1 Cloning

For electrophysiology and expression in HEK293 cells, the TMEM175 genes were cloned without tags into the plasmids pcDXC3MS (Brunner et al., 2014; Schenck et al., 2017) (Addgene #49030) followed by a stop-codon as well as into the vector pcDXC3GMS (Brunner et al., 2014; Schenck et al., 2017) (Addgene #49031) (where EGFP was replaced by Venus-YFP (vYFP) using the KpnI sites) to obtain a C-terminally vYFP tagged channel. Both, tagged and untagged versions yielded similar results. For TIRF microscopy the TMEM175 genes were cloned into the vector pcDXC3GMS (Brunner et al., 2014; Schenck et al., 2017) (Addgene #49031) to produce a fusion to vYFP. Mutant proteins were generated by site-directed mutagenesis. All constructs were verified by Sanger sequencing. For cell free expression performed for planar lipid bilayer experiments the MtTMEM175_wt gene, followed by a stop-codon, was cloned in a pET-based vector (p7x-C) baring a Lac-repressor.

All plasmids were provided by Janine Brunner (Department of Biochemistry, University of Zürich, Zürich, Switzerland).

2.5.2 Cell culture and transfection protocol

Membrane currents were recorded from HEK293 cells transiently expressing TMEM175 proteins. For this low passage human embryonic kidney (HEK293) cells were cultured in Dulbecco’s modified Eagle’s medium supplemented with 10% fetal bovine serum, 100 IU/mL of penicillin, 100 mg/ml of streptomycin, and stored in a 37°C humidified incubator with 5% CO_2. Transfections were performed with TransfeX^{TM} Transfection Reagent (ATCC, Manassas, Virginia, USA) according the producer protocol: The MtTMEM175 genes inserted in pcDXC3MS (Brunner et al., 2014; Schenck et al., 2017) were co-transfected with a plasmid containing green fluorescent protein (GFP) and incubated in dark. Human TMEM175 constructs were cloned into pcDXC3GMS (Brunner et al., 2014; Schenck et al., 2017) with a C-terminal vYFP tag.

2.5.3 TIRF microscopy

HEK293 cells transiently expressing vYFP-tagged TMEM175 proteins were grown on cover slips and decapitated by cold distilled water as described previously (Biel et al., 2016). The remaining isolated PM patches on the glass cover slips were imaged on a Nikon Ti-E microscope (Nikon, Konan, Minato-ku, Tokyo, Japan) with a CFI Apo TIRF 100x objective (NA 1.49, WD 0.12 mm). For TIRF imaging the focus in the back focal plane was moved off-center by controlling the position of a mirror with a single-axis stage M-126. DG controlled by a C-863 Mercury Servo Controller (Physik Instrumente (PI), Karlsruhe, Germany). PM patches and potential contamination of remaining cortical ER were stained with red fluorescent CellMask Deep Red (CMDR) and ER-tracker Blue-white DPX (both from Thermo Fisher) respectively. The fluorescent markers were excited/detected as follows: vYFP (488 nm/ 500–550 nm), ER-Tracker (561 nm/ 577.5–646.5 nm), CMDR (647 nm/ 662.5–799.5 nm).

2.5.4 Patch clamp recordings

One to two days after transfection, cells were dispersed by accutase treatment and seeded on 35 mm plastic petri dishes (on 15 mm cover slips) to allow single cell measurements. Green fluorescent cells were selected for patch clamp measurements. Membrane currents were recorded in whole-cell configuration using an EPC9 or EPC10 patch-clamp amplifier (HEKA Electronics) controlled by the PatchMaster software (HEKA). Micropipettes with a resistance of about 2 MW were made from 1.5 mm thin-walled glass and fire-polished. The pipette solution contained (in mM) 150 KOH, 5 HCl, 10 HEPES, pH 7.4, titrated with methanesulfonic acid. The standard bath solution contained (in mM) 150 KOH, 1 $CaCl_2$, 1 $MgCl_2$, 10 TEA, 10 HEPES/KOH, pH 7.4, titrated with methanesulfonic acid. For measurements of selectivity K^+ was replaced by other cations of interest. Relevant liquid junction voltages were calculated with JPCalcWin (UNSW Sydney). Differences in osmolarity between pipette and bath solution were compensated by D-mannitol. Membrane currents were either measured by voltage step- or ramp protocols. In standard step protocol the cell was clamped for 200 ms in 20 mV steps from holding voltage (0 mV, 100 ms) to test voltages between ±100 mV before returning to holding voltage (100 ms). The steady state current at the test voltages was measured during the final 20 ms of clamp steps. In ramp protocols the voltage increased from a holding voltage (-80 mV, 20 ms) in 200 ms to +40 mV (20 ms).

2.5.5 *In vitro* Protein expression and purification

In vitro expression of MtTMEM175 was done using the MembraneMax Protein Expression System (ThermoFisher Scientific, Waltham, MA, USA) following manufacturer’s instructions. In brief, the cell-free expression takes place in the presence of nanodiscs (Katzen, 2008) fused with multiple His-tags. 1 µg of template DNA (p7x-C/MtTMEM175_Stop) was added to the transcription/translation reaction mixture in the presence of 0.5 mM IPTG and pre-assembled human MSP2N2-His DMPC nanodiscs (Cube Biotech GmbH, Monheim, Germany). After initial incubation for 30 min at 30°C and 1250 rpm, feeding buffer was added and incubation was continued for additional 3 hours. The reaction mixture was then added to a 0.2 mL HisPur Ni-NTA Spin column (ThermoFisher Scientific, Waltham, MA, USA), pre-equilibrated with a solution containing 20 mM Na_3Po_4, 300 mM NaCl and 10 mM imidazole adjusted to pH 7.4 and incubated at constant shaking for 30 min at 37°C. Flow through was collected at 700 x g for 2 min. The column was then washed three times with 400 µL imidazole (20 mM) adjusted to pH 7.4 and finally proteins were eluted three times using 200 µL imidazole (250 mM) adjusted to pH 7.4.

2.5.6 Single channel analysis *via* Planar Lipid Bilayer technique

Recordings of MtTMEM175 mediated channel activity were performed in vertical lipid bilayers by voltage clamp recordings. Both chambers were connected with Ag/AgCl electrodes to the head-stage of a patch-clamp amplifier (L/M-EPC-7, List-Medical, Darmstadt). Membrane potentials were referred to the cis compartment. Current traces were low-pass filtered at 1 kHz with a 4-pole Bessel filter and digitized with a sampling frequency of 5 kHz by an A/D-converter (LIH 1600, HEKA Elektronik, Lambrecht, Germany). DPhPC (1,2-diphytanoyl-sn-glycero-3-phosphocholine) bilayers with 10% cholesterol (Avanti Polar Lipids; Alabaster, AL, USA) were formed by the Pseudo painting/air bubble technique (Braun et al., 2014) in symmetrical 100 mM KCl solution (pH 7, buffered with 10 mM HEPES). For reconstitution of channel proteins, a small amount (1-2 µL) of the purified protein-bearing nanodiscs diluted in 250 mM imidazole solution was added directly below the bilayer in the trans compartment with a bent Hamilton syringe. After successful incorporation of a single channel in the DPhPC bilayer, constant voltages were applied for 1 to 5 min. Voltage was changed in steps of 20 mV between +160 mV and -160 mV. Single-channel current traces were recorded with Patchmaster (HEKA) and digitally filtered with 0.3 kHz. Analysis of single channel amplitudes was performed visually with the custom-made program Kielpatch (http://www.zbm.uni-kiel.de/aghansen/ software.html).

2.6 References

Alam A, Jiang Y. 2009a. High-resolution structure of the open NaK channel. Nature Structural & Molecular Biology 16:30–34. DOI: https://doi.org/10.1038/nsmb.1531, PMID: 19098917

Alam A, Jiang Y. 2009b. Structural analysis of ion selectivity in the NaK channel. Nature Structural & Molecular Biology 16:35–41. DOI: https://doi.org/10.1038/nsmb.1537, PMID: 19098915

Aryal P, Abd-Wahab F, Bucci G, Sansom MS, Tucker SJ. 2014. A hydrophobic barrier deep within the inner pore of the TWIK-1 K2P potassium channel. Nature Communications 5:4377. DOI: https://doi.org/10.1038/ncomms5377, PMID: 25001086

Baker NA, Sept D, Joseph S, Holst MJ, McCammon JA. 2001. Electrostatics of nanosystems: Application to microtubules and the ribosome. PNAS 98:10037–10041. DOI: https://doi.org/10.1073/pnas. 181342398 , PMID: 11517324

Ballabio A, Bonifacino JS. 2020. Lysosomes as dynamic regulators of cell and organismal homeostasis. Nature Reviews Molecular Cell Biology 21:101–118. DOI: https://doi.org/10.1038/s41580-019-0185-4, PMID: 31768005

Biel S, Aquila M, Hertel B, Berthold A, Neumann T, DiFrancesco D, Moroni A, Thiel G, Kauferstein S. 2016. Mutation in S6 domain of HCN4 channel in patient with suspected brugada syndrome modifies channel function. Pflu¨gers Archiv - European Journal of Physiology 468:1663–1671. DOI: https://doi.org/10.1007/s00424-016-1870-1, PMID: 27553229

Blanc E, Roversi P, Vonrhein C, Flensburg C, Lea SM, Bricogne G. 2004. Refinement of severely incomplete structures with maximum likelihood in BUSTER-TNT. Acta Crystallographica Section D Biological Crystallography 60:2210–2221. DOI: https://doi.org/10.1107/S0907444904016427, PMID: 15572774

Braun CJ, Baer T, Moroni A, Thiel G. 2014. Pseudo painting/air bubble technique for planar lipid bilayers. J Neurosci Methods 15:233:13-7. Doi: 10.1016/j.jneumeth.2014.05.031, PMID: 24938397

Brunner JD, Lim NK, Schenck S, Duerst A, Dutzler R. 2014. X-ray structure of a calcium-activated TMEM16 lipid scramblase. Nature 516:207–212. DOI: https://doi.org/10.1038/nature13984, PMID: 25383531

Brunner JD, Jakob RP, Schulze T, Neldner Y, Moroni A, Thiel G, Maier T, Schenck S. 2020. Structural basis for ion selectivity in TMEM175 K(+) channels. eLife 8;9:e53683. DOI: 10.7554/eLife.53683, PMID: 32267231

Cang C, Aranda K, Seo YJ, Gasnier B, Ren D. 2015. TMEM175 is an organelle K(+) Channel regulating lysosomal function. Cell 162:1101–1112. DOI: https://doi.org/10.1016/j.cell.2015.08.002, PMID: 26317472

Chang D, Nalls MA, Hallgrı´msdo´ ttir IB, Hunkapiller J, van der Brug M, Cai F, Kerchner GA, Ayalon G, Bingol B, Sheng M, Hinds D, Behrens TW, Singleton AB, Bhangale TR, Graham RR, International Parkinson’s Disease Genomics Consortium, 23andMe Research Team,. 2017. A meta-analysis of genome-wide association studies identifies 17 new parkinson’s disease risk loci. Nature Genetics 49:1511–1516. DOI: https://doi.org/10.1038/ng.3955, PMID: 28892059

Chatelain FC, Gazzarrini S, Fujiwara Y, Arrigoni C, Domigan C, Ferrara G, Pantoja C, Thiel G, Moroni A, Minor DL. 2009. Selection of Inhibitor-Resistant viral potassium channels identifies a selectivity filter site that affects barium and amantadine block. PLOS ONE 4:e7496. DOI: https://doi.org/10.1371/journal.pone.0007496

Chen Q, She J, Zeng W, Guo J, Xu H, Bai XC, Jiang Y. 2017. Structure of mammalian endolysosomal TRPML1 channel in nanodiscs. Nature 550:415–418. DOI: https://doi.org/10.1038/nature24035, PMID: 29019981

Cowtan K. 2006. The buccaneer software for automated model building. 1. tracing protein chains. Acta Crystallographica. Section D, Biological Crystallography 62:1002–1011. DOI: https://doi.org/10.1107/S0907444906022116, PMID: 16929101

Cowtan K. 2010. Recent developments in classical density modification. Acta Crystallographica Section D Biological Crystallography 66:470–478. DOI: https://doi.org/10.1107/S090744490903947X, PMID: 20383000

Derebe MG, Sauer DB, Zeng W, Alam A, Shi N, Jiang Y. 2011. Tuning the ion selectivity of tetrameric cation channels by changing the number of ion binding sites. PNAS 108:598–602. DOI: https://doi.org/10.1073/pnas.1013636108, PMID: 21187421

Doyle DA, Morais Cabral J, Pfuetzner RA, Kuo A, Gulbis JM, Cohen SL, Chait BT, MacKinnon R. 1998. The structure of the potassium channel: molecular basis of K+ conduction and selectivity. Science 280:69–77. DOI: https://doi.org/10.1126/science.280.5360.69, PMID: 9525859

Ehrnstorfer IA, Geertsma ER, Pardon E, Steyaert J, Dutzler R. 2014. Crystal structure of a SLC11 (NRAMP) transporter reveals the basis for transition-metal ion transport. Nature Structural & Molecular Biology 21:990– 996. DOI: https://doi.org/10.1038/nsmb.2904

Emsley P, Lohkamp B, Scott WG, Cowtan K. 2010. Features and development of coot. Acta Crystallographica. Section D, Biological Crystallography 66:486–501. DOI: https://doi.org/10.1107/S0907444910007493, PMID: 20383002

Feng X, Zhao Z, Li Q, Tan Z. 2018. Lysosomal potassium channels: potential roles in lysosomal function and neurodegenerative diseases. CNS & Neurological Disorders Drug Targets 17:261–266. DOI: https://doi.org/10.2174/1871527317666180202110717, PMID: 29422008

Gandhi CS and Isacoff EY. 2002. Molecular Models of Voltage Sensing. J Gen Physiol. 120(4): 455–463. DOI: 10.1085/jgp.20028678, PMCID: PMC2229531

Geertsma ER, Chang YN, Shaik FR, Neldner Y, Pardon E, Steyaert J, Dutzler R. 2015. Structure of a prokaryotic fumarate transporter reveals the architecture of the SLC26 family. Nature Structural & Molecular Biology 22: 803–808. DOI: https://doi.org/10.1038/nsmb.3091, PMID: 26367249

Geertsma ER, Dutzler R. 2011. A versatile and efficient high-throughput cloning tool for structural biology. Biochemistry 50:3272–3278. DOI: https://doi.org/10.1021/bi200178z, PMID: 21410291

Gouaux E, Mackinnon R. 2005. Principles of selective ion transport in channels and pumps. Science 310:1461– 1465. DOI: https://doi.org/10.1126/science.1113666, PMID: 16322449

Grimm C, Butz E, Chen CC, Wahl-Schott C, Biel M. 2017. From mucolipidosis type IV to ebola: trpml and two-pore channels at the crossroads of endo-lysosomal trafficking and disease. Cell Calcium 67:148–155. DOI: https://doi.org/10.1016/j.ceca.2017.04.003, PMID: 28457591

Guo J, She J, Zeng W, Chen Q, Bai XC, Jiang Y. 2017. Structures of the calcium-activated, non-selective cation channel TRPM4. Nature 552:205–209. DOI: https://doi.org/10.1038/nature24997, PMID: 29211714

Henning R. 1975. pH gradient across the lysosomal membrane generated by selective cation permeability and Donnan equilibrium. Biochimica Et Biophysica Acta (BBA) - Biomembranes 401:307–316. DOI: https://doi.org/10.1016/0005-2736(75)90314-4

Hilf RJ, Bertozzi C, Zimmermann I, Reiter A, Trauner D, Dutzler R. 2010. Structural basis of open channel block in a prokaryotic pentameric ligand-gated ion channel. Nature Structural & Molecular Biology 17:1330–1336. DOI: https://doi.org/10.1038/nsmb.1933, PMID: 21037567

Jinn S, Drolet RE, Cramer PE, Wong AH, Toolan DM, Gretzula CA, Voleti B, Vassileva G, Disa J, Tadin-Strapps M, Stone DJ. 2017. TMEM175 deficiency impairs lysosomal and mitochondrial function and increases a-synuclein aggregation. PNAS 114:2389-2394. DOI: https://doi.org/10.1073/pnas. 1616332114, PMID: 28193887

Jinn S, Blauwendraat C, Toolan D, Gretzula CA, Drolet RE, Smith S, Nalls MA, Marcus J, Singleton AB, Stone DJ. 2019. Functionalization of the TMEM175 p.m393t variant as a risk factor for parkinson disease. Human Molecular Genetics 28:3244–3254. DOI: https://doi.org/10.1093/hmg/ddz136, PMID: 31261387

Kabsch W. 2010a. XDS. Acta Crystallogr D Biol Crystallogr 66:125–132. DOI: https://doi.org/10.1107/S0907444909047337

Kabsch W. 2010b. Integration, scaling, space-group assignment and post-refinement. Acta Crystallographica Section D Biological Crystallography 66:133–144. DOI: https://doi.org/10.1107/ S0907444909047374, PMID: 20124693

Kane Dickson V, Pedi L, Long SB. 2014. Structure and insights into the function of a Ca(2+)-activated Cl(-) channel. Nature 516:213–218. DOI: https://doi.org/10.1038/nature13913, PMID: 25337878

Karplus PA, Diederichs K. 2012. Linking crystallographic model and data quality. Science 336:1030–1033. DOI: https://doi.org/10.1126/science.1218231, PMID: 22628654

Kast SM, Kloss T, Tayefeh S, Thiel G. 2011. A minimalist model for ion partitioning and competition in a K+ channel selectivity filter. The Journal of General Physiology 138:371–373. DOI: https://doi.org/ 10.1085/jgp.201110694, PMID: 21875982

Katzen F, Fletcher JE, Yang JP, Vasu S, Peterson T, Kudlicki W. 2008. Cell-free protein expression of membrane proteins using nanolipoprotein particles. Biotechniques 45(4):469. Doi: 10.2144/000112996, PMID: 18949886

Keefe AD, Wilson DS, Seelig B, Szostak JW. 2001. One-step purification of recombinant proteins using a nanomolar-affinity streptavidin-binding peptide, the SBP-Tag. Protein Expression and Purification 23:440–446. DOI: https://doi.org/10.1006/prep.2001.1515, PMID: 11722181

Krishnan MN, Trombley P, Moczydlowski EG. 2008. Thermal stability of the K+ channel tetramer: cation interactions and the conserved threonine residue at the innermost site (S4) of the KcsA selectivity filter. Biochemistry 47:5354–5367. DOI: https://doi.org/10.1021/bi702281p, PMID: 18419132

Lamming DW, Bar-Peled L. 2019. Lysosome: the metabolic signaling hub. Traffic 20:27–38. DOI: https://doi.org/10.1111/tra.12617, PMID: 30306667

Laverty D, Desai R, Uchan´ ski T, Masiulis S, Stec WJ, Malinauskas T, Zivanov J, Pardon E, Steyaert J, Miller KW, Aricescu AR. 2019. Cryo-EM structure of the human a1b3g2 GABAA receptor in a lipid bilayer. Nature 565:516–520. DOI: https://doi.org/10.1038/s41586-018-0833-4, PMID: 30602789

Lawrence RE, Zoncu R. 2019. The lysosome as a cellular centre for signalling, metabolism and quality control. Nature Cell Biology 21:133–142. DOI: https://doi.org/10.1038/s41556-018-0244-7, PMID: 30602725

Lee C, Guo J, Zeng W, Kim S, She J, Cang C, Ren D, Jiang Y. 2017. The lysosomal potassium channel TMEM175 adopts a novel tetrameric architecture. Nature 547:472–475. DOI: https://doi.org/10.1038/nature23269, PMID: 28723891

Lee C-H, MacKinnon R. 2017. Structures of the human HCN1 Hyperpolarization-Activated channel. Cell 168:111–120. DOI: https://doi.org/10.1016/j.cell.2016.12.023

Li P, Gu M, Xu H. 2019. Lysosomal ion channels as decoders of cellular signals. Trends in Biochemical Sciences 44:110–124. DOI: https://doi.org/10.1016/j.tibs.2018.10.006, PMID: 30424907

Long SB, Campbell EB, Mackinnon R. 2005. Crystal structure of a mammalian voltage-dependent shaker family K+ channel. Science 309:897–903. DOI: https://doi.org/10.1126/science.1116269, PMID: 16002581

McCoy AJ, Grosse-Kunstleve RW, Adams PD, Winn MD, Storoni LC, Read RJ. 2007. Phaser crystallographic software. Journal of Applied Crystallography 40:658–674. DOI: https://doi.org/10.1107/S0021889807021206, PMID: 19461840

McGoldrick LL, Singh AK, Saotome K, Yelshanskaya MV, Twomey EC, Grassucci RA, Sobolevsky AI. 2018. Opening of the human epithelial calcium channel TRPV6. Nature 553:233–237. DOI: https://doi.org/10.1038/nature25182, PMID: 29258289

Miller AN, Vaisey G, Long SB. 2019. Molecular mechanisms of gating in the calcium-activated chloride channel bestrophin. eLife 8:e43231. DOI: https://doi.org/10.7554/eLife.43231, PMID: 30628889

Murshudov GN, Skuba´ k P, Lebedev AA, Pannu NS, Steiner RA, Nicholls RA, Winn MD, Long F, Vagin AA. 2011. REFMAC5 for the refinement of macromolecular crystal structures. Acta Crystallographica Section D Biological Crystallography 67:355–367. DOI: https://doi.org/10.1107/S0907444911001314, PMID: 21460454

Nalls MA, Pankratz N, Lill CM, Do CB, Hernandez DG, Saad M, DeStefano AL, Kara E, Bras J, Sharma M, Schulte C, Keller MF, Arepalli S, Letson C, Edsall C, Stefansson H, Liu X, Pliner H, Lee JH, Cheng R. 2014. Large- scale meta-analysis of genome-wide association data identifies six new risk loci for parkinson’s disease. Nature Genetics 46:989–993. DOI: https://doi.org/10.1038/ng.3043, PMID: 25064009

Oh S, Paknejad N, Hite RK. 2020. Gating and selectivity mechanisms for the lysosomal K(+) channel TMEM175. eLife 31;9:e53430. DOI: 10.7554/eLife.53430, PMID: 32228865

Paroutis P, Touret N, Grinstein S. 2004. The pH of the secretory pathway: measurement, determinants, and regulation. Physiology (Bethesda). 19:207-15. DOI: 10.1152/physiol.00005.2004, PMID: 15304635

Pei J, Grishin NV. 2001. AL2CO: calculation of positional conservation in a protein sequence alignment. Bioinformatics 17:700–712. DOI: https://doi.org/10.1093/bioinformatics/17.8.700, PMID: 11524371

Perera RM, Zoncu R. 2016. The lysosome as a regulatory hub. Annual Review of Cell and Developmental Biology 32:223–253. DOI: https://doi.org/10.1146/annurev-cellbio-111315-125125, PMID: 27501449

Quiocho FA, Spurlino JC, Rodseth LE. 1997. Extensive features of tight oligosaccharide binding revealed in high- resolution structures of the maltodextrin transport/chemosensory receptor. Structure 5:997–1015. DOI: https://doi.org/10.1016/S0969-2126(97)00253-0

Rao S, Klesse G, Stansfeld PJ, Tucker SJ, Sansom MSP. 2017. A BEST example of channel structure annotation by molecular simulation. Channels 11:347–353. DOI: https://doi.org/10.1080/19336950.2017.1306163, PMID: 28319451

Rao S, Lynch CI, Klesse G, Oakley GE, Stansfeld PJ, Tucker SJ, Sansom MSP. 2018. Water and hydrophobic gates in ion channels and nanopores. Faraday Discussions 209:231–247. DOI: https://doi.org/10.1039/C8FD00013A, PMID: 29969132

Sauer DB, Zeng W, Canty J, Lam Y, Jiang Y. 2013. Sodium and potassium competition in potassium-selective and non-selective channels. Nature Communications 4:2721. DOI: https://doi.org/10.1038/ncomms3721, PMID: 24217363

Schenck S, Kunz L, Sahlender D, Pardon E, Geertsma ER, Savtchouk I, Suzuki T, Neldner Y, Sˇ tefanic´ S, Steyaert J, Volterra A, Dutzler R. 2017. Generation and characterization of Anti-VGLUT nanobodies acting as inhibitors of transport. Biochemistry 56:3962–3971. DOI: https://doi.org/10.1021/acs.biochem.7b00436, PMID: 28731329

Schindelin J, Arganda-Carreras I, Frise E, Kaynig V, Longair M, Pietzsch T, Preibisch S, Rueden C, Saalfeld S, Schmid B, Tinevez JY, White DJ, Hartenstein V, Eliceiri K, Tomancak P, Cardona A. 2012. Fiji: an open-source platform for biological-image analysis. Nature Methods 9:676–682. DOI: https://doi.org/10.1038/nmeth.2019, PMID: 22743772

Shen PS, Yang X, DeCaen PG, Liu X, Bulkley D, Clapham DE, Cao E. 2016. The structure of the polycystic kidney disease channel PKD2 in lipid nanodiscs. Cell 167:763–773. DOI: https://doi.org/10.1016/j.cell.2016.09.048

Smart OS, Goodfellow JM, Wallace BA. 1993. The pore dimensions of gramicidin A. Biophysical Journal 65:2455–2460. DOI: https://doi.org/10.1016/S0006-3495(93)81293-1, PMID: 7508762

Staus DP, Strachan RT, Manglik A, Pani B, Kahsai AW, Kim TH, Wingler LM, Ahn S, Chatterjee A, Masoudi A, Kruse AC, Pardon E, Steyaert J, Weis WI, Prosser RS, Kobilka BK, Costa T, Lefkowitz RJ. 2016. Allosteric nanobodies reveal the dynamic range and diverse mechanisms of G-protein-coupled receptor activation. Nature 535:448–452. DOI: https://doi.org/10.1038/nature18636, PMID: 27409812

Su M, Gao F, Yuan Q, Mao Y, Li DL, Guo Y, Yang C, Wang XH, Bruni R, Kloss B, Zhao H, Zeng Y, Zhang FB, Marks AR, Hendrickson WA, Chen YH. 2017. Structural basis for conductance through TRIC cation channels. Nature Communications 8:15103. DOI: https://doi.org/10.1038/ncomms15103, PMID: 28524849

Tao X, Hite RK, MacKinnon R. 2017. Cryo-EM structure of the open high-conductance Ca2+-activated K+ channel. Nature 541:46–51. DOI: https://doi.org/10.1038/nature20608

Vaisey G, Miller AN, Long SB. 2016. Distinct regions that control ion selectivity and calcium-dependent activation in the bestrophin ion channel. PNAS 113:E7399–E7408. DOI: https://doi.org/10.1073/pnas.1614688113, PMID: 27821745

van Veen S, Martin S, Van den Haute C, Benoy V, Lyons J, Vanhoutte R, Kahler JP, Decuypere JP, Gelders G, Lambie E, Zielich J, Swinnen JV, Annaert W, Agostinis P, Ghesquie` re B, Verhelst S, Baekelandt V, Eggermont J, Vangheluwe P. 2020. ATP13A2 deficiency disrupts lysosomal polyamine export. Nature 578:419–424. DOI: https://doi.org/10.1038/s41586-020-1968-7, PMID: 31996848

Vieira-Pires RS, Morais-Cabral JH. 2010. 3(10) helices in channels and other membrane proteins. Journal of General Physiology 136:585–592. DOI: https://doi.org/10.1085/jgp.201010508, PMID: 21115694

Wie J, Liu Z, Song H, Tropea TF, Yang L, Wang H, Liang Y, Cang C, Aranda K, Lohmann J, Yang J, Lu B, Chen-Plotkin AS, Luk KC, Ren D. 2021. A growth-factor-activated lysosomal K(+) channel regulates Parkinson’s pathology. Nature 591(7850):431-437. Doi: 10.1038/s41586-021-03185-z. PMID: 33505021

Winn MD, Ballard CC, Cowtan KD, Dodson EJ, Emsley P, Evans PR, Keegan RM, Krissinel EB, Leslie AG, McCoy A, McNicholas SJ, Murshudov GN, Pannu NS, Potterton EA, Powell HR, Read RJ, Vagin A, Wilson KS. 2011. Overview of the CCP4 suite and current developments. Acta Crystallographica. Section D, Biological Crystallography 67:235–242. DOI: https://doi.org/10.1107/S0907444910045749, PMID: 21460441

Winterstein LM, Kukovetz K, Rauh O, Turman DL, Braun C, Moroni A, Schroeder I, Thiel G. 2018. Reconstitution and functional characterization of ion channels from nanodiscs in lipid bilayers. J. Gen Physiol. 150, 637-646. DOI: 10.1085/jgp.201711904. Epub 2018 Feb 27, PMID: 29487088

Yang T, Liu Q, Kloss B, Bruni R, Kalathur RC, Guo Y, Kloppmann E, Rost B, Colecraft HM, Hendrickson WA. 2014. Structure and selectivity in bestrophin ion channels. Science 346:355–359. DOI: https://doi.org/10.1126/science.1259723, PMID: 25324390

Zhou Y, Morais-Cabral JH, Kaufman A, MacKinnon R. 2001. Chemistry of ion coordination and hydration revealed by a K+ channel-Fab complex at 2.0 A resolution. Nature 414:43–48. DOI: https://doi.org/10.1038/35102009, PMID: 11689936

Zhou Y, MacKinnon R. 2003. The occupancy of ions in the K+ selectivity filter: charge balance and coupling of ion binding to a protein conformational change underlie high conduction rates. Journal of Molecular Biology 333: 965–975. DOI: https://doi.org/10.1016/j.jmb.2003.09.022, PMID: 14583193

Zhou M, MacKinnon R. 2004. A mutant KcsA K(+) channel with altered conduction properties and selectivity filter ion distribution. Journal of Molecular Biology 338:839–846. DOI: https://doi.org/10.1016/j.jmb.2004.03.020,PMID: 15099749

3. Ep-Cov-2 – The Envelope Protein of SARS-CoV-2 corrupts homeostatic signaling mechanisms in mammalian cells

3.1 Abstract

Infections with coronaviruses (CoVs) have led in the last decades to SARS (SARS-CoV-1; 2003) and MERS (2012) epidemics and to the most recent COVID-19 (SARS-CoV-2; 2019) pandemic. CoVs in general are built from four major structural proteins: the nucleocapsid (N) protein engulfing the viral RNA, the spike (S) protein, the membrane (M) protein and the envelope (E) protein.

It is known that infected host cells produce during replication of SARS-CoV-2 large amounts of envelope protein (Ep-CoV-2), which are partially inserted into the membrane of nascent viral particles as well as into cellular membranes. To mimic the pathophysiological impact on human cells, Ep-CoV-2 was overexpressed in mammalian cells and the protein sorting as well as the effect on key signaling parameters was monitored. The GFP-tagged protein (Ep-CoV-2_{GFP}) was mostly present in the endoplasmic reticulum but in small amounts also in particular regions of the PM. Performing fluorescent measurements, I observed that Ep-CoV-2 corrupted some of the most important homeostatic mechanisms in both HEK293 and A549 cells. Expression of Ep-CoV-2 evoked an elevation of the intracellular Ca^{2+} concentration ($[Ca^{2+}]_{in}$) and pH (in HEK293 and A549) and induced membrane depolarization (only for HEK293).

Functional testing in HEK293 cells showed that the rise in $[Ca^{2+}]_{in}$ is reduced, but not eliminated, by expressing either the truncated Ep-CoV-2 protein (Ep-CoV-2_{TM}) or two mutants, which are supposed to affect channel function (N15A or V25F). A similar picture emerged from the pH recordings. In this case, neither Ep-CoV-2_{TM} nor the mutants have a strong impact on the amplitude of the pH excursion in cells which express Ep-CoV-2. The impact of the mutants on E_M were again examined by fluorescent measurements and by patch-clamp recordings in HEK293 cells. The general picture which emerges from both assays suggests that the mutant proteins either reduce (EP-CoV-2_N15A) or eliminate (EP-CoV-2_V25F + Ep-CoV-2_{TM}) the depolarizing effect of Ep-CoV-2. From the differential impact of the mutants on either $[Ca^{2+}]_{in}$ and pH_{in}, compared to their effects on membrane potential on the other side, it can further be concluded that the membrane depolarization in Ep-CoV-2 expressing cells is neither a secondary result of altered Ca^{2+} nor a result of pH conditions.

An Ep-CoV-2 evoked elevation of intracellular $[Ca^{2+}]$ and pH as well as the induced membrane depolarization has the potential of interfering with major signal transduction cascades in cells. These functions of Ep-CoV-2, which may eventually contribute to the pathogenesis of the viral protein, can be partially explained by an ion channel activity of the viral protein. Two independent assays, a functional reconstitution of Ep-CoV-2 protein in artificial membranes and a rescue of K^+ deficient yeast mutants confirm that Ep-CoV-2 generates a cation conducting channel with a low unitary conductance and a complex ion selectivity. All this suggests that inhibitors of this channel function can provide cell protection and virostatic effects.

3.2 Introduction

Infections with CoVs have led in the last decades to the severe acute respiratory syndrome (SARS)-CoV-1 (2003) and Middle East respiratory syndrome (MERS) (2012) epidemics and to the most recent COVID-19 (Coronavirus disease 2019) pandemic (2019). CoVs are positive-strand enveloped RNA viruses with many different hosts and strains. The alpha-coronavirus strains 229E and OC43 are associated with up to 30% of common cold cases showing mild symptoms in humans (Mesel-Lemoine et al., 2012), while in non-human strains, such as the bovine corona virus (beta-coronavirus) or the avian infectious bronchitis virus (IBV, gamma-coronavirus), infections have large impacts in agricultural settings (Sjaak de Wit et al., 2011).

CoVs are built from four major structural proteins: the nucleocapsid (N) protein engulfing the viral RNA, the spike (S) protein, the membrane (M) protein and the envelope (E) protein. The S-, M- and E-protein are membrane proteins embedded in a lipid bilayer surrounding the ribonucleoprotein complex in the virus particle (Figure 3.1; Schoeman and Fielding, 2019). Presently, academic and pharmaceutical efforts are mainly focused on the S-protein which is involved in the entry of the virus into the host cell (Hoffmann et al., 2020). The M- and E-proteins in contrast are less well studied (Schoeman and Fielding, 2019) but there is compelling evidence for a concerted role of both proteins in the formation of virus-like particles in the ER-Golgi intermediate compartment (ERGIC) as well as in the process of budding of the mature virus particles from the host cells (Hogue et al., 2008). A prominent functional role of the E-protein is further supported by *in vivo* studies, which show that its genetic depletion alone leads to a marked decrease of viral fitness leading to reduced disease (Nieto-Torres et al., 2014; To et al., 2017). These data together with the indirect evidence for a functional role of the E-protein in acute respiratory distress syndrome (Schoeman and Fielding, 2019) underscore the necessity for improving our understanding of the role of the E protein in host-virus interaction.

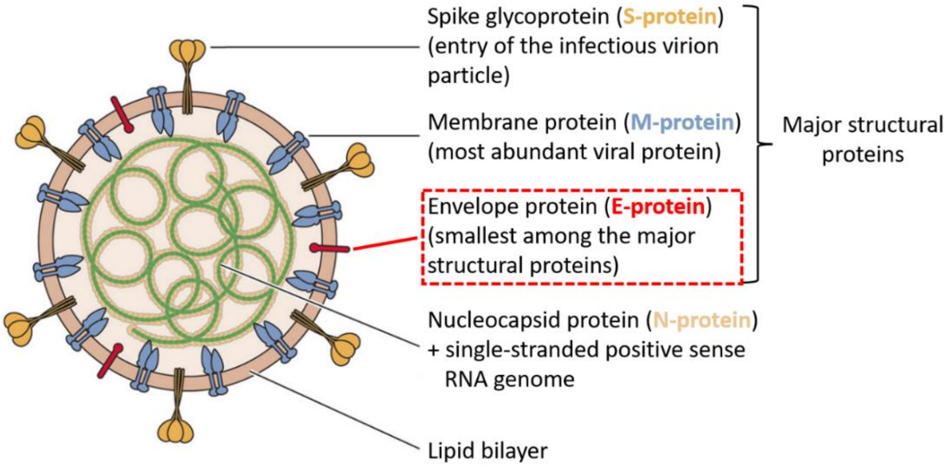

Figure 3.1: SARS-CoV-2 structure with major structural proteins. (modified from Dhama et al., 2020)

E-proteins are composed of three structural domains - a short hydrophilic N-terminus, a long transmembrane domain, and a long hydrophilic C-terminal domain with an alpha helical fold (Surya et al., 2018). Computer-based models and structural studies on purified proteins in detergent micelles suggest that the E-protein from both SARS-CoV-1 and SARS-CoV-2 forms a pentamer with a central pore that could serve as an ion channel (Liao et al., 2006; Mandala et al., 2020; Park et al., 2021; Surya et al., 2018).

For an understanding of the functional role of the E-protein in viral infection and replication, a detailed characterization of ion channel activity is essential. In the case of the E-protein from CoVs a number of electrophysiological studies have been performed using purified or synthetic E-proteins reconstituted in planar lipid bilayers (Nieto-Torres et al., 2015; Verdiá-Báguena et al., 2012; Verdiá-Báguena et al., 2013; Verdiá-Báguena et al., 2021; Wilson et al., 2004; Wilson et al., 2006; Xia et al., 2020). In addition, voltage clamp measurements were carried out in mammalian cells transiently transfected with the viral protein (Pervushin et al., 2009). The general consensus from all these studies is that the viral protein indeed exhibits channel activity. However, detailed scrutiny of the data provides a rather diverse picture on basic functional features of this channel, including unitary conductance and ion selectivity. While some studies report, after functional reconstitution of the protein in planar lipid bilayers, distinct channel fluctuations with a conductance in the lower pS range (10-20 pS) (Hutchison et al., 2021; Xia et al., 2020), others find a broad spectrum of conductance values including a unitary conductance in the range from 19 to >400 pS (Verdiá-Báguena et al., 2012; Wilson et al., 2004; Wilson et al., 2006). While all studies agree on an overall cation selectivity of the channel, there is no consensus on its preference for K^+ over Na^+ (McClenaghan et al., 2020) and whether it is at all permeable to Ca^{2+} (McClenaghan et al., 2020; Nieto-Torres et al., 2015). In some of these studies it was reported that E-protein-mediated channel fluctuations were inhibited by the antiviral channel blocker amantadine or hexamethylene-amiloride (HMA), and the presence of these compounds also resulted in an attenuation of virus replication *in vivo* (Fink et al., 2021; Park et al., 2021; Pervushin et al., 2009; Torres et al., 2007). Because of the heterogeneity in the functional data, it is currently difficult to interpret these pharmacological results in the context of a defined channel activity of the E-protein. Accordingly, it is also not surprising that a correlation between the sensitivity of the channel to HMA and its effect on plaque formation has been questioned (McClenaghan et al., 2020).

Furthermore, reports on whether the E-protein from SARS-CoV-1 (Ep-CoV-1) and SARS-CoV-2 (Ep-CoV-2) can form ion channels that reach the PM of cells are controversial. While some studies report an Ep-CoV-1-generated conductance in the PM of Xenopus oocytes and mammalian cells (Jeppesen et al., 2020; Pervushin et al., 2009), others do not find any evidence for elevated currents after expressing the protein in the same systems (Cabrera-Garcia et al., 2021; Mehregan et al., 2021). The latter work suggests that the presence or absence of the Ep-CoV-2 in the PM is a matter of protein sorting. Only after addition of an appropriate sorting signal trafficking of Ep-CoV-2 was reported to the PM of Xenopus oocytes and mammalian cells where it generated a cation-selective conductance (Cabrera-Garcia et al., 2021). At this point, it is difficult to explain this variability in observed channel function. One possible explanation is that this functional diversity reflects differences in the experimental conditions, including the systems under which the E-protein was isolated or synthesized and the approaches with which it was functionally reconstituted.

To further improve understanding of the functional properties of Ep-CoV-2, initially its channel function was confirmed. When the protein was synthesized *in vitro* into nanodiscs and reconstituted into model bilayer membranes, it generated a cation conductance with a defined low unitary amplitude and long open and closed times on the order of seconds. Heterologous expression of the protein and its mutants in mammalian cells caused major changes of cellular signaling parameters, specifically membrane depolarization, an elevation of free $[Ca^{2+}]_{in}$ and an intracellular alkalization. It is already well established that a number of viral membrane proteins exhibit channel activity with well-known roles in distinct steps of viral entry, replication and budding (Griffin et al., 2003; Nieva et al., 2012; Pinto and Lamb, 2007). Particularly interesting in this context is the ability of some of these channels to modulate the concentration of free Ca^{2+} in the cytosol of the host cells (Hyser and Estes, 2015). The latter is a crucial second messenger in mammalian cells which orchestrates a multitude of cellular functions. A modulation of these signaling cascades is a key event in the infection and replication strategy of many viruses (Hyser and Estes, 2015; Olivier, 1996; Zhou et al., 2009). Hence, like in the case of other viral membrane channel proteins, such as the M2 protein from Influenza A (Moorthy et al., 2014), the E-protein is a good target for the development of blockers that may act as virostatic drugs.

3.3 Results and discussion

3.3.1 The E-protein of SARS-CoV-2 forms functional ion channels in model membranes

Several studies have reported that the E-protein from SARS-CoV-1 forms an ion channel (Schoeman and Fielding, 2019). The high similarity in the primary amino acid sequence with the corresponding Ep-CoV-2 from SARS-CoV-2 (Figure 3.2A, B) suggests that the latter should also exhibit channel function, which has been recently confirmed (Hutchison et al., 2021; Xia et al., 2020).

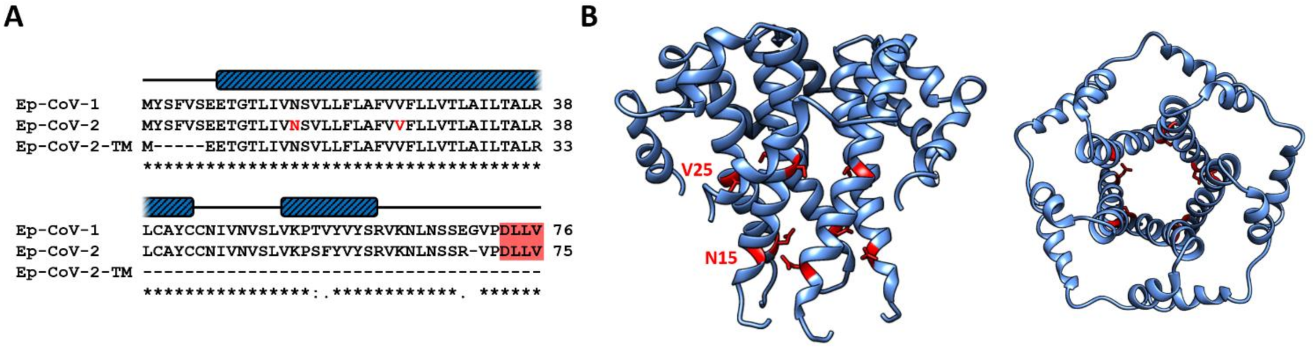

Figure 3.2: Ep-CoV-2 structure; (A) Alignment of the amino acid sequences of envelope proteins from SARS-CoV-1 (Ep-CoV-1), SARS-CoV-2 (Ep-CoV-2) and the truncated version of Ep-CoV-2 (Ep-CoV-2-TM) used in this study. Blue bars above sequences indicate regions with α-helical structure according to NMR analysis of full-length SARS-CoV-2. Asterisks denote conserved amino acids in Ep-CoV-1 and Ep-CoV-2; colons and dots indicate conservative and semi-conservative amino acid exchanges, respectively. Amino acids N15 and V25, which were mutated in this study, are colored red. The PDZ-binding motif D-L-L-V at the C-terminus of Ep-CoV-1 and Ep-CoV-2 is highlighted by a red box. **(B)** Cartoon representation of homology model of Ep-CoV-2 (amino acids 8 to 65). Left: side view of pentameric channel. Right: view from top to bottom. Positions of amino acids N15 and V25 highlighted in red. Homology model created with Swiss-Model using NMR structure of SARS Coronavirus E protein (PDB 5X29) as template.

To further test this prediction Ep-CoV-2 was synthesized *in vitro* into membrane-mimetic nanodiscs, a method with a low propensity of contaminations from the expression system (Winterstein et al., 2018). As biochemical evidence, the nanodiscs were shown to contain the FLAG-tagged Ep-CoV-2 (Ep-CoV-2_{FLAG}) after cell-free synthesis by performing SDS gels (Figure 3.3A). The protein maintains even in the SDS gel multimeric forms, a property that was also observed for other membrane proteins including Ep-CoV-2 (Mehregan et al., 2021). Notably this protocol was not designed to resolve the oligomeric state of functional Ep-CoV-2. Hence, the data only underpin that Ep-CoV-2 is synthesized into nanodiscs and that it has a spontaneous propensity for forming oligomers in the nano-membranes scaffolds.

After functional reconstitution of these Ep-CoV-2_{FLAG} proteins from the nanodiscs into a planar lipid bilayer (1:1 mixture of DPhPC:DPhPS), distinct channel fluctuations with characteristic seconds-long open and closed states and a low unitary amplitude became visible (Figure. 3.3B). Typically, this type of activity was observable 10-20 minutes after the nanodisc/protein complexes were added to the model membrane. For FLAG-tagged and untagged protein (Ep-CoV-2), in symmetrical solutions with 250 mM KCl, a dominant unitary conductance of 16.3 ± 0.3 pS and 18.0 ± 0.4 pS, respectively, was found (Figure 3.3C). Hence addition of the FLAG-tag at the amino terminus of the protein has no major effect on the channel conductance (Figure 3.3C). The i/V relation of the channel is linear over the range of test voltages between ±150 mV. The unitary conductance of Ep-CoV-2 increases with increasing salt concentration; a 10-fold elevation in KCl from 0.1 to 1 M increases the unitary channel conductance by a factor of 2.3 (Figure 3.4A). The open-channel conductance of Ep-CoV-2 is sensitive to the lipid bilayer composition. In a bilayer with a 1:1 mix of neutral (DPhPC) and anionic lipids (DPhPS) the unitary conductance increased 1.5-fold over that recorded in neutral bilayers (Figure 3.4B). A sensitivity of Ep-CoV-1 channel conductance to anionic phospholipids was already reported previously (Verdiá-Báguena et al., 2013).

Altogether the channel recordings show some similarities to published data in that the unitary conductance is in the range of 10 to 20 pS, values consistent with those that have been reported by others (Hutchison et al., 2021; Park et al., 2021; Wilson et al., 2004; Xia et al., 2020). Differing from some previous studies (Park et al., 2021; Wilson et al., 2004), however, the channel in these recordings has only one major conductance. Worth noting are the longer open and closed dwell times in the presented measurements compared to those reported by Hutchison et al., 2021. In both studies, the viral proteins were solubilized either into nanodiscs (the present study) or into amphipols (Hutchison et al., 2021) before functional reconstitution in bilayers. It is possible that this preparative step, which may preserve the native fold of the oligomeric protein, is the source of these differences in the functional properties of the channel.

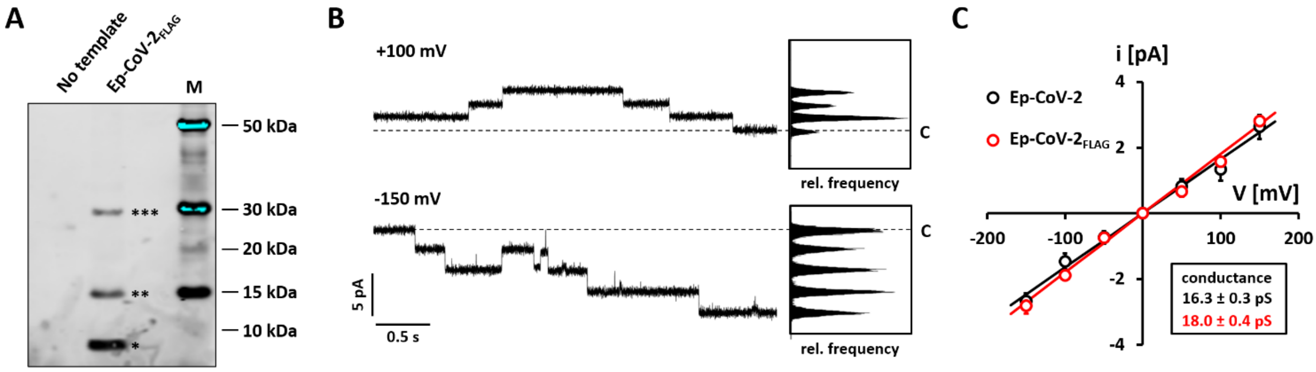

Figure 3.3: Ep-CoV-2 shows ion channel activity in artificial lipid bilayers. (A) Western-blot analysis of purified No template and Ep-CoV-2$_{\text{FLAG}}$ *in vitro* expression products using a mouse anti-FLAG tag antibody as described in material and methods. Number of asterisks indicates the oligomeric state of Ep-CoV-2$_{\text{FLAG}}$. **(B)** Exemplary current fluctuations generated by *in vitro* translated Ep-CoV-2 channels in 1:1 DPhPC/DPhPS lipid bilayer at +100 and -150 mV in symmetrical 250 mM KCl, 1 mM EGTA, and 10 mM HEPES (pH 7.4); corresponding amplitude histograms are depicted on the right. Dashed lines indicate the zero-current level. Current traces were digitally filtered at 100 Hz for visualization. **(C)** Unitary open-channel currents of Ep-CoV-2 and Ep-CoV-2$_{\text{FLAG}}$. Solid lines are best fits of $i = \gamma \cdot V$ to the two data sets, resulting in unitary conductance γ for Ep-CoV-2 (black) and Ep-CoV-2$_{\text{FLAG}}$ (red) given in box on bottom right. Data points in **C** are arithmetic means ± s.d. of >3 independent measurements.

Control experiments confirm that the channel activity measured here is indeed generated by Ep-CoV-2. In experiments in which *in vitro* expression was performed as in Figure 3.3B, C but without the vector or without the nanodiscs no channel activity was detected in the bilayer. As an additional control, the Ep-CoV-2_N15A mutant was synthesized into nanodiscs using the same methods employed for the wt-protein. This mutant, which is expected to corrupt channel function (Verdiá-Báguena et al., 2012), was able to generate some channel activity in the presented experiments. However, this occurred at a lower efficiency than with the wt-channel. While channel activity of the Ep-CoV-2_wt was robustly seen in typical single-channel recordings after 10-20 minutes, the N15A mutant, at comparable protein concentration, showed only activity after 240 minutes (three recordings in an accumulated experimental time of 12-14 h) (Figure 3.4C). The results of these experiments indicate that the N15A mutant is, in principle, active, but the mutant has either a reduced ability to form functional ion channels or the mutation compromises the pore stability and thus causes considerably reduced channel open probabilities.

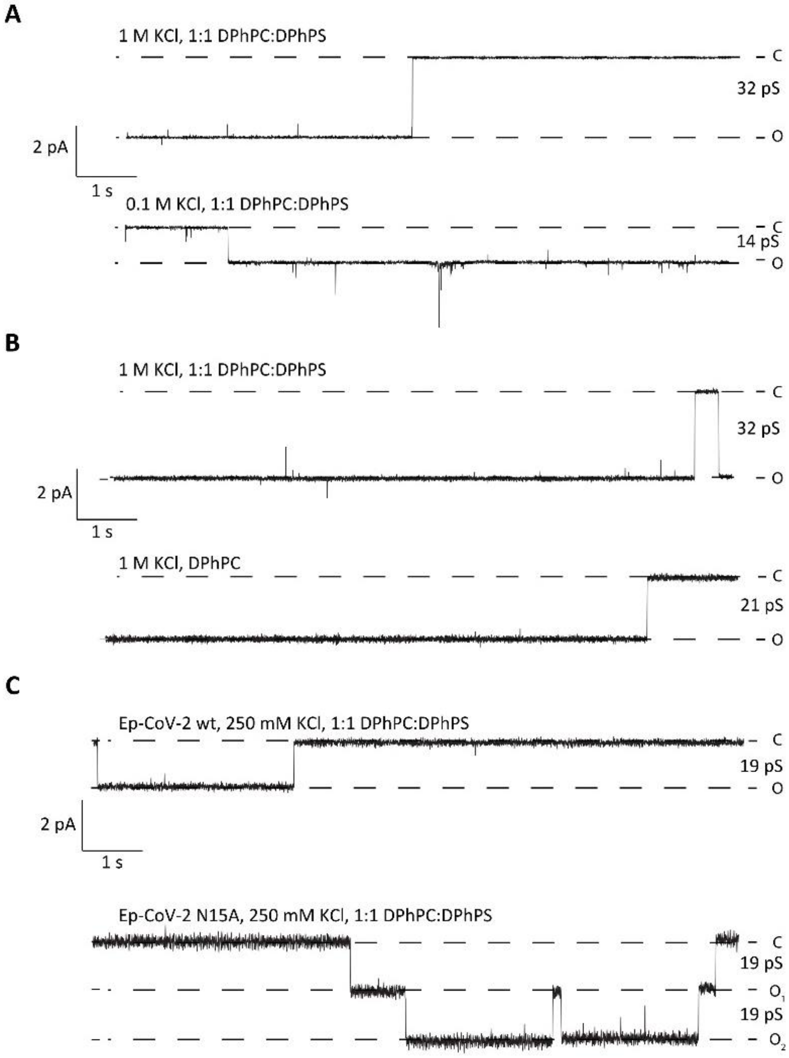

Figure 3.4. Channel recordings of mutant Ep-CoV-2_N15A and Ep-CoV-2_wt under different experimental conditions. (A) Effect of reducing KCl concentration in symmetrical recordings from 1 M (upper panel) to 0.1 M KCl

(lower panel) on unitary conductance of Ep-CoV-2. **(B)** Ep-CoV-2 generated channel fluctuations in symmetrical 1 M KCl solution in absence and presence of anionic lipids. Unitary conductance in bilayer with 1:1 mix of neutral (DPhPC (1,2-diphytanoyl-sn-glycero-3-phosphocholine) and anionic lipid (DPhPS) (1,2-diphytanoyl-sn-glycero-3-phospho-L-Serin) (upper panel) and recording in neutral DPhPC-only bilayers (lower panel). **(C)** Channel fluctuations in symmetrical 250 mM KCl with mixed DPhPC:DPhPS (1:1) bilayer generated by Ep-CoV-2_wt (upper panel) and Ep-CoV-2_N15A (lower panel). All recordings were done at -100 mV. Data was digitized at 100 kHz and digitally filtered for presentation at 100 Hz.

Channel function of Ep-CoV-2 was further confirmed by an independent yeast complementation assay (Anderson et al., 1992). A yeast mutant lacking the major K^+ uptake systems Trk1 and Trk2 (Bertl et al., 2003) grows in medium with high (107 mM) $[K^+]$, independent of whether the cells express the viral K^+ channel Kcv_{PBCV1} or Ep-CoV-2. This confirms that the latter protein is not cytotoxic for yeast growth. The data in Figure. 3.5A-C show that this mutant strain, however, is unable to grow in a medium with a low (7 mM) $[K^+]$. This growth defect can be rescued by expressing the small K^+ channel Kcv_{PBCV1} as a positive control (Gebhardt et al., 2011). A similar growth rescue was achieved by expressing Ep-CoV-2 (Figure 3.5A, C). These data are in agreement with the results from bilayer recordings in that Ep-CoV-2 forms a channel with a K^+ conductance. The finding that expression of Ep-CoV-2 is able to compensate for the absence of an endogenous K^+ uptake system is also in agreement with similar experiments in which the expression of the viral protein was modulating the growth of bacteria (Tomar and Arkin, 2020), both indicating that Ep-CoV-2 forms a channel with K^+ conductance. Further, the Ep-CoV-2 channel mutations V25F and N15A were tested in the yeast complementation system as well. Both mutants appeared unable to rescue the growth phenotype under potassium-limiting conditions (Figure 3.5C), which is in a general agreement with the aforementioned results from the suspended bilayer in that the N15A mutant is less active than the wt protein.

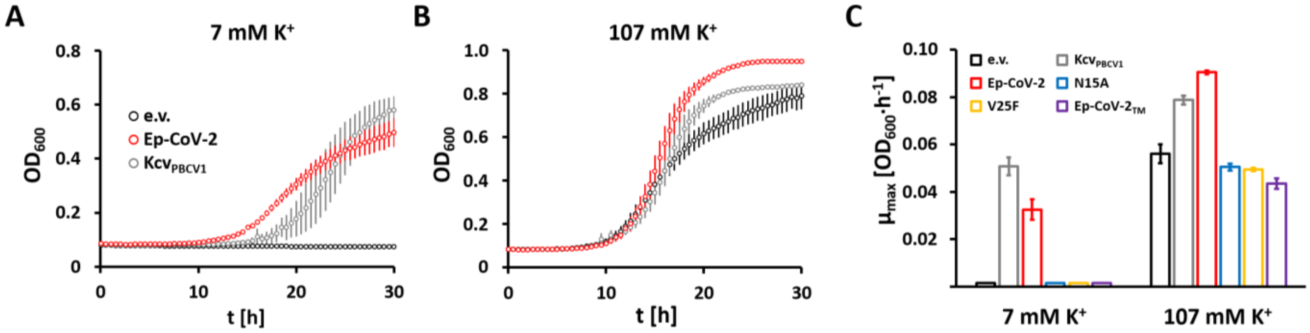

Figure 3.5: Ep-CoV-2 shows ion channel activity in yeast complementation assay. (A-C) Results of functional yeast complementation assay as described in material and methods using yeast strain PLY240 which is lacking K^+ uptake systems Trk1 and Trk2. Growth of PLY240 cells transformed with empty vector (e.v.), Ep-CoV-2 or Kcv_{PBCV1} was measured in low (7 mM) K^+ **(A)** and high (107 mM) K^+ **(B)**. **(C)** Maximal growth rates μ_{max} calculated from growth curves as in (A) and (B). Data points in **A-C** are arithmetic means ± s.d. of >3 independent measurements.

3.3.2 The E-protein affects cytoplasmic calcium

During replication the structural membrane proteins of coronaviruses are synthesized into the ER membrane of infected host cells (Ujike and Taguchi, 2015). Since Ep-CoV-2 has channel function in model membranes it is imaginable that cells expressing this protein might exhibit an altered membrane conductance of the ER. This could be crucial in virus infected cells, since the ER is a major reservoir of important cell signaling factors like Ca^{2+} and H^{+}.

In a first set of experiments, it was examined whether Ep-CoV-2 affects the intracellular concentration of $[Ca^{2+}]_{in}$. It is suggested that a heterologous expression of the viral Ep-CoV-2 mimics the high and uncontrolled expression of viral proteins in infected cells (Schoeman and Fielding, 2019). Therefore, HEK293 cells were co-transfected with cytosolic mRuby3 as a transfection marker with and without untagged Ep-CoV-2. Representative images of control cells stained with the Ca^{2+} sensor Fluo4-AM (Fluo4) show the same Fluo4 signal in mRuby3 positive and negative cells indicating that the transfection marker is not affecting $[Ca^{2+}]_{in}$ (Figure 3.6A, B). For cells co-transfected with Ep-CoV-2 and mRuby3, the Fluo4 signal is high in mRuby3-positive cells with respect to the mRuby3-negative controls (Figure 3.6A, B), but does not fully reach the values measured after adding the Ca^{2+}-ionophore ionomycin (Figure 3.6C). Given that the Fluo4 reporter has a K_d value of 345 nM $[Ca^{2+}]$ (Paredes et al., 2008) and is saturating at concentrations >1 µM, it is reasonable to assume that the presence of Ep-CoV-2 elevates $[Ca^{2+}]_{in}$ to a range of several hundred nM.

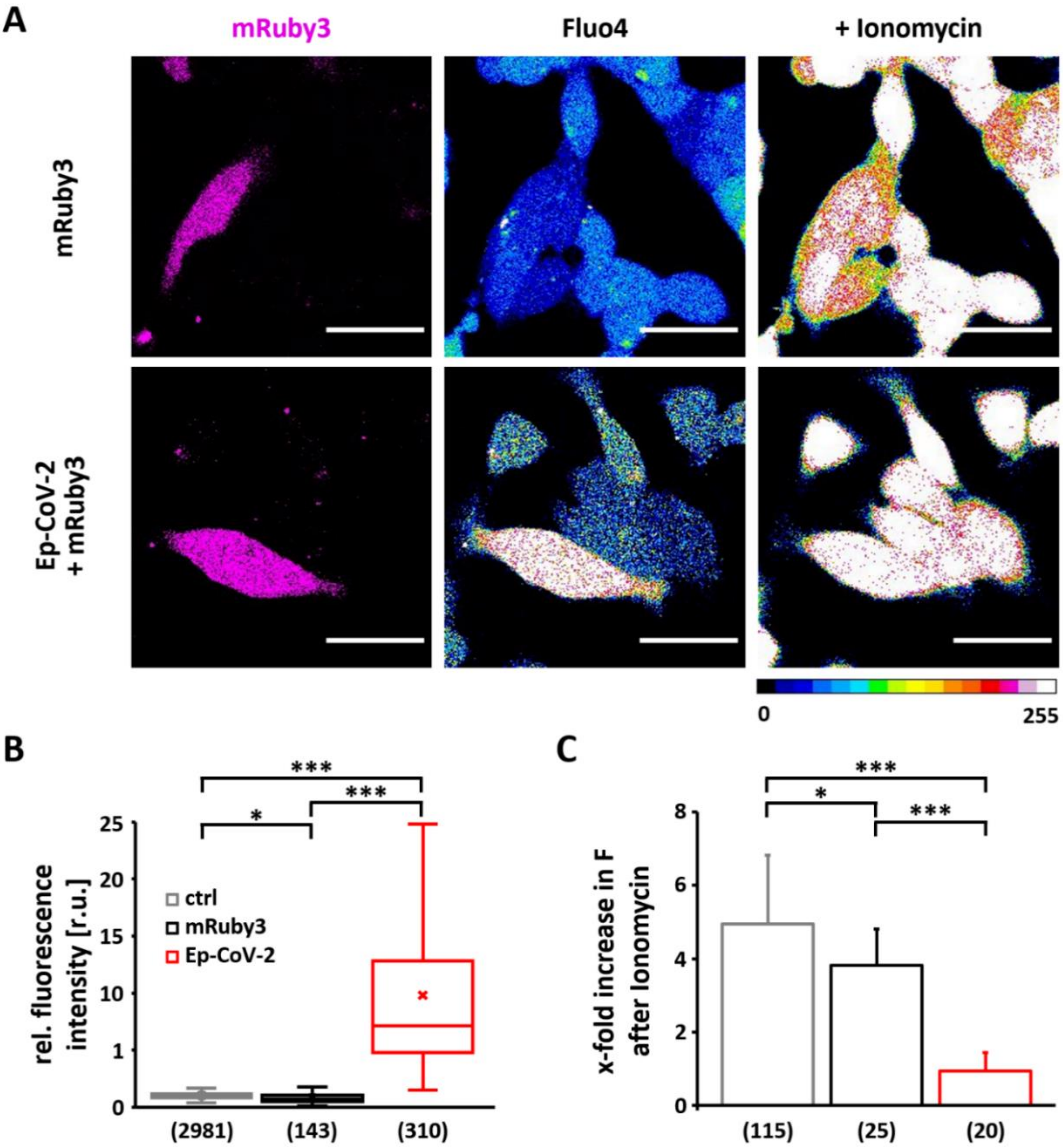

Figure 3.6: Expression of Ep-CoV-2 in HEK293 cells increases $[Ca^{2+}]_{in}$. (A) Representative fluorescence images of HEK293 cells transfected with either mRuby3 alone (negative control with mRuby3 reporting successful transfection, first lane) (upper row) or with mRuby3 + Ep-CoV-2 (lower row). The signal of $[Ca^{2+}]_{in}$ reporter Fluo4 is globally low in control cells irrespectively of presence/absence of mRuby3 but high in cells transfected with mRuby3 + Ep-CoV-2 (lane two and three (16 color LUT)). Addition of Ionomycin elevates $[Ca^{2+}]_{in}$ in all cells (lane three). Scale bar = 30 µm. **(B)** Boxplot of relative Fluo4 fluorescence intensity of HEK293 cells expressing mRuby3 alone (black) or Ep-CoV-2 + mRuby3 (red) normalized to mean intensity of untransfected cells (ctrl, grey). Number of measured cells in brackets. **(C)** X-fold increase in Fluo4 fluorescence intensity after addition of Ionomycin. Bars represent arithmetic mean ± s.d.; number of measured cells in brackets. Boxes of the box plots in (B) represent the 25th and 75th percentile; the median is shown as horizontal line, the arithmetic mean as cross. The bars indicate the minimal and maximal value. Statistical significance in (B) and (C) was determined with unpaired two-tailed student t-test assuming unequal variances ($p < 0.001$, ***; $0.001 < p < 0.01$, **; $0.01 < p < 0.05$, *; $p > 0.05$, n.s.).

Further, it was determined whether the increase in $[Ca^{2+}]_{in}$ is caused in an indirect manner by activation of endogenous PM Ca^{2+} channels. Experiments as in Figure 2 were therefore repeated in the presence of conventional calcium-channel blockers Gd^{3+} (10 µM) or Bepridil (20 µM). The presence of these blockers did not abolish the increased $[Ca^{2+}]_{in}$ in Ep-CoV-2 expressing cells (Figure 3.7C) implying that this rise in second messenger is not caused by an indirect activation of endogenous Ca^{2+} channels.

The conclusion that Ca^{2+} influx across the PM is not the origin for the elevated $[Ca^{2+}]_{in}$ was confirmed by Mn^{2+}-quenching experiments (Hallam and Rink, 1985). HEK293 cells transfected with Ep-CoV-2 were therefore loaded with Fura2-AM (Fura2) and transferred into a buffer containing 2 mM Mn^{2+}. This resulted in no apparent quenching of the Fura2 signal at 360 nm (Figure 3.7 A, B) indicating that Mn^{2+} (as substitute for Ca^{2+}) cannot enter the cells *via* the PM.

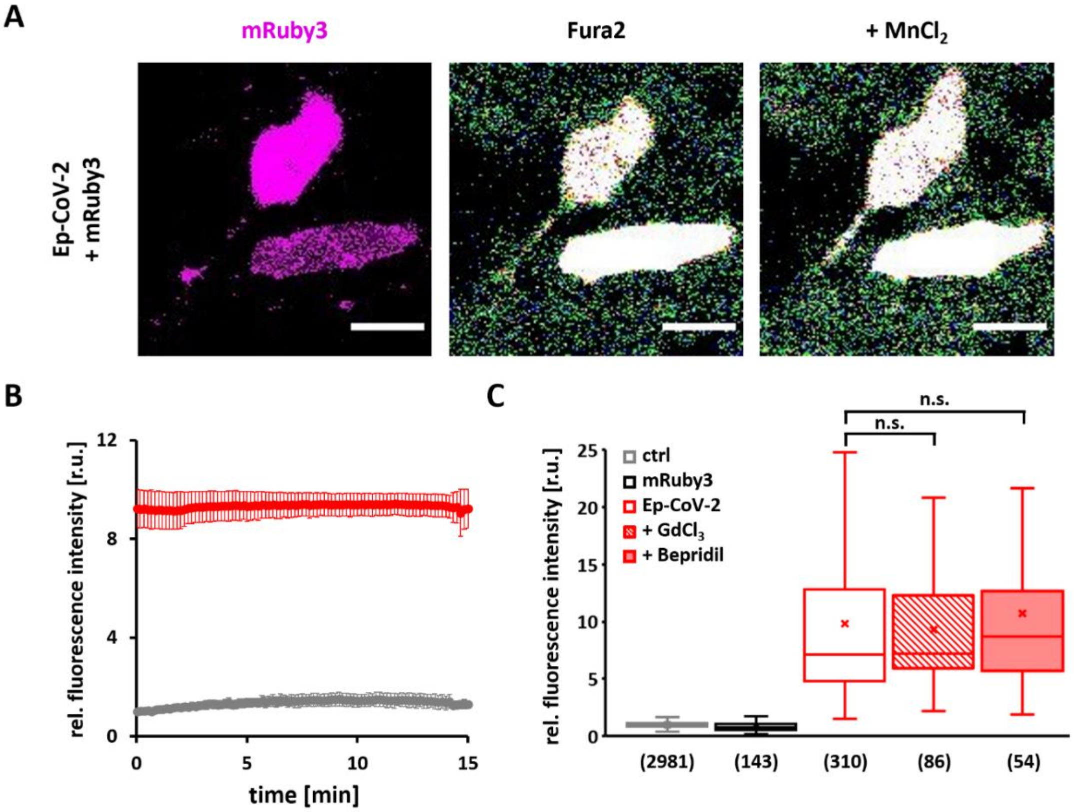

Figure 3.7: Addition of Mn^{2+} to external buffer does not quench elevated Fura2 signal in Ep-CoV-2 expressing HEK293 cells and conventional Ca^{2+} channel blockers do not abolish effects of Ep-CoV-2 on $[Ca^{2+}]_{in}$. **(A)** Representative fluorescence images of HEK293 cells expressing mRuby3 + Ep-CoV-2 with mRuby3 signal (left) and Fura2 signal in absence (central) and presence of 2 mM Mn^{2+} in buffer (right). Scale bars = 20 µm. **(B)** Dynamics of mean Fura2 fluorescence intensity in untransfected control cells (grey) and cells expressing mRuby3 + Ep-CoV-2 (red) after addition of 2 mM $MnCl_2$ to external buffer at time zero. Mean ± s.d. from > 8 cells were normalized to fluorescence intensity of control cells prior to addition of Mn^{2+}. **(C)** Relative fluorescent intensities from Ca^{2+} sensor Fluo4 in HEK293 cells expressing mRuby3 alone (black) or mRuby3 + Ep-CoV-2 in absence (red, open bar), or presence of 10 µM $GdCl_3$ (red, dashed bar) or 20 µM Bepridil (red, solid bar). Data obtained as in Figure 2B; data in absence of blockers are replotted from Figure 3.5. Number of measured cells in brackets. The boxes represent the 25th and 75th percentile; the median is shown as horizontal line, the arithmetic mean as cross. The bars indicate the minimal and maximal value. Statistical significance was determined with unpaired two-tailed student t-test assuming unequal variances ($p > 0.05$, n.s.).

To test if the effect of Ep-CoV-2 on $[Ca^{2+}]_{in}$ is a generic or cell-type-specific effect, experiments were also repeated in A549 cells, a model system for human alveolar cells which express the virus in infected humans (Wang et al., 2021). Ep-CoV-2 elicits also in these cells an increase in $[Ca^{2+}]_{in}$ (Figure 3.8 A, B) in these cells. Hence, expression of Ep-CoV-2 causes an elevated $[Ca^{2+}]_{in}$ in a cell-type-independent manner, which is not mediated by endogenous Ca^{2+} channels at the PM. The results of these experiments are in a general agreement with recent reports showing that expression of Ep-CoV-2 corrupts the Ca^{2+} homeostasis in mammalian cells and that this could be related to a release of the second messenger from internal stores (Mehregan et al., 2021). Such a scenario could well explain the elevated $[Ca^{2+}]_{in}$ in Ep-CoV-2 expressing cells observed in this study.

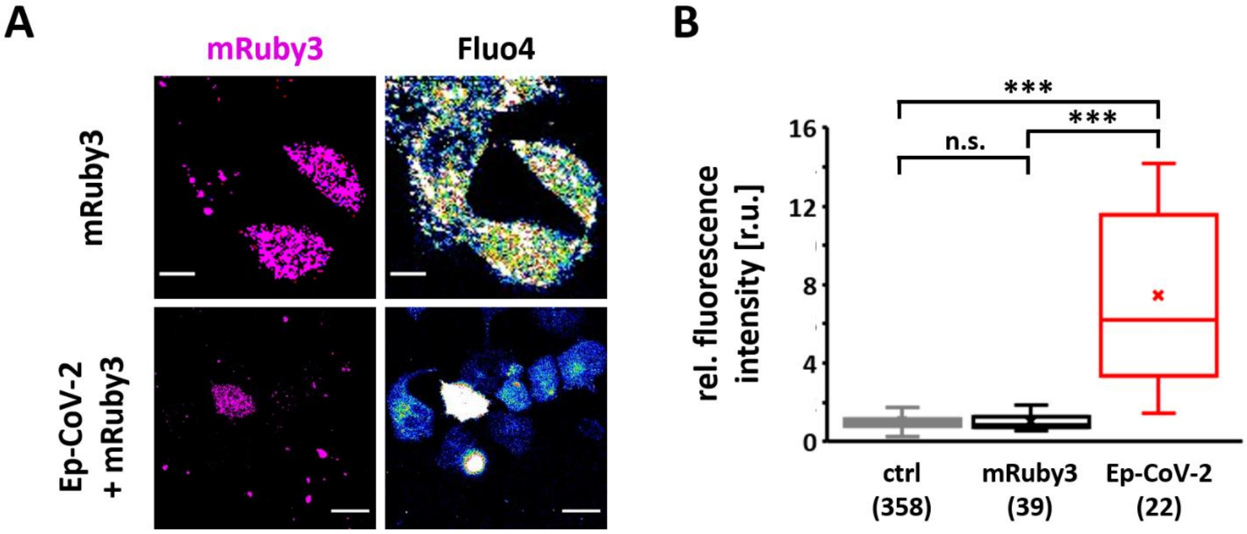

Figure 3.8: Expression of Ep-CoV-2 increases $[Ca^{2+}]_{in}$ of A549 cells. (A) Representative fluorescence images of A549 cells expressing either mRuby3 alone (negative control; upper row) or mRuby3 + Ep-CoV-2 (lower row). mRuby3 signal acts as a transfection control (first lane, magenta). Cells were loaded with 1 µM Fluo4-AM to indicate the $[Ca^{2+}]_{in}$ (second lane, 16 color LUT). Fluo4 intensity is insensitive to absence/presence of mRuby3 but elevated in cells co-transfected with mRuby3 + Ep-CoV-2. Scale bars represent a distance of 10 µm (upper row) and 20 µm (lower row). **(B)** Relative Fluo4 fluorescence intensity of HEK293 cells expressing mRuby3 alone (black) or Ep-CoV-2 + mRuby3 (red) normalized to mean intensity of untransfected cells (ctrl, grey); number of measured cells in brackets. Boxes represent the 25th and 75th percentile; the median is shown as horizontal line, the arithmetic mean as cross. The bars indicate the minimal and maximal value. Statistical significance in was determined with unpaired two-tailed student t-test assuming unequal variances ($p < 0.001$, ***; $p > 0.05$, n.s.).

3.3.3 E-protein in model membranes shows an anomalous mole fraction effect

To further test if this increase in $[Ca^{2+}]_{in}$ is directly mediated by the channel activity of Ep-CoV-2, the Ca^{2+} conductance in planar lipid bilayers was examined. Channel activity was first measured in a symmetrical 250 mM KCl solution before the buffer on the *trans*-side was exchanged with a K^+-free 125 mM $CaCl_2$ solution (Figure 3.9A left panel). In this condition positive and negative channel fluctuations occurred (Figure 3.9A, B). This suggests that the channel conducts K^+ outward and Ca^{2+} inward currents. When the solution on the *trans*-side, in the same recording, contained 125 mM $CaCl_2$ and 5 mM K^+, only K^+ outward current with no appreciable inward current was observed (Figure 3.9A, middle panel, Figure 3.9B). The results of these experiments suggest that the channels show an anomalous mole fraction effect (AMFE), a phenomenon that was already reported for a higher unitary conductance of Ep-CoV-2 (Verdiá-Báguena et al., 2021). The results of these experiments suggest that Ep-CoV-2 conducts Ca^{2+} and K^+ in pure solutions. A mixture of the two ions is not additive but they cause a mutual inhibition of unitary conductance. These data indicate that Ep-CoV-2 can, under specific constraints, conduct Ca^{2+}. However, it cannot be determined whether Ep-CoV-2 is solely responsible for the increase in $[Ca^{2+}]_{in}$ observed under physiological conditions. Instead, the presented data suggests an indirect effect of Ep-CoV-2 on the regulation of endogenous Ca^{2+} homeostasis.

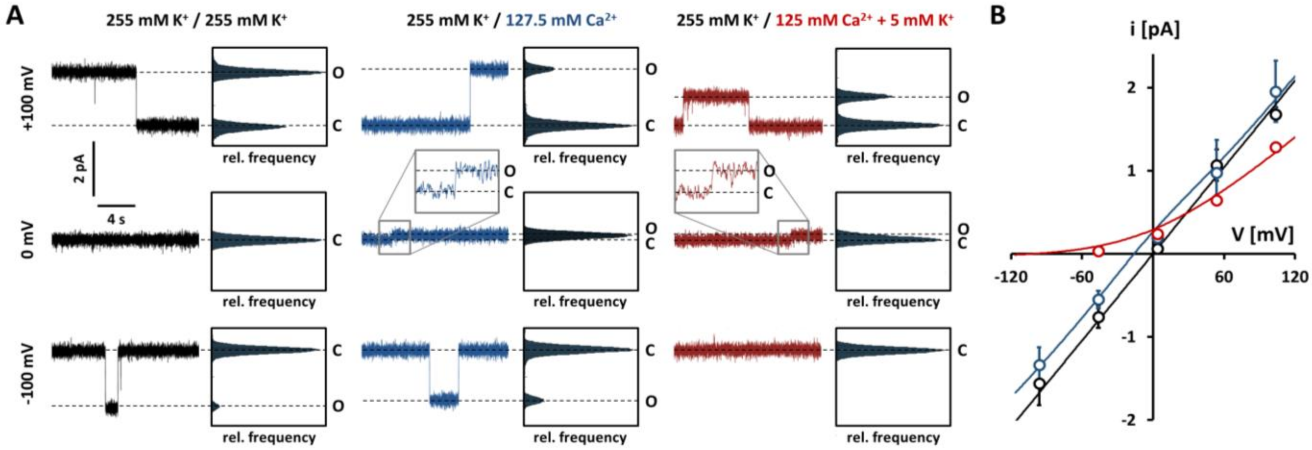

Figure 3.9: Ep-CoV-2 shows Ca^{2+} permeability and anomalous mole fraction effect in artificial lipid bilayers. (A) Representative Ep-CoV-2 single channel current fluctuations in 1:1 DPhPC/DPhPS lipid bilayer at +100 mV, 0 mV and -100 mV. The solution in the *cis* chamber always contained 255 mM K^+ (250 mM KCl, 1 mM EGTA, 10 mM HEPES, pH adjusted to 7.4 with ~5 mM KOH). The *trans* chamber was perfused with either 255 mM K^+ (same as in *cis*) (left, black), 127.5 mM Ca^{2+} (125 mM $CaCl_2$, 10 mM HEPES, pH adjusted to 7.4 with ~2.5 mM $Ca(OH)_2$)(middle, blue), or 127.5 mM Ca^{2+} + 5 mM K^+ (125 mM $CaCl_2$, 10 mM HEPES, pH adjusted to 7.4 with ~5 mM KOH)(right, red). Corresponding amplitude histograms are depicted on the right of each trace. Dashed lines indicate the closed (C) or open channel (O) level. Current jumps measured under asymmetric conditions at 0 mV are shown enlarged in gray boxes above the corresponding traces. Current traces were digitally filtered at 100 Hz for visualization. **(B)** Unitary open-channel currents of Ep-CoV-2 for the conditions shown in (A). Data points represent arithmetic mean ± s.d. of at least three independent measurements. Solid lines were inserted for visualization purposes only and have no physical meaning.

3.3.4 The E-protein has an impact on cellular pH homeostasis

To further determine the effect of Ep-CoV-2 on cellular ion homeostasis, identification of any possible effects on cellular pH (pH_{in}) was aspired; to this end experiments using the pH sensitive dye BCECF-AM were performed. Confocal images of control cells expressing only mRuby3 exhibit a homogeneous signal in all cells irrespectively of reporter expression (Figure 3.10A, upper row). In cells co-transfected with mRuby3 and Ep-CoV-2, a slight increase in the fluorescent signal throughout the cell was measured, suggesting that Ep-CoV-2 causes alkalization of the cytosol (Figure 3.10 A, lower row). To further test the significance of this effect the external buffer was exchanged from a neutral (pH 7.3) to an acidic (pH 4.5) medium. The consequent acidification of the cytosol resulted in mRuby3 negative cells in a slow decrease in the fluorescent signal. In contrast, mRuby3 positive cells, which were co-transfected with Ep-CoV-2, maintained a high fluorescent signal (Figure 3.10 A, B). The results of these experiments suggest that Ep-CoV-2 is not generating a proton conductance in the PM, but it is instead supporting cellular systems, which buffer the cytosolic pH close to its resting value. In both Ep-CoV-2 transfected and untransfected cells the intracellular pH decreased to a common level when the H^+ conductance of the PM was increased by nigericin; while this acidification was rapid in control cells it progressed much slower in Ep-CoV-2 positive cells (Figure 3.10C). Hence, the positive effect of Ep-CoV-2 on pH_{in} buffering can be overridden by a massive influx of H^+ across the PM.

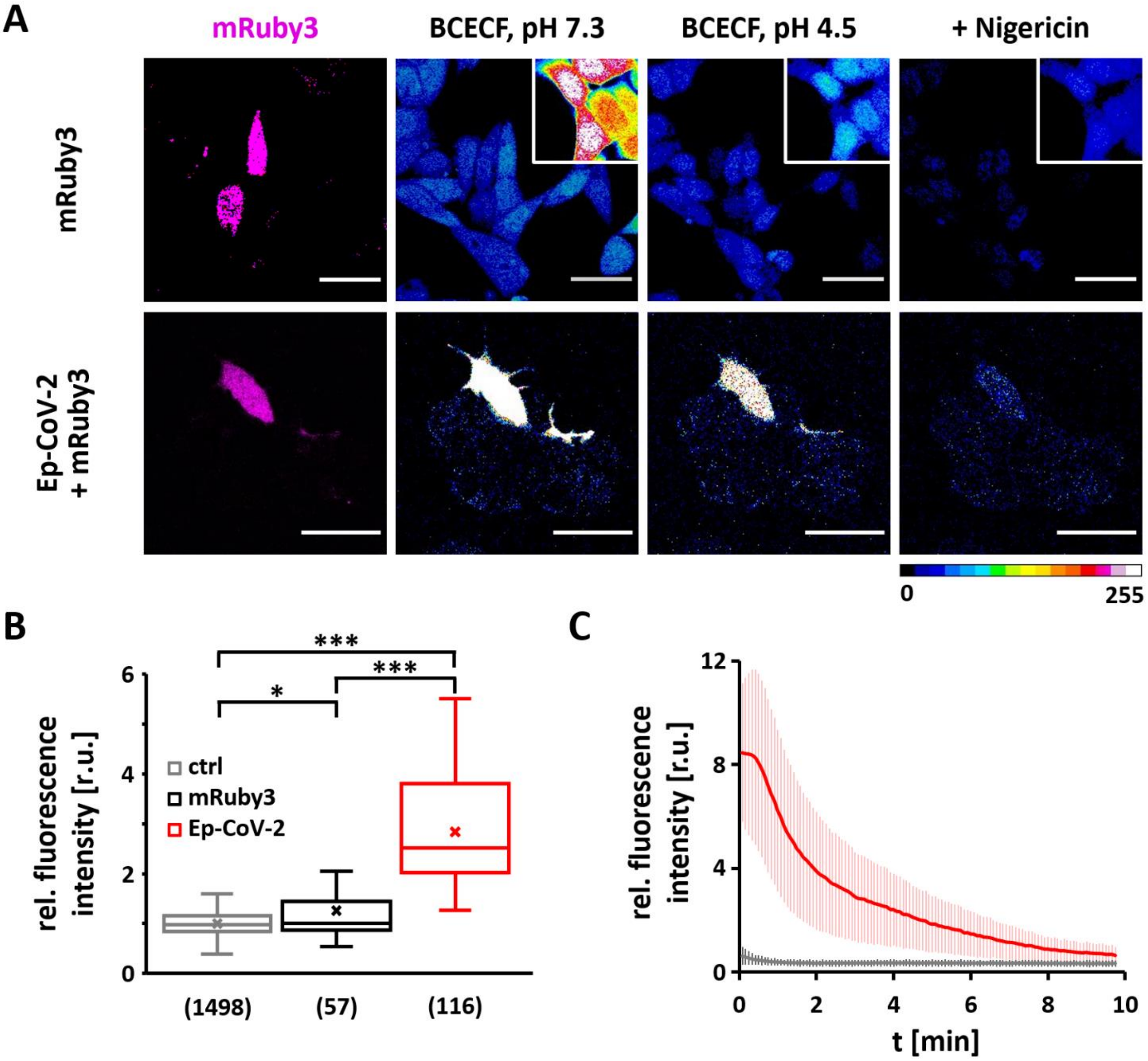

Figure 3.10: pH$_{in}$ remains high after acidification of external buffer only in Ep-CoV-2 expressing HEK293 cells. (A) Representative fluorescence images of HEK293 cells transfected with either mRuby3 alone (negative control with mRuby3 reporting successful transfection, first lane, magenta) (upper row) or with mRuby3 + Ep-CoV-2 (lower row). Fluorescence intensity of pH$_{in}$ reporter BCECF at extracellular pH of 7.3 (second lane, 16 color LUT) or 4.5 (third lane, 16 color LUT) and after addition of nigericin (forth lane, 16 color LUT). BCECF signal is independent of presence/absence of mRuby3 in control cells but elevated in cells expressing mRuby3 + Ep-CoV-2. While BCECF intensity decreases in control cells in acidic external buffer it remains high in cells expressing mRuby3 + Ep-CoV-2. Nigericin causes a decrease in BCECF signal in all cells. Area framed in controls is shown at higher intensity to appreciate decay of BCECF signal. Scale bar = 30 µm. **(B)** Boxplot of relative BCECF fluorescence intensity of HEK293 cells expressing mRuby3 alone (black) or Ep-CoV-2 + mRuby3 (red) normalized to mean intensity of untransfected cells (ctrl, grey); number of measured cells in brackets. Boxes represent the 25th and 75th percentile; the median is shown as horizontal line, the arithmetic mean as cross. The bars indicate the minimal and maximal value. Statistical significance was determined with unpaired two-tailed student t-test assuming unequal variances ($p < 0.001$, ***; $0.001 < p < 0.01$, **; $0.01 < p < 0.05$, *; $p > 0.05$, n.s.). **(C)** Time course of relative BCECF fluorescence intensity decay after addition of nigericin. Lines represent arithmetic means ± s.d. of 7 (Ep-CoV-2, red) and 12 (ctrl, grey) cells.

3.3.5 Ep-CoV-2 is located at the plasma membrane and affects the membrane potential

There are controversial reports on whether the E-protein from SARS-CoV-1 and SARS-CoV-2 can also form ion channels in the PM of cells. While some studies exclude an Ep-CoV-1 generated conductance in the PM (Cabrera-Garcia et al., 2021; Mehregan et al., 2021) others find elevated currents after expressing the protein in the same system (Jeppesen et al.2020; Pervushin et al., 2009). A recent publication suggests that the presence or absence of the Ep-CoV-2 in the PM is a matter of protein sorting. Only after addition of an appropriate sorting signal, Ep-CoV-2 was trafficking to the PM of *Xenopus* oocytes and mammalian cells, where it generated a cation selective conductance (Cabrera-Garcia et al., 2021).

Since the aforementioned yeast complementation assays suggested that Ep-CoV-2 is present in the PM (Figure 3.5), the next attempt was to visualize the protein in the PM of HEK293 cells. When GFP-tagged Ep-CoV-2 (Ep-CoV-2$_{GFP}$) was expressed in HEK293 cells, the fluorescence associated with the protein co-localized, like in other studies (Cabrera-Garcia et al., 2021; Mehregan et al., 2021), well with the fluorescent marker ER-Tracker^{TM} which stains specifically the endoplasmic reticulum (Figure 3.11 A, B).

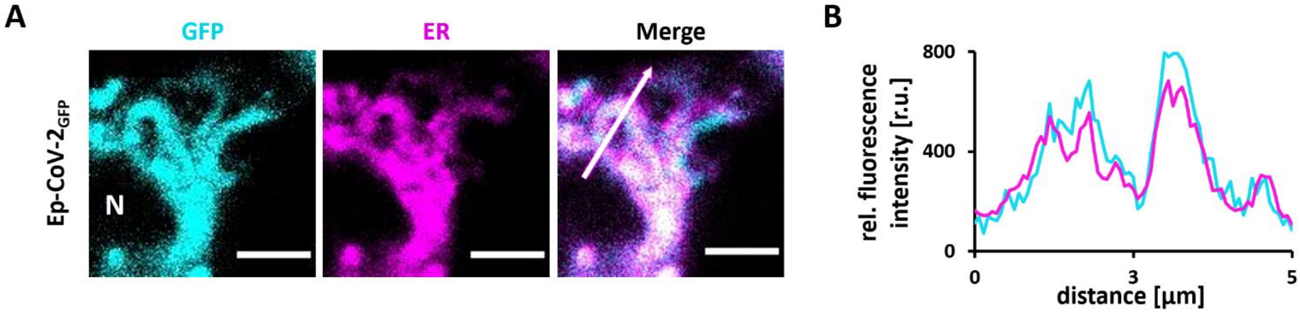

Figure 3.11: Ep-CoV-2 is sorted into the ER of HEK293 cells. (A) Representative fluorescence images with zoom on ER in periphery of nucleus (N) in HEK293 cells transfected with Ep-CoV-2$_{GFP}$. GFP signal (cyan, left lane) and ER-tracker^{TM} Blue-white DPX (magenta, middle lane) colocalize (right lane, merger). Scale bar = 3 µm. **(B)** Plot profile along inserted arrow from merger in **A**. Colocalization of Ep-CoV-2$_{GFP}$ (cyan) with ER signal (magenta).

To address the question of a PM localization for the Ep-CoV-2, high-resolution microscopy of membrane proteins in the PM was used (Axelrod, 1981). Small PM patches of HEK293 cells expressing Ep-CoV-2$_{GFP}$ were isolated by deroofing of the cell body (Biel et al., 2016) and imaged with TIRF microscopy. Figure 3.12A shows representative images of such PM patches transfected with either GFP alone or with Ep-CoV-2$_{GFP}$. The isolated PM patch in the evanescent field can be identified from the fluorescence of the PM-specific dye CellMask^{TM} Deep Red (CMDR, magenta). From the uneven intensity of this dye, it was concluded that the membrane patch is not making a flat foot over the entire contact with the cover slip. In some cases, like in the example in Figure

3.12A, small areas with a fluorescent signal from the ER-tracker^{TM} (yellow) are visible, suggesting some remaining cortical ER attached to the patches. In cells expressing only soluble GFP, no GFP fluorescence in the evanescent field of the isolated membrane patch or the associated ER was detected. Cells expressing Ep-CoV-2_{GFP}, on the other hand, frequently show a GFP signal in the plane of the PM; this signal is composed of intense spots and, in the case of remaining cortical ER, of a diffuse low-intensity background (Figure 3.12A, B). In the overlay, the diffuse low-background GFP signal colocalizes with the ER marker, suggesting that the protein is present in the cortical ER. The intense fluorescent GFP spots, on the other hand, colocalize exclusively with the PM marker (Figure 3.12A, B). These spots of colocalization are never in the foot area where the PM touches the cover slip but higher up in the evanescent field. At this point, it cannot be distinguished if these are specific domains of the membrane or vesicular structures (e.g. exosomes) which were secreted from the cell. The same patterns of fluorescent signal distributions were detected in six other cells expressing Ep-CoV-2_{GFP}. Typically, the GFP signals were slightly but significantly elevated above the background in areas, which revealed a signal from the ER (Figure 3.12A, B). In ER-free areas, the GFP signal showed a spot-like distribution with an intensity well above that associated with the ER (Figure 3.12A, B). The results of these experiments confirm that Ep-CoV-2_{GFP} is present in the ER and reaches distinct areas of the PM, where it occurs at high concentration in a patch-like manner.

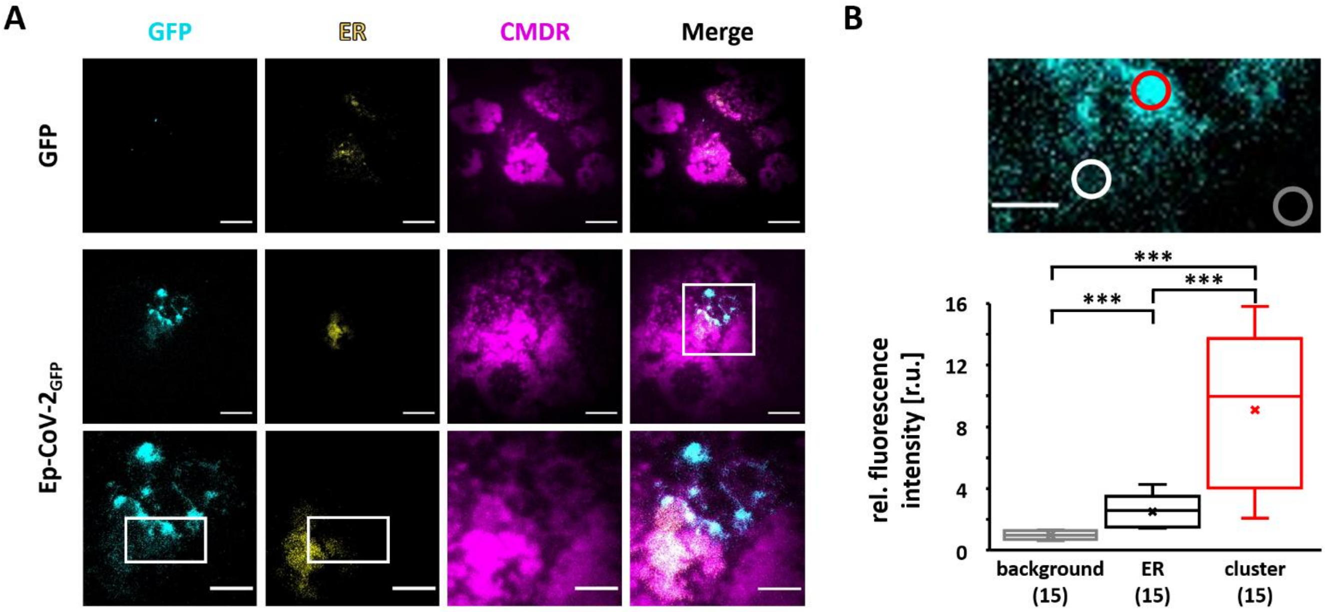

Figure 3.12: Ep-CoV-2 is sorted into distinct regions of the plasma membrane of HEK293 cells. (A) Exemplary fluorescence TIRF microscopy images of isolated membrane patches of HEK293 cells expressing either eGFP (upper row) or Ep-CoV-2_{GFP} (middle row). Area framed in merger is blown up in lower row. The GFP signal shows the localization of either eGFP or Ep-CoV-2_{GFP} in isolated membrane patches (first lane, cyan). Remaining ER on the isolated patches (second lane) and isolated PM patches (third lane) are identified by ER-tracker^{TM} Blue-white DPX (ER, yellow) and CellMask^{TM} Deep Red (CMDR, magenta) fluorescence, respectively. Mergers of lane 1, 2 and 3 show coincidence of Ep-CoV-2_{GFP}, ER and CMDR (fourth lane). Scale bars: 10 µm (upper and middle row) or 3 µm (lower row). **(B)** Magnified area marked in GFP and ER channels with regions of high and low GFP intensity (top). Regions of interest (ROI, circles) positioned over region with high GFP/low ER (red) and low GFP/high ER intensity (white) as well as background with no

GFP/ER fluorescence (grey). Relative fluorescence intensity of Ep-CoV-2_{GFP} in background (grey), ER regions (black/white) and vesicular like clusters (red) (bottom graph). Intensity was normalized to mean background intensity. The boxes represent the 25th and 75th percentile; the median is shown as horizontal line, the arithmetic mean as cross. The bars indicate the minimal and maximal value. Scale bar = 2 µm. Statistical significance was determined with unpaired two-tailed student t-test assuming unequal variances ($p < 0.001$, ***; $0.001 < p < 0.01$, **; $0.01 < p < 0.05$, *; $p > 0.05$, n.s.).

With the indication of a potential PM localization of Ep-CoV-2_{GFP}, its channel conductance by whole-cell patch-clamp measurements in HEK293 cells was tested. Comparative inspection of representative current responses with corresponding mean steady-state I/V relations from cells transfected with GFP or co-transfected with GFP and Ep-CoV-2 shows no obvious indication for a conductance of Ep-CoV-2 at the PM (Figure 3.13A). The same is true for cells transfected with Ep-CoV-2_{GFP}. The observed similarity in the I/V characteristics between control cells and cells expressing Ep-CoV-2 is present not only for measurements in physiological solutions containing K^+ and Na^+ but also in solutions with Cs^+ or high external Ca^{2+} (Figure 3.13B, C). Hence, in line with data from others (Mehregan et al., 2021), Ep-CoV-2 does not generate a measurable cation conductance in the PM of HEK293 cells. Either the protein is not present as a functional channel in the PM or the additional Ep-CoV-2 conductance is smaller than the scatter of current densities between individual cells.

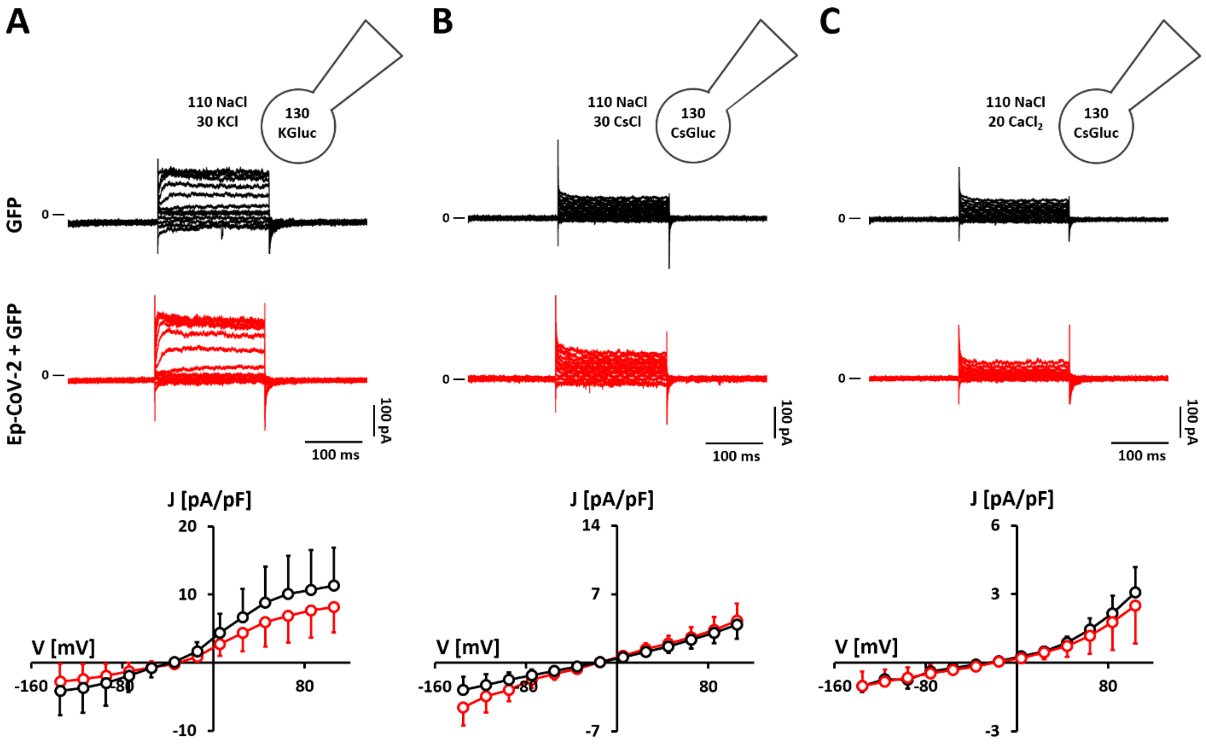

Figure 3.13: Expression of Ep-CoV-2 has no appreciable effect on whole-cell currents of HEK293 cells. (A-C) Whole-cell voltage-clamp recordings of HEK293 cells expressing GFP (negative control, upper row in black) or Ep-CoV-2 and GFP (middle row in red). Whole-cell currents elicited by voltage steps between -135 mV and +105 mV from holding potential of -95 mV. Current density (J) / voltage relations (V) (lower row) represent mean current densities at respective clamp voltages. Recordings were performed using standard internal and external solutions **(A)**, solutions containing cesium instead of potassium **(B)** and solutions containing cesium and high external $CaCl_2$ **(C)**. For more details see materials and methods.

While the data show no evidence for an Ep-CoV-2-mediated conductance at the PM, they do indicate that the viral protein causes a depolarization of the membrane potential in a K$^+$ containing solution. Close inspection of the I/V characteristic from cells expressing Ep-CoV-2 shows that the reversal voltage is depolarized and shifted by about 9 mV to a membrane potential more positive than the controls. In complementary experiments, resting membrane potentials (E$_M$) of cells ± Ep-CoV-2 were measured *via* current clamp recordings. The data in Figure 3.14C confirm that expression of Ep-CoV-2 causes a depolarization of the membrane potential (E$_M$) of 19 mV. This effect was only evident when Ep-CoV-2 was expressed without a GFP tag and in recordings with K$^+$ in the internal and external solutions. Substitution of K$^+$ with Cs$^+$ resulted in a strongly depolarized membrane potential in both Ep-CoV-2-transfected (E$_M$ = -0.7 ± 8.7 mV) and control cells (E$_M$ = +1.3 ± 8.2 mV) (Figure 3.14C). Further elevation of the external Ca^{2+} concentration from 2 to 20 mM did not result in a difference in E$_M$s between Ep-CoV-2-transfected (E$_M$ = +9.2 ± 13.8 mV) or control cells (E$_M$ = +13.4 ± 8.2 mV), providing additional evidence that the positive shift of the membrane potential in Ep-CoV-2-expressing cells is mediated by inhibition or elimination of an endogenous K$^+$ conductance or a K$^+$-dependent electrogenic transport process.

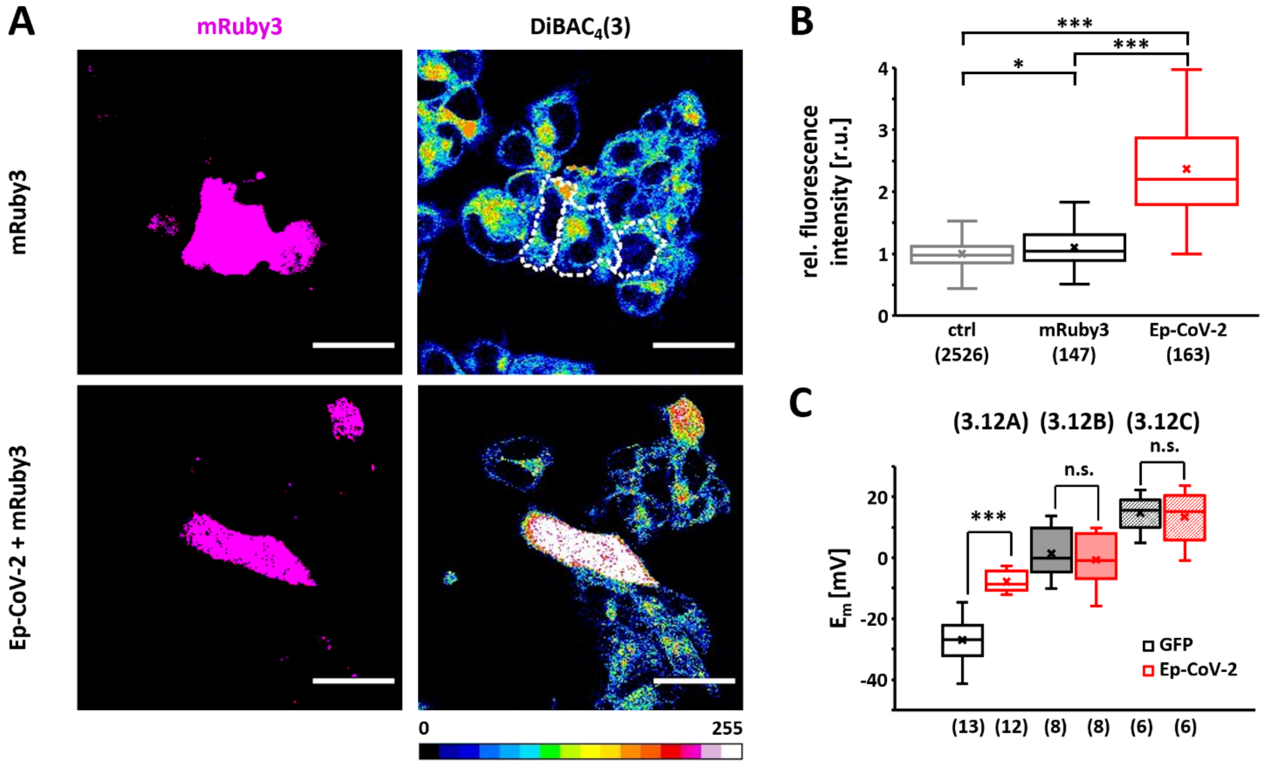

Figure 3.14: Expression of Ep-CoV-2 depolarizes the plasma membrane of HEK293 cells. (A) Representative fluorescence images of HEK293 cells expressing either mRuby3 alone as negative control (upper row) or Ep-CoV-2 + mRuby3 (lower row). mRuby3 signal acts as transfection control (first lane, magenta). Cells were loaded with 10 µM DiBAC$_4$(3) to monitor their membrane potential (lane two, 16 color LUT). Contours of mRuby3 positive cells in DiBAC$_4$(3) channel in upper row are highlighted with white dotted lines. Scale bar = 30 µm. **(B)** Relative DiBAC$_4$(3) fluorescence intensity of HEK293 cells expressing mRuby3 alone (black) or Ep-CoV-2 + mRuby3 (red) normalized to the mean intensity of untransfected cells (ctrl, grey); number of measured cells in brackets. **(C)** Mean membrane potentials (E$_M$) of HEK293 cells expressing GFP (black) or Ep-CoV-2 + GFP (red) measured by current-clamp in whole-cell

configuration in solutions (3.12A) - (3.12C) as in (Figure 3.12). Number of measured cells in brackets. The boxes of the box plots in (B) and (C) represent the 25th and 75th percentile; the median is shown as horizontal line, the arithmetic mean as cross. The bars indicate the minimal and maximal value. Statistical significance in (B) and (C) was determined with unpaired two-tailed student t-test assuming unequal variances ($p < 0.001$, ***; $p > 0.05$, n.s.).

The same measurements were repeated in A549 cells revealing a much larger variability of currents among control cells (Figure 3.15A, B). Typically, these cells exhibit different degrees of inward currents as well as outward currents with different types of kinetics. The latter are either dominated by an inactivating and/or non-inactivating outward rectifier. As much as the control cells show different types of currents, the membrane potentials of these cells are also more variable, including cells with strongly hyperpolarized and depolarized voltages (Figure 3.15C). The mean E_M from 24 different control cells was -13.6 ± 6.3 mV.

Electrophysiological recordings of cells expressing Ep-CoV-2 show the same heterogeneity of membrane currents as the controls (Figure 3.15A, B). The mean I/V characteristics of Ep-CoV-2-expressing cells match the heterogeneity of currents observed in the controls. In agreement with the results using HEK293 cells, this suggests that Ep-CoV-2 is not generating an appreciable ion conductance at the PM of A549 cells. The E_M of 25 Ep-CoV-2-expressing cells is -9.5 ±7.9 mV showing a non-significant ($p = 0.06$) depolarization compared to the control cells (Figure 3.15C).

The effect of Ep-CoV-2 on the membrane voltage of the two cell lines was confirmed by fluorescent measurements in cells with and without Ep-CoV-2. Quantitative image analysis shows that expression of mRuby3 alone has no impact on the fluorescence intensity of the voltage sensitive dye $DiBAC_4(3)$ in both cell types (Figure 3.14A, B; 3.15D, E). However, when HEK293 cells were co-transfected with mRuby3 and Ep-CoV-2, the mRuby3-positive cells exhibited a significant increase in $DiBAC_4(3)$ fluorescence (Figure 3.14A, B). This decrease in fluorescence indicates a depolarized membrane voltage.

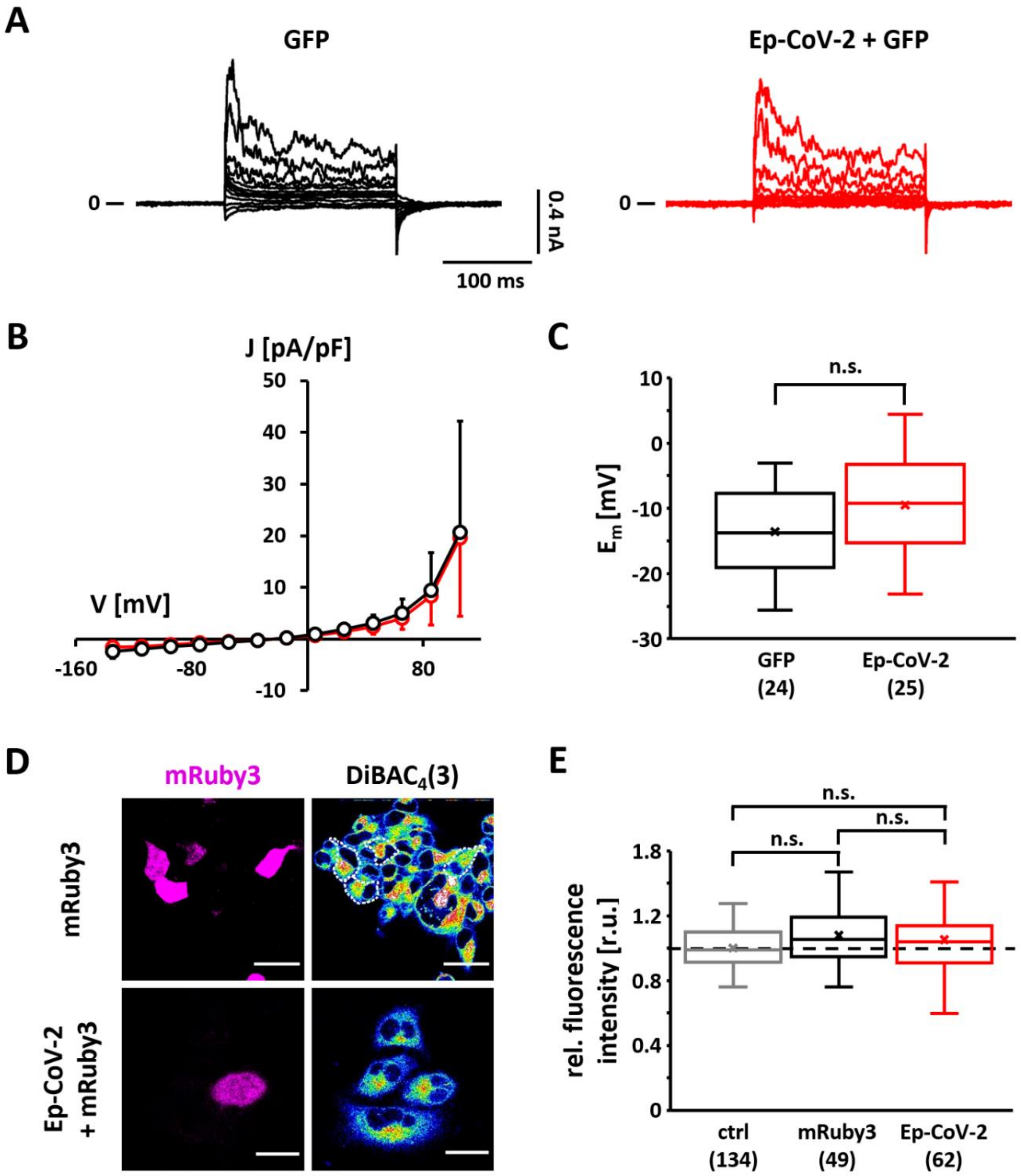

Figure 3.15: Expression of Ep-CoV-2 has no appreciable effect on electrical properties of the plasma membrane of A549 cells. (A) Representative whole-cell voltage-clamp recordings of A549 cells expressing GFP (black) or Ep-CoV-2 + GFP (red) using standard internal and external solutions. Currents were elicited by voltage steps between -135 mV and +105 mV from holding potential of -95 mV. **(B)** Corresponding mean current density/voltage relations at respective clamp voltages (GFP, black, n = 24; Ep-CoV-2+GFP, red, n = 25). **(C)** Mean membrane potentials (E_M) of A549 cells expressing GFP (black) or Ep-CoV-2 + GFP (red) measured by current-clamp in whole-cell configuration in standard solutions; number of measured cells in brackets. **(D)** Representative fluorescence images of A549 cells expressing either mRuby3 alone (negative control; upper row) or mRuby3 plus Ep-CoV-2 (lower row). mRuby3 signal acts as a transfection control (first lane, magenta). Cells were loaded with 10 µM DiBAC$_4$(3) to monitor their membrane potential (second lane, 16 color LUT). DiBAC$_4$(3) fluorescence is independent on presence/absence of mRuby3 or mRuby3 + Ep-CoV-2. Contours of mRuby3 positive cells in DiBAC$_4$(3) channel in upper row are highlighted with white dotted line. Scale bars represent a distance of 30 µm (upper row) and 20 µm (lower row). **(E)** Relative DiBAC$_4$(3) fluorescence intensity of A549 cells expressing mRuby3 alone (black) or Ep-CoV-2 + mRuby3 (red) normalized to mean intensity of untransfected cells (ctrl, grey); number of measured cells in brackets. Boxes of the box plots in (C) and (E) represent the 25th and 75th percentile; the median is shown as horizontal line, the arithmetic mean as cross. The bars indicate the minimal and maximal value. Statistical significance in (C) and (E) was determined with unpaired two-tailed student t-test assuming unequal variances ($p < 0.001$, ***; $p > 0.05$, n.s.).

We confirmed these findings using the fluorescent voltage reporter FluoVolt. The results (Figure 3.16A, B) are overall in good agreement with the electrical recordings, showing a depolarized E_M in Ep-CoV-2-expressing cells. In contrast, A549 cells show no appreciable difference in DiBAC$_4$(3) fluorescence between cells with or without Ep-CoV-2, which is also in agreement with the electrophysiological recordings.

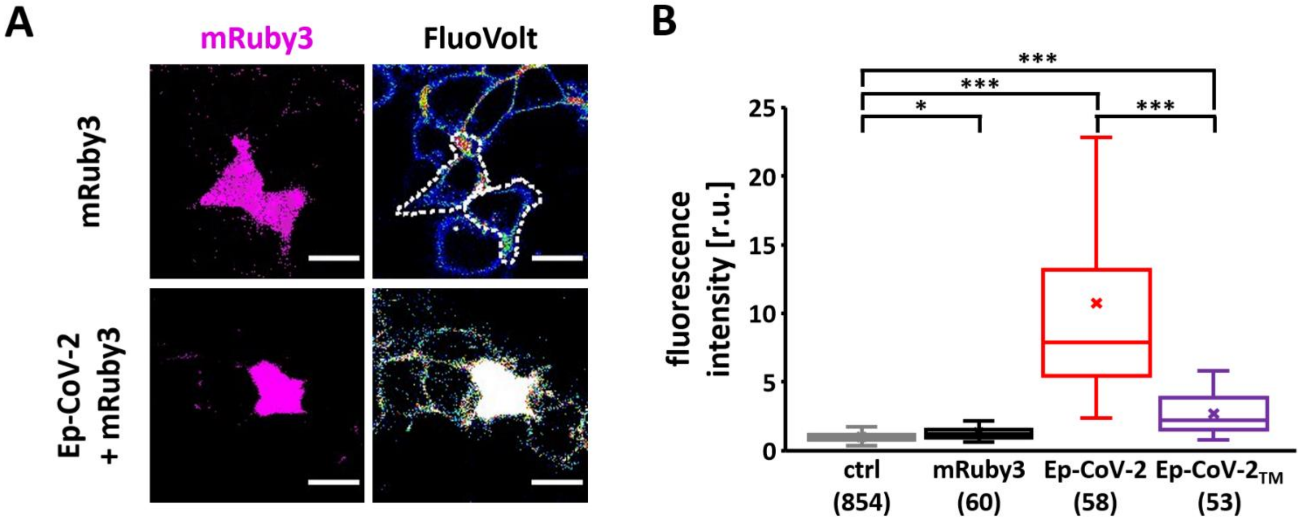

Figure 3.16: Expression of Ep-CoV-2 depolarizes plasma membrane. (A) Representative fluorescence images of HEK293 cells expressing either mRuby3 alone (negative control; upper row) or mRuby3 + Ep-CoV-2 (lower row). mRuby3 signal acts as a transfection control (first lane, magenta). Cells were loaded with voltage sensitive dye FluoVolt (second lane, 16 color LUT). Contours of mRuby3 positive cells in FluoVolt channel in upper row are highlighted with white dotted line. Scale bars represent a distance of 20 µm. **(B)** Relative fluorescence intensity of FluoVolt in untransfected control HEK293 cells (ctrl, grey) and HEK293 cells expressing mRuby3 alone (black), mRuby3 + Ep-CoV-2 (red) and mRuby3 + Ep-CoV-2$_{TM}$ (violet). Data are normalized to mean fluorescence intensity of untransfected control cells; number of measured cells in brackets. The boxes represent the 25th and 75th percentile; the median is shown as horizontal line, the arithmetic mean as cross. The bars indicate the minimal and maximal value. Statistical significance in was determined with unpaired two-tailed student t-test assuming unequal variances ($p < 0.001$, ***; $0.001 < p < 0.01$, **; $0.01 < p < 0.05$, *; $p > 0.05$, n.s.).

Taken together the data provide evidence that Ep-CoV-2 affects the membrane potential of mammalian cells in a cell-type-specific manner. No significant change of membrane currents above the measurement/noise level in Ep-CoV-2-expressing cells that would explain this shift of the membrane potential could be detected. These data indicate that only a small number of channels is reaching the PM where they generate a conductance that is in the range of the variability of current densities between individual cells. This interpretation would be consistent with the very low unitary conductance seen in bilayer recordings (Figure 3.3B, C) and the need of a targeting signal for efficient trafficking of Ep-CoV-2 to the PM (Cabrera-Garcia et al., 2021). The explanation would also agree with the finding that expression of Ep-CoV-2 in yeast is sufficient for rescuing yeast growth (Figure 3.5A-C). An alternative interpretation, which cannot be excluded at this point, is that the viral protein has no direct channel activity in the PM but modulates a transporter, which is strongly contributing to the membrane voltage in HEK293 but not in A549 cells. While this interpretation is compatible with the data in mammalian cells, it is not in agreement with the finding that Ep-CoV-2 is able to rescue K^+ uptake deficient yeast.

3.3.6 Mutants alter the impact of Ep-CoV-2 on cellular parameters

After finding that the expression of Ep-CoV-2 in HEK293 cells modulates $[Ca^{2+}]_{in}$, pH_{in} and E_M, three distinct cellular functions which are all related to cellular signaling cascades, the question arose whether these parameters are correlated and whether they are directly or indirectly related to a channel function of the viral protein. To answer this question, the $[Ca^{2+}]_{in}$, pH_{in} and E_M measurements were repeated with mutant constructs of Ep-CoV-2. Based on functional considerations deducted from homology modeling and from previously reported experimental studies, it was assumed that a C- and N-terminal truncation of (Ep-CoV-2_{TM}) (Figure 3.2A) should eliminate interactions with endogenous proteins (Corse and Machamer, 2003) while not compromising channel function (Verdiá-Báguena et al., 2012). According to data from Ep-CoV-1, point mutations N15A and V25F in the transmembrane domain of Ep-CoV-2 should eliminate or impair channel function (Torres et al., 2007; Verdiá-Báguena et al., 2012) by corrupting oligomerization of Ep-CoV-2 (Schoeman and Fielding, 2019). A recent study on full-length Ep-CoV-2, however, reports that both of these mutations affect the structure of the protein to differing extents but not its ability to oligomerize (Park et al., 2021). In order to access the impact of these mutations on channel function, the aforementioned yeast complementation assay was repeated with the respective Ep-CoV-2 mutants. The data show that none of the mutants was able to rescue yeast growth (Figure 3.5A-C). This implies that all the mutations including the truncation of cytosolic/extracellular domains, must have a strong impact on channel function at least in the yeast system.

Functional testing of these mutants in HEK293 cells shows that the rise in $[Ca^{2+}]_{in}$ is reduced, but not eliminated, by expressing either the truncated Ep-CoV-2 protein or the two mutants (Figure 3.17A). It is worth noting that the Ep-CoV-2_V25F mutant, which should have the most severe impact on ion channel function (Schoeman and Fielding, 2019), does not behave differently than the Ep-CoV-2_N15A mutant and the C- and N-terminal-truncated Ep-CoV-2_{TM}. A similar picture emerges from the pH recordings; here, neither the truncated protein nor the mutants have a strong impact on the amplitude of the pH excursion in cells which express Ep-CoV-2 (Figure 3.17B). Collectively the data show that mutations, which are thought to alter the structural properties of Ep-CoV-2, have an impact on its effect on cellular functions, which is not correlated with their impact on protein oligomerization and channel function (Schoeman and Fielding, 2019). This implies that the rise in $[Ca^{2+}]_{in}$ and pH either is not caused primarily by a channel function of Ep-CoV-2 or that the impact of the mutations from *in vitro* experiments cannot be directly extrapolated to functional data in cells. It is possible that mutations N15A and V25F impair (but do not eliminate) oligomerization and, consequently, channel function. The latter interpretation is in agreement with the findings that the N15A mutant was still able to generate some channel functions in artificial membranes (Figure 3.4C) and that both mutants exhibit the same oligomerization as the full-length Ep-CoV-2 wt protein (Park et al., 2021).

The impact of the mutants on E_M were again examined by fluorescent measurements and by patch-clamp recordings in HEK293 cells. The general picture which emerges from both assays suggests that the mutant proteins either reduce (EP-CoV-2_N15A) or eliminate (EP-CoV-2_V25F and Ep-CoV-2_{TM}) the depolarizing effect of Ep-CoV-2 (Figure 3.17C, D). The mutants affecting the oligomerization of the protein (EP-CoV-2_V25F) or its interaction with other protein partners (Ep-CoV-2_{TM}) fully eliminate the depolarizing effect of Ep-CoV-2 on the membrane voltage (Figure 3.17C, D). Again, the effects of the mutations on membrane depolarization are not in line with their expected impact on channel function, meaning that either biochemical data cannot be extrapolated in channel function or that the depolarization is not the result of a channel function. The data would also support a scenario in which Ep-CoV-2 interacts with either a pump or a channel; the resulting modulation of the latter is then causing the membrane depolarization. It is worth noting that such a scenario could also explain the negative effect of the GFP tag on Ep-CoV-2-induced membrane depolarization because it could sterically hinder the proposed interaction with other proteins.

From the differential impact of the mutants on either $[Ca^{2+}]_{in}$ and pH_{in}, compared to their effects on membrane potential on the other side (Figure 3.17A-D), it can further be concluded that the membrane depolarization in Ep-CoV-2 expressing cells is neither a secondary result of altered Ca^{2+} nor a result of pH conditions. The apparent requirement of this effect on the cytosolic terminus (Figure 3.17C, D) instead suggests that interactions of this domain with cellular factors are essential for this effect. Such interactions could also be disturbed in a case where the oligomerization of the protein is corrupted. It is possible that in this case the extracellular/cytosolic termini are misfolded preventing an interaction with partner proteins.

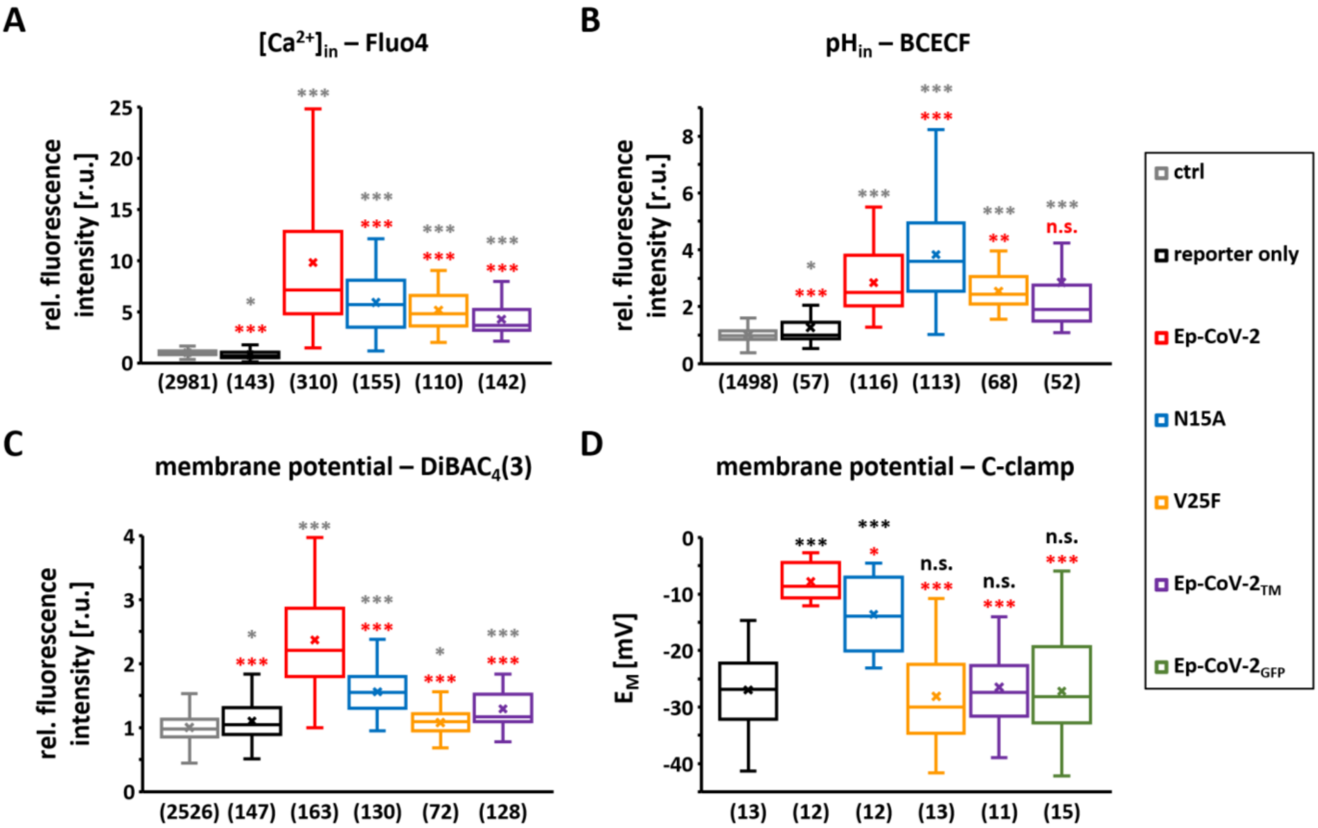

Figure 3.17: Effects of Ep-CoV-2 and its mutants on $[Ca^{2+}]_{in}$, pH_{in} and membrane potential. **(A-C)** Box plot of relative fluorescent intensities from sensors for Ca^{2+} (Fluo4, **(A)**), pH (BCECF, **(B)**) membrane voltage ($DiBAC_4(3)$ **(C)**) in HEK293 cells expressing mRuby3 alone (black) or mRuby3 + Ep-CoV-2 variants (red (wt), blue (N15A), yellow (V25F) and purple ($Ep\text{-}CoV\text{-}2_{TM}$)). Data normalized to mean intensity of untransfected HEK293 cells (ctrl, grey); number of measured cells in brackets. **(D)** Mean membrane potentials (E_M) of HEK293 cells expressing eGFP (black) and eGFP + Ep-CoV-2 variants: Red (wt), blue (N15A), yellow (V25F) and purple ($Ep\text{-}CoV\text{-}2_{TM}$) or green $Ep\text{-}CoV\text{-}2_{GFP}$. E_Ms were measured by current-clamp in whole-cell configuration; number of measured cells in brackets. The boxes of the box plots in A-D represent the 25th and 75th percentile; the median is shown as horizontal line, the arithmetic mean as cross. The bars indicate the minimal and maximal value. Statistical significance was determined with unpaired two-tailed student t-test assuming unequal variances ($p < 0.001$, ***; $0.001 < p < 0.01$, **; $0.01 < p < 0.05$, *; $p > 0.05$, n.s.).

3.4 Conclusion and outlook

Host cells infected with CoVs produce abundant amounts of Ep-CoV-2, of which only a small part is incorporated into the nascent virus particle as structural membrane proteins; the majority of the proteins remain in host cell membranes. The data presented here shed light on the potential impacts of the latter protein fraction on functional properties of infected cells. A key concept of cell-signaling is that crucial signaling cascades, which modulate a large spectrum of functions ranging from acute reactions to long lasting alteration in cell development and differentiation. This concept has been extensively studied for Ca^{2+} and pH (Berridge et al., 2003; Putnam, 2012). This study reports that expression of Ep-CoV-2 affects three of the main homeostatic control systems of mammalian cells - the PM voltage, $[Ca^{2+}]_{in}$ and pH_{in}. In this way, CoVs follow a strategy that is used by many viruses in that they commandeer universal signaling pathways in host cells to their own benefits. The three signaling parameters, which are modulated by Ep-CoV-2, are so universal in cells that any of the pathophysiological reactions in infected cells and tissues can potentially be associated with signaling cascades, which are triggered in response to Ep-CoV-2 activity. The present data on an Ep-CoV-2-mediated increase in $[Ca^{2+}]_{in}$ are interesting in the context of a recent report on the Porcine delta-coronavirus (PDCoV). It was found that this virus, which is related to SARS-CoV-1 and SARS-CoV-2, causes an increase in $[Ca^{2+}]_{in}$ in host cells (Bai et al., 2019). Further experiments revealed that pharmacological manipulations, which reduced the rise in $[Ca^{2+}]_{in}$, were able to inhibit distinct steps of PDCoV replication. In the context of these findings, it is tempting to speculate that the mortality-reducing effects of Ca^{2+}-channel blockers (Crespi and Alcock, 2020; Zhang et al., 2020) and Ca^{2+} chelators (Cashman, 2020) on the course of Covid-19 infections could be directly or indirectly related to the function of Ep-CoV-2 in elevating $[Ca^{2+}]_{in}$.

Using different experimental approaches, the presented data confirm reports by others in that Ep-CoV-2 has channel activity. Still the data provide no clear-cut answer to the question on whether this channel function is instrumental for the effects of Ep-CoV-2 on cell signaling cascades. Because of the complex interplay between K^+ and Ca^{2+} on channel permeability, it cannot be easily predicted from *in vitro* measurements whether the Ep-CoV-2 generated channel also conducts Ca^{2+} in the ER membrane under physiological conditions. Because of the high concentration gradient between the ER lumen and the cytosol, a small and steady Ca^{2+} leak in the ER membrane *via* an Ep-CoV-2 generated channel, however, might already be sufficient to cause the observed increase of $[Ca^{2+}]_{in}$. Also, the experiments with Ep-CoV-2 mutants provide no definite picture on the relationship between a function and the cellular effects. The experiments were based on computational and experimental studies which reported that the two mutants N15A and V25F decrease or abolish channel function while the truncation of the cytosolic termini maintains function (Schoemann and Fielding, 2019). At this point, it can be concluded from the presented data that the Ep-CoV-2 generated effects on $[Ca^{2+}]_{in}$, pH_{in} and E_M are sensitive to all three mutations. However, there is no apparent correlation between the proposed impacts of the mutations on channel structure and function on one side and the effects of these mutants on cellular activities on the other side. This suggests that the modulation of signaling cascades may be independent of channel function. An alternative explanation is that the impact of the mutations on channel function is not yet fully understood. This interpretation is in agreement with the findings that the N15A mutant, which was previously reported to corrupt channel function, was still able to generate some channel activity in model membranes (Figure 3.4C). Also, while some studies reported that the two mutants N15A and V25F alter or prevent oligomerization (Schoemann and Fielding, 2019), another study showed that they exhibit the same oligomerization as the Ep-CoV-2 wt protein (Park et al., 2021).

Even though the mode of action of Ep-CoV-2 in cells is not fully understood, the data presented here underpin that the viral protein modulates cellular functions in multiple ways. With such a prominent role in infected cells and with the known importance of Ep-CoV-2 in the pathogenicity of the virus, this protein presents a key target for developing virostatic drugs. This choice as a target is further supported by the fact that Ep-CoV-2 exhibits a much lower mutation frequency than other relevant targets like the spike protein (Rahman et al., 2021). In the case that some or all of the cellular functions are mediated by a channel function of Ep-CoV-2 the yeast complementation system can be developed together with similar systems in bacteria into versatile high-throughput screening systems for pore blockers.

3.5 Material and methods

3.5.1 Transfection of mammalian cells

For expression in mammalian cells, Ep-CoV-2 and Ep-CoV-2_{TM} were cloned into pEGFP-N2 which contains the eGFP sequence for generating C-terminal eGFP-tags as previously described in Schulze et al., 2021. The Ep-CoV-2 mutants N15A and V25F were generated by site-directed mutagenesis as described in (Papworth et al., 1996; Schulze et al., 2021).

For functional expression of Ep-CoV-2, Ep-CoV-2 mutants, Ep-CoV-2_{GFP} and Ep-CoV-2_{TM}, HEK293 and A549 cells were transfected 16 to 24 hours before the start of patch-clamp or fluorescence imaging experiments using TransfeX™ Transfection Reagent (ATCC, Manassas, Virginia, USA) according to the manufacturer's instructions. HEK293 and A549 cells (German Collection of Microorganisms and cell cultures, Braunschweig, Germany) were grown at 37°C in a humidified 95% air/ 5% CO_2 incubator in Dulbecco's Modified Eagle Medium (DMEM; Gibco) supplemented with 10% v/v heat-inactivated fetal bovine serum, 100 U/ml penicillin G, 100 µg/ml streptomycin sulfate and 2 mM L-glutamine (all from Invitrogen). After reaching approximately 80% confluence mammalian cells were (co-)transfected in a 35 mm petri dish with 1 µg of the plasmid carrying the gene of interest and (if necessary) 1 µg of empty pEGFP-N2 or empty pIRES2-mRuby3 to enable identification of transfected cells *via* eGFP or mRuby3 fluorescence, respectively. pIRES2-mRuby3 was generated by replacing the sequence encoding for the green fluorescent protein eGFP in pIRES2-eGFP by a DNA sequence encoding for the red fluorescent protein mRuby3.

3.5.2 Single Molecule Detection/Total Internal Reflection Fluorescence (SMD/TIRF) Microscopy

HEK293 cells transiently expressing Ep-CoV-2_{GFP} were grown on coverslips (Ø 25 mm). To favor strong adhesion of the cells to the glass, the coverslips were cleaned in a Zepto-B plasma furnace (Diener electronic GmbH, Ebhausen, Germany) and coated with a layer of 0.01% poly-D-lysine to favor strong adhesion of the cells to the glass. PM patches were then isolated by an osmotic shock with ice cold distilled water as described previously (Biel et al., 2016). The remaining PM patches on the glass coverslips were covered with PBS and imaged on a Nikon Ti-E stand (Nikon, Konan, Minato-ku, Tokyo, Japan) with a CFI Apo TIRF 100x objective (NA 1.49, WD 0.12 mm). For TIRF imaging the focus in the back focal plane was moved off-center by controlling the position of a mirror with a single-axis micropositioner stage M-126. DG controlled by a C-863 Mercury Servo Controller (Physik Instrumente (PI), Karlsruhe, Germany). PM patches and potential contaminations by remaining cortical

ER were stained with red fluorescent CellMask^{TM} Deep Red (CMDR) and ER-tracker^{TM} Blue-white DPX (both from ThermoFisher Scientific), respectively. The fluorescent markers were excited/detected as follows: GFP (488 nm/500-550 nm), ER-Tracker^{TM} (561 nm/577.5-646.5 nm) or CMDR (647 nm/ 662.5-799.5 nm).

3.5.3 Confocal laser scanning microscopy

Confocal laser scanning microscopy (CLSM) was performed on a Leica TCS SP or SP5 II system (Leica microsystems, Mannheim, Germany) equipped with 40 × 1.30 oil UV (HCX PL APO) objective. The external buffer for microscopy contained in mM: 140 NaCl, 4 KCl, 1 $MgCl_2$, 5 D-mannitol, 10 HEPES, 2 $CaCl_2$, pH 7.3 with an osmolarity of 310 mOsmol/kg. In all experiments mRuby3 fluorescence (561 nm/ 600-630 nm) was used as transfection control.

On the day of the experiment, transfected HEK293 or A549 cells were separated by incubation with accutase, seeded at low density on 25 mm coverslips, and then incubated for 2 to 4 hours to allow adhering of cells on the glass surface. For monitoring $[Ca^{2+}]_{in}$, HEK293 cells were loaded with the cell permeable Ca^{2+} sensor Fluo4-AM (ThermoFisher Scientific) for 30 min in microscopy buffer at a final concentration of 1 µM. In alternative experiments cells were loaded with FURA2-AM (ThermoFisher Scientific) as Ca^{2+} sensor by incubating cells for 30 min in buffer with 5 µM dye. Cytosolic pH was monitored by incubating HEK293 cells with the cell membrane permeable pH sensor BCECF-AM (2’,7’-Bis-(2-Carboxyethyl)-5-(and-6)-Carboxyfluorescein, Acetoxymethyl Ester) (Sigma Aldrich, St. Louis, MO, USA) for 30 min in microscopy buffer at a final concentration of 1.25 µM. The membrane potential of HEK293 cells was examined by loading the cells for 15 min with one of the two voltage sensitive dyes $DiBAC_4(3)$ (Bis-(1,3-Dibutylbarbituric Acid)Trimethine Oxonol) (AnaSpec, Fremont, CA, USA) or FluoVolt^{TM} (ThermoFisher Scientific) diluted with microscopy buffer to a final concentration of 10 µM or 13.7 µM, respectively. All dyes were removed after cell staining by washing cells with dye free buffer.

All dyes were detected at 500-540 nm and excited at 360 nm (Fura2) or 488 nm (all other dyes). Images were taken at a resolution of 1024 x 1024 pixels and a scan speed of 200 or 400 Hz. Signals of positive controls were recorded in 5 s intervals for 15-30 min in total after adding the corresponding solution. The same procedures were employed with A549 cells.

3.6 References

Anderson JA, Huprikar SS, Kochian LV, Lucas WJ, Gaber RF. 1992. Functional expression of a probable Arabidopsis thaliana potassium channel in Saccharomyces cerevisiae. Proc Natl Acad Sci U S A. 89(9):3736-40. DOI: 10.1073/pnas.89.9.3736, PMID: 1570292

Axelrod D. 1981. Cell-substrate contacts illuminated by total internal reflection fluorescence. J Cell Biol. 89(1):141-5. DOI: 10.1083/jcb.89.1.141, PMID: 7014571

Bai D, Fang L, Xia S, Ke W, Wang J, Wu X, Fang P, Xiao S. 2020. Porcine deltacoronavirus (PDCoV) modulates calcium influx to favor viral replication. Virology. 539:38-48. DOI: 10.1016/j.virol.2019.10.011, PMID: 31670218

Berridge MJ, Bootman MD, Roderick HL. 2003. Calcium signalling: dynamics, homeostasis and remodelling. Nat Rev Mol Cell Biol. 4(7):517-29. DOI: 10.1038/nrm1155, PMID: 12838335.

Bertl A, Ramos J, Ludwig J, Lichtenberg-Fraté H, Reid J, Bihler H, Calero F, Martínez P, Ljungdahl PO. 2003. Characterization of potassium transport in wild-type and isogenic yeast strains carrying all combinations of trk1, trk2 and tok1 null mutations. Mol Microbiol. 47(3):767-80. DOI: 10.1046/j.1365-2958.2003.03335.x, PMID: 12535075

Biel S, Aquila M, Hertel B, Berthold A, Neumann T, DiFrancesco D, Moroni A, Thiel G, Kauferstein S. 2016. Mutation in S6 domain of HCN4 channel in patient with suspected Brugada syndrome modifies channel function. Pflugers Arch. 468(10):1663-71. DOI: 10.1007/s00424-016-1870-1, PMID: 27553229.

Cabrera-Garcia D, Bekdash R, Abbott GW, Yazawa M, Harrison NL. 2021. The envelope protein of SARS-CoV-2 increases intra-Golgi pH and forms a cation channel that is regulated by pH. J Physiol. 599(11):2851-2868. DOI: 10.1113/JP281037, PMID: 33709461

Cashman DP. 2020. Why the lower reported prevalence of asthma in patients diagnosed with COVID-19 validates repurposing EDTA solutions to prevent and manage treat COVID-19 disease. Med Hypotheses. 144:110027. DOI: 10.1016/j.mehy.2020.110027, PMID: 32758873

Corse E, Machamer CE. 2003. The cytoplasmic tails of infectious bronchitis virus E and M proteins mediate their interaction. Virology. 312(1):25-34. DOI: 10.1016/s0042-6822(03)00175-2, PMID: 12890618

Crespi B, Alcock J. 2020. Conflicts over calcium and the treatment of COVID-19. Evol Med Public Health. 9(1):149-156. DOI: 10.1093/emph/eoaa046, PMID: 33732462

Dhama K, Patel SK, Kumar R, Rana J, Yatoo MI, Kumar A, Tiwari R, Dhama J, Natesan S, Singh R, Harapan H. 2020. Geriatric Population During the COVID-19 Pandemic: Problems, Considerations, Exigencies, and Beyond. Front Public Health. 8:574198. DOI: 10.3389/fpubh.2020.574198, PMID: 33072713

Fink K, Nitsche A, Neumann M, Grossegesse M, Eisele KH, Danysz W. Amantadine Inhibits SARS-CoV-2 In Vitro. Viruses. 2021 Mar 24;13(4):539. DOI: 10.3390/v13040539. PMID: 33804989

Gebhardt M, Hoffgaard F, Hamacher K, Kast SM, Moroni A, Thiel G. 2011. Membrane anchoring and interaction between transmembrane domains are crucial for K+ channel function. J Biol Chem. Apr 1;286(13):11299-306. DOI: 10.1074/jbc.M110.211672, PMID: 21310959

Griffin SD, Beales LP, Clarke DS, Worsfold O, Evans SD, Jaeger J, Harris MP, Rowlands DJ. 2003. The p7 protein of hepatitis C virus forms an ion channel that is blocked by the antiviral drug, Amantadine. FEBS Lett. 535(1-3):34-8. DOI: 10.1016/s0014-5793(02)03851-6, PMID: 12560074

Hallam TJ, Rink TJ. 1985. Agonists stimulate divalent cation channels in the plasma membrane of human platelets. FEBS Lett. 186(2):175-9. DOI: 10.1016/0014-5793(85)80703-1, PMID: 2408921.

Hoffmann M, Kleine-Weber H, Schroeder S, Krüger N, Herrler T, Erichsen S, Schiergens TS, Herrler G, Wu NH, Nitsche A, Müller MA, Drosten C, Pöhlmann S. 2020. SARS-CoV-2 Cell Entry Depends on ACE2 and TMPRSS2 and Is Blocked by a Clinically Proven Protease Inhibitor. Cell. 16;181(2):271-280.e8. DOI: 10.1016/j.cell.2020.02.052, PMID: 32142651

Hogue BG, Machamer CE. 2008. Coronavirus structural proteins and virus assembly. in *Nidoviruses* S. Perlman, T. Gallagher, E.J. Snijder, Eds. (ASM Press; Washington, DC, USA. 2008) pp. 179–200

Hutchison JM, Capone R, Luu DD, Shah KH, Hadziselimovic A, Van Horn WD, Sanders CR. 2021. Recombinant SARS-CoV-2 envelope protein traffics to the trans-Golgi network following amphipol-mediated delivery into human cells. J Biol Chem. 297(2):100940. DOI: 10.1016/j.jbc.2021.100940, PMID: 34237302

Hyser JM, Estes MK. 2015. Pathophysiological Consequences of Calcium-Conducting Viroporins. Annu Rev Virol. 2(1):473-96. DOI: 10.1146/annurev-virology-100114-054846, PMID: 26958925

Jeppesen MG, Toft-Bertelsen TL, Kledal TN, Rosenkilde MM. 2020. Amantadin has potential for treatment of COVID-19 because it tragets known and novel ion channels encoded by SARS-CoV-2. *Research Square*. DOI: 10.21203/rs.3.rs-121743/v1

Jimenez-Guardeño JM, Nieto-Torres JL, DeDiego ML, Regla-Nava JA, Fernandez-Delgado R, Castaño-Rodriguez C, Enjuanes L. 2014. The PDZ-binding motif of severe acute respiratory syndrome coronavirus envelope protein is a determinant of viral pathogenesis. PLoS Pathog. 10(8):e1004320. DOI: 10.1371/journal.ppat.1004320, PMID: 25122212

Liao Y, Yuan Q, Torres J, Tam JP, Liu DX. 2006. Biochemical and functional characterization of the membrane association and membrane permeabilizing activity of the severe acute respiratory syndrome coronavirus envelope protein. Virology. 349(2):264-75. DOI: 10.1016/j.virol.2006.01.028, PMID: 16507314

Mandala VS, McKay MJ, Shcherbakov AA, Dregni AJ, Kolocouris A, Hong M. 2020. Structure and drug binding of the SARS-CoV-2 envelope protein transmembrane domain in lipid bilayers. Nat Struct Mol Biol. 27(12):1202-1208. DOI: 10.1038/s41594-020-00536-8, PMID: 33177698

McClenaghan C, Hanson A, Lee SJ, Nichols CG. 2020. Coronavirus Proteins as Ion Channels: Current and Potential Research. Front Immunol.11:573339. DOI: 10.3389/fimmu.2020.573339, PMID: 33154751

Mehregan A, Pérez-Conesa S, Zhuang Y, Elbahnsi A, Pasini D, Lindahl E, Howard RJ, Ulens C, Delemotte L. 2021. Biophysical characterization of the SARS-CoV-2 E protein. *bioRxiv*. 2021.05.28.446179, DOI: https://doi.org/10.1101/2021.05.28.446179

Mesel-Lemoine M, Millet J, Vidalain PO, Law H, Vabret A, Lorin V, Escriou N, Albert ML, Nal B, Tangy F. 2012. A human coronavirus responsible for the common cold massively kills dendritic cells but not monocytes. J Virol. 86(14):7577-87. DOI: 10.1128/JVI.00269-12l, PMID: 22553325

Moorthy NS, Poongavanam V, Pratheepa V. 2014. Viral M2 ion channel protein: a promising target for anti-influenza drug discovery. Mini Rev Med Chem. 14(10):819-30, DOI: https://doi.org/10.2174/138955751410141020150822, PMID: 25342196.

Nieto-Torres JL, Dediego ML, Alvarez E, Jiménez-Guardeño JM, Regla-Nava JA, Llorente M, Kremer L, Shuo S, Enjuanes L. 2011. Subcellular location and topology of severe acute respiratory syndrome coronavirus envelope protein. Virology. 415(2):69-82. DOI: 10.1016/j.virol.2011.03.029, PMID: 21524776

Nieto-Torres JL, DeDiego ML, Verdiá-Báguena C, Jimenez-Guardeño JM, Regla-Nava JA, Fernandez-Delgado R, Castaño-Rodriguez C, Alcaraz A, Torres J, Aguilella VM, Enjuanes L. 2014. Severe acute respiratory syndrome coronavirus envelope protein ion channel activity promotes virus fitness and pathogenesis. PLoS Pathog.10(5):e1004077. DOI: 10.1371/journal.ppat.1004077, PMID: 24788150

Nieto-Torres JL, Verdiá-Báguena C, Jimenez-Guardeño JM, Regla-Nava JA, Castaño-Rodriguez C, Fernandez-Delgado R, Torres J, Aguilella VM, Enjuanes L. 2015. Severe acute respiratory syndrome coronavirus E protein transports calcium ions and activates the NLRP3 inflammasome. Virology. 485:330-9. DOI: 10.1016/j.virol.2015.08.010, PMID: 26331680

Nieva JL, Madan V, Carrasco L. 2012. Viroporins: structure and biological functions. Nat Rev Microbiol. 2;10(8):563-74. DOI: 10.1038/nrmicro2820, PMID: 22751485

Olivier M. 1996. Modulation of host cell intracellular Ca2+. Parasitol Today. 12(4):145-50. DOI: 10.1016/0169-4758(96)10006-5, PMID: 15275223.

Papworth C, Braman J, Wright DA. 1996 Site- directed mutagenesis in one day with >80% efficiency. Strategies. 9, 3-4.

Paredes RM, Etzler JC, Watts LT, Zheng W, Lechleiter JD. 2008. Chemical calcium indicators. Methods. 46(3):143-51. DOI: 10.1016/j.ymeth.2008.09.025, PMID: 18929663

Park SH, Siddiqi H, Castro DV, De Angelis AA, Oom AL, Stoneham CA, Lewinski MK, Clark AE, Croker BA, Carlin AF, Guatelli J, Opella SJ. 2021. Interactions of SARS-CoV-2 envelope protein with amilorides correlate with antiviral activity. PLoS Pathog. 17(5):e1009519. DOI: 10.1371/journal.ppat.1009519, PMID: 34003853

Pervushin K, Tan E, Parthasarathy K, Lin X, Jiang FL, Yu D, Vararattanavech A, Soong TW, Liu DX, Torres J. 2009. Structure and inhibition of the SARS coronavirus envelope protein ion channel. PLoS Pathog. 5(7):e1000511. doi: 10.1371/journal.ppat.1000511, PMID: 19593379

Pinto LH, Lamb RA. 2007. Controlling influenza virus replication by inhibiting its proton channel. Mol Biosyst. 3(1):18-23. DOI: 10.1039/b611613m, PMID: 17216051

Putnam RW. 2012 Intracellular pH Regulation. in *Cell Physiology Source Book.* N. Sperelakis Ed. (Academic Press. *4th edition* 2012) pp. 303-321.

Rahman MS, Hoque MN, Islam MR, Islam I, Mishu ID, Rahaman MM, Sultana M, Hossain MA. 2021. Mutational insights into the envelope protein of SARS-CoV-2. Gene Rep. 22:100997. DOI: 10.1016/j.genrep.2020.100997, PMID: 33319124

Schoeman D, Fielding BC. 2019. Coronavirus envelope protein: current knowledge. Virol J. 16(1):69. DOI: 10.1186/s12985-019-1182-0, PMID: 31133031

Singh Tomar PP, Arkin IT. 2020. SARS-CoV-2 E protein is a potential ion channel that can be inhibited by Gliclazide and Memantine. Biochem Biophys Res Commun. 530(1):10-14. DOI: 10.1016/j.bbrc.2020.05.206, PMID: 32828269

Sjaak de Wit JJ, Cook JK, van der Heijden HM. 2011. Infectious bronchitis virus variants: a review of the history, current situation and control measures. Avian Pathol. 40(3):223-35. DOI: 10.1080/03079457.2011.566260, PMID: 21711181

Surya W, Li Y, Torres J. 2018. Structural model of the SARS coronavirus E channel in LMPG micelles. Biochim Biophys Acta Biomembr. 1860(6):1309-1317. DOI: 10.1016/j.bbamem.2018.02.017, PMID: 29474890

To J, Surya W, Fung TS, Li Y, Verdià-Bàguena C, Queralt-Martin M, Aguilella VM, Liu DX, Torres J. 2017. Channel-Inactivating Mutations and Their Revertant Mutants in the Envelope Protein of Infectious Bronchitis Virus. J Virol. 91(5):e02158-16. DOI: 10.1128/JVI.02158-16, PMID: 27974570

Torres J, Maheswari U, Parthasarathy K, Ng L, Liu DX, Gong X. 2007. Conductance and amantadine binding of a pore formed by a lysine-flanked transmembrane domain of SARS coronavirus envelope protein. Protein Sci. 16(9):2065-71. DOI: 10.1110/ps.062730007, PMID: 17766393

Ujike M, Taguchi F. 2015. Incorporation of spike and membrane glycoproteins into coronavirus virions. Viruses. 7(4):1700-25. DOI: 10.3390/v7041700, PMID: 25855243

Verdiá-Báguena C, Nieto-Torres JL, Alcaraz A, DeDiego ML, Torres J, Aguilella VM, Enjuanes L. 2012. Coronavirus E protein forms ion channels with functionally and structurally-involved membrane lipids. Virology. 432(2):485-94. DOI: 10.1016/j.virol.2012.07.005, PMID: 22832120

Verdiá-Báguena C, Nieto-Torres JL, Alcaraz A, Dediego ML, Enjuanes L, Aguilella VM. 2013. Analysis of SARS-CoV E protein ion channel activity by tuning the protein and lipid charge. Biochim Biophys Acta. 1828(9):2026-31. DOI: 10.1016/j.bbamem.2013.05.008, PMID: 23688394

Verdiá-Báguena C, Aguilella VM, Queralt-Martín M, Alcaraz A. 2021. Transport mechanisms of SARS-CoV-E viroporin in calcium solutions: Lipid-dependent Anomalous Mole Fraction Effect and regulation of pore conductance. Biochim Biophys Acta Biomembr. 1863(6):183590. DOI: 10.1016/j.bbamem.2021.183590, PMID: 33621516

Wang JY, Zhang W, Roehrl MW, Roehrl VB, Roehrl MH. 2021. An autoantigen profile of human A549 lung cells reveals viral and host etiologic molecular attributes of autoimmunity in COVID-19. J Autoimmun. 120:102644. DOI: 10.1016/j.jaut.2021.102644, PMID: 33971585

Wilson L, McKinlay C, Gage P, Ewart G. 2004. SARS coronavirus E protein forms cation-selective ion channels. Virology. 330(1):322-31. DOI: 10.1016/j.virol.2004.09.033, PMID: 15527857

Wilson L, Gage P, Ewart G. 2006. Hexamethylene amiloride blocks E protein ion channels and inhibits coronavirus replication. Virology. 353(2):294-306. DOI: 10.1016/j.virol.2006.05.028, PMID: 16815524

Winterstein LM, Kukovetz K, Rauh O, Turman DL, Braun C, Moroni A, Schroeder I, Thiel G. 2018. Reconstitution and functional characterization of ion channels from nanodiscs in lipid bilayers. J Gen Physiol. 150(4):637-646. DOI: 10.1085/jgp.201711904, PMID: 29487088

Xia B, Shen X, He Y, Pan X, Liu FL, Wang Y, Yang F, Fang S, Wu Y, Duan Z, Zuo X, Xie Z, Jiang X, Xu L, Chi H, Li S, Meng Q, Zhou H, Zhou Y, Cheng X, Xin X, Jin L, Zhang HL, Yu DD, Li MH, Feng XL, Chen J, Jiang H, Xiao G, Zheng YT, Zhang LK, Shen J, Li J, Gao Z. 2021. SARS-CoV-2 envelope protein causes acute respiratory distress syndrome (ARDS)-like pathological damages and constitutes an antiviral target. Cell Res. 31(8):847-860. DOI: 10.1038/s41422-021-00519-4, PMID: 34112954

Zhang LK, Sun Y, Zeng H, Wang Q, Jiang X, Shang WJ, Wu Y, Li S, Zhang YL, Hao ZN, Chen H, Jin R, Liu W, Li H, Peng K, Xiao G. 2020. Calcium channel blocker amlodipine besylate therapy is associated with reduced case fatality rate of COVID-19 patients with hypertension. Cell Discov. 6(1):96. DOI: 10.1038/s41421-020-00235-0, PMID: 33349633

Zhou Y, Frey TK, Yang JJ. 2009. Viral calciomics: interplays between Ca2+ and virus. Cell Calcium. 46(1):1-17. DOI: 10.1016/j.ceca.2009.05.005, PMID: 19535138

Amino acids and codes

Alanine	A	Ala
Arginine	R	Arg
Asparagine	N	Asn
Aspartic acid	D	Asp
Cysteine	C	Cys
Glutamine	Q	Gln
Glutamic acid	E	Glu
Glycine	G	Gly
Histidine	H	His
Isoleucine	I	Ile
Leucine	L	Leu
Lysine	K	Lys
Methionine	M	Met
Phenylalanine	F	Phe
Proline	P	Pro
Serine	S	Ser
Threonine	T	Thr
Tryptophane	W	Trp
Tyrosine	Y	Tyr
Valine	V	Val

Own work

2. Electrophysiological characterization using structural data to gain insights into ion selectivity and gating mechanisms of lysosomal TMEM175 K^+ channels:

Experiments, data analysis and writing were exclusively done by myself, with exception of:

- Dr. Janine Brunner, Dr. Roman Jakob, Dr. Stephan Schenk and Prof. Dr. Timm Maier cloned genes, purified and crystallized the proteins and analyzed crystallographic data.
- Prof. Dr. Gerhard Thiel contributed to the electrophysiological measurements of MtTMEM175_wt with different cations in the bath solution.
- Dr. Janine Brunner, Dr. Stephan Schenk and Prof. Dr. Gerhard Thiel contributed to the design of experiments and the interpretation of the data.

3. Ep-Cov-2 – The Envelope Protein of SARS-CoV-2 corrupts homeostatic signaling mechanisms in mammalian cells

Experiments, data analysis and writing were exclusively done by myself, with exception of:

- Dr. Andreas Hartel performed the single channel measurements in planar lipid bilayers and western blotting experiments. Dr. Andreas Hartel and Dr. Oliver Rauh analyzed the data obtained.
- Sebastian Höler performed the yeast complementation assay. Sebastian Höler and Dr. Oliver Rauh analyzed the data obtained.
- Dr. Oliver Rauh performed the patch clamp measurements in voltage clamp as well as current clamp conformation and analyzed the data obtained.
- Clara Hemming (Bachelor) performed most of the fluorescent microscopic measurements with the Ep-CoV-2_{TM} mutant and analyzed the data obtained, both under my supervision.
- Sebastian Höler, Dr. Andreas Hartel, Dr. Oliver Rauh and Prof. Dr. Gerhard Thiel contributed in close cooperation to the design of the experiments and the interpretation of the data.

Declaration – Ehrenwörtliche Erklärung

Ich erkläre hiermit ehrenwörtlich, dass ich die vorliegende Arbeit entsprechend den Regeln guter wissenschaftlicher Praxis selbstständig und ohne unzulässige Hilfe Dritter angefertigt habe.

Sämtliche aus fremden Quellen direkt oder indirekt übernommenen Gedanken sowie sämtliche von Anderen direkt oder indirekt übernommenen Daten, Techniken und Materialien sind als solche kenntlich gemacht. Die Arbeit wurde bisher bei keiner anderen Hochschule zu Prüfungszwecken eingereicht.

Darmstadt, den 02.11.2021

……………………………………………………………………………

Acknowledgements - Danksagung

Ich möchte mich an dieser Stelle bei allen Personen bedanken, die mich in den letzten Jahren unterstützt und zum Gelingen dieser Arbeit beigetragen haben.

Mein besonderer Dank geht an:

Herrn Prof. Dr. Gerhard Thiel für die Möglichkeit, diese Thesis in seiner Arbeitsgruppe erarbeiten und mich wissenschaftlich frei entfalten zu dürfen. Darüber hinaus möchte ich mich für seine stets lockere und gelassene aber dennoch interessierte Art bedanken, die ich sehr schätze.

Herrn Prof. Dr. Bodo Laube für die Übernahme des Zweitgutachtens.

Oliver Rauh und **Sebastian Höler** sowie auch **Andreas Hartel** für die enge Zusammenarbeit an Ep-CoV-2 während der schwierigen Situation in Zeiten der CoVid-19 Pandemie. Die Arbeit mit euch an diesem Projekt war wirklich sehr motivierend!

Brigitte Hertel, Silvia Haase, Sylvia Lenz, Mirja Manthey, Tanja Musielak und **Ulrike Burk** für ihre Hilfsbereitschaft sowie das Bereitstellen eines organisierten und funktionierenden Laboralltags.

Clara Hemming für ihre sehr gute Bachelor-Arbeit. Ihre eigenständige Arbeit im Labor und ihre geordnete Arbeitsweise haben mir im Rahmen meiner Arbeit sehr weitergeholfen.

Robert Lehn für die Hilfe am TIRF-Mikroskop und **Dominique Tandl** für die Einweisung am CLSM.

Allen Korrektur-Lesern, die sich am Ende meiner Arbeit noch die Zeit genommen haben, mich auf diese Weise zu unterstützen (**Prof. Dr. Gerhard Thiel, Theresa Gebhard, Oliver Rauh, Sebastian Höler**).

Dem Kinderzimmer und der gesamten AG Thiel für die große Hilfsbereitschaft und das spaßige und herzliche Miteinander. Weiterhin bedanke ich mich für die vielen gemeinsamen Aktivitäten wie Kickerrunden, Marathon-Läufe, Feierabendbiere, Dart-Sessions und vor allem für sehr enge Freundschaften auch in privatem Rahmen (**Kerri Kukovetz, Laura Winterstein (geb. Schlee), Oliver Rauh, René Lautenschläger, Sebastian Mach, Sebastian Höler, Tobias Winterstein, Paolo Zuccolini, Bianca Introini uvm.**).

Teile der **AG Laube und Warzecha**, die zunehmend Einfluss auf die privaten Aspekte des Alltags der AG Thiel nehmen.

Im privaten Zusammenhang danke ich besonders:

meinen Freunden **Bianca Introini, Oliver Rauh und Kerri Kukovetz** sowie allen anderen, die mich in ungewöhnlichen aber auch in sehr schwierigen Zeiten sowohl unterstützt als auch abgelenkt haben.

meiner Familie, die wir in den letzten Zügen dieser Arbeit noch einmal vor eine unglaublich schwere und unbegreifliche Situation gestellt wurden. Ich danke euch dafür, dass Ihr nie aufgehört habt an mich zu glauben und mich all die Jahre so sehr unterstützt habt!

Theresa Gebhard, die mich in allen Lebenslagen unterstützt. Sie hat mir immer den Rücken freigehalten und vor allem in den Endzügen dieser Arbeit sehr häufig zurückstecken müssen. Ich danke dir einfach für Alles und hoffe, dass ich dir diese Art von Unterstützung irgendwann zurückgeben kann.